



UNIVERSITÀ POLITECNICA DELLE MARCHE  
Repository ISTITUZIONALE

Modal-based FE model updating via genetic algorithms: Exploiting artificial intelligence to build realistic numerical models of historical structures

This is the peer reviewed version of the following article:

*Original*

Modal-based FE model updating via genetic algorithms: Exploiting artificial intelligence to build realistic numerical models of historical structures / Standoli, Gianluca; Salachoris, Georgios Panagiotis; Masciotta, Maria Giovanna; Clementi, Francesco. - In: CONSTRUCTION AND BUILDING MATERIALS. - ISSN 0950-0618. - STAMPA. - 303:(2021). [10.1016/j.conbuildmat.2021.124393]

*Availability:*

This version is available at: 11566/291691 since: 2024-04-28T12:35:07Z

*Publisher:*

*Published*

DOI:10.1016/j.conbuildmat.2021.124393

*Terms of use:*

The terms and conditions for the reuse of this version of the manuscript are specified in the publishing policy. The use of copyrighted works requires the consent of the rights' holder (author or publisher). Works made available under a Creative Commons license or a Publisher's custom-made license can be used according to the terms and conditions contained therein. See editor's website for further information and terms and conditions.

This item was downloaded from IRIS Università Politecnica delle Marche (<https://iris.univpm.it>). When citing, please refer to the published version.

(Article begins on next page)

# **Modal-based FE model updating via Genetic Algorithms: exploiting artificial intelligence to build realistic numerical models of historical structures**

Gianluca Standoli<sup>1</sup>, Georgios Panagiotis Salachoris<sup>1</sup>, Maria Giovanna Masciotta<sup>2</sup>, Francesco Clementi<sup>1,\*</sup>

<sup>1</sup>*Dept. ICEA, Università Politecnica delle Marche, Via Brecce Bianche, 60131 Ancona, Italy*

<sup>2</sup>*Dept. of Engineering and Geology, University "G. d'Annunzio" of Chieti-Pescara, Viale Pindaro 42, 65127 Pescara, Italy*

e-mail : {g.standoli, g.p.salachoris }@pm.univpm.it, g.masciotta@unich.it,  
francesco.clementi@univpm.it,  
\*corresponding author

## **HIGHLIGHTS**

- A FE model calibration based on AVT and machine learning process is presented.
- The dynamic parameters of the investigated tower are estimated via OMA techniques.
- Different parameterization and modelling assumptions are employed for the updating.
- The calibrated model accurately reproduces the real dynamic behaviour of the tower.

## **ABSTRACT**

Cultural Heritage preservation requires the combination of in situ investigations and accurate Finite Elements models in order to correctly interpret the empirical evidence and successfully apply advanced structural analyses for health assessment purposes, allowing to infer about the future evolution of the structural response and timely detect deviations from the expected behaviour.

In this paper the actual dynamic behaviour of the Civic Tower of Ostra, Italy, is thoroughly investigated by means of a detailed numerical model built and calibrated using the experimental modal features estimated through field dynamic testing. To this end, a fully automated Finite Element Model Updating procedure based on genetic algorithms and machine learning is conceived and employed, allowing the successful estimation of the unknown material properties of the tower, considering both isotropic and orthotropic behavioural models for masonry. The results enabled to establish baseline information on the current structural condition of the heritage and to set to performance standards that will serve to optimise the control of the structural integrity over time.

## **KEYWORDS**

Masonry Towers, Cultural Heritage, Structural Health Monitoring, Operational Modal Analysis, Automated Model Updating, Genetic Algorithms, Machine Learning

## 1. Introduction

Masonry towers are one of the most widespread structural typologies among the various Italian Cultural Heritage (CH) buildings. One peculiar characteristic of this category of buildings is their evident slenderness. This aspect, together with the numerous uncertainties associated to masonry structures, such as irregularities and imperfections, complexity of the internal structure, local variability of material properties as well as the effects of past damages and repairs, makes masonry towers particularly vulnerable to seismic actions, as the tragical events of last years demonstrated [1–6].

Besides their cultural and social importance, heritage structures and sites positively impact the economy of the cities and countries in which they are located by providing touristic attractions. Thus, it is crucial to guarantee appropriate maintenance plans and undertake regular preventive actions in order to prevent irreparable damages and avoid unexpected collapses with consequent unsustainable losses. Particularly, as far as masonry towers are concerned, their high vulnerability to seismic loading calls for an accurate characterization of their dynamic behaviour in order to better understand their actual response during earthquakes. The achievement of a thorough knowledge about the global behaviour of these unconventional structures, also considering their interaction with the surrounding environment [7–10], is indispensable for a reliable structural assessment and for the early identification of damage.

Damage can be considered as an adverse condition that impairs the structural behaviour of a system and causes a deviation from its expected response, often resulting in excessive displacements, vibrations and/or undesirable stresses. Early-stage damage detection is therefore crucial to ensure both the integrity of the structures and the safety of their users. Several damage identification techniques based on the observation of dynamic properties variations in structural systems have been developed in the last decades [11–16], given the high sensitivity of modal parameters to damage-induced changes. Among these techniques, vibration-based Structural Health Monitoring (SHM) tools have shown a great potential for the structural assessment of historical constructions, both from a static and a dynamic point of view, standing as reliable full-scale investigation methods that allow to collect experimental data representative of the global structural behaviour without resorting to any invasive technique, thus preserving the historical value of the construction. The basic idea of vibration-based damage detection methods is that any change in the physical and mechanical properties of the structure, or in its boundary conditions, will cause changes in its dynamic properties. Thus, by deploying a grid of wired or wireless sensors at strategic locations, one can keep under control the behaviour of any system by following the evolution of its modal parameters estimated from the vibration signatures recorded across the instrumented structure. To this end, operational modal analysis (OMA) techniques are preferred over traditional experimental modal analysis (EMA) approaches since they allow to estimate the modal parameters of the structure under real operational and boundary conditions (e.g. without interrupting the operative function of the building), using freely available ambient excitations as input force, and measuring only the output vibration response of the structure [17].

Ambient Vibration tests (AVT) are commonly used in conjunction with another classical procedure in the field of damage identification which is Finite Element (FE) model updating, whose application for design and construction of structures has started since the 1980s [18] and, in recent years, has been successfully extended to existing masonry structures [8,19–23]. This updating process consists in calibrating the unknown properties of a structural system till the distance between numerical and experimental dynamic responses, particularly in terms of modal frequencies and mode shapes, is minimized. This fine-tuning operation, if performed manually by a trial-and-error approach, can result cumbersome and very time-consuming in case of large and complex structures, making impossible the accurate estimation of the global optimal solution. Various authors have therefore turned their attention towards automated iterative procedures; though, given the high computational time often required by the elevated number of iterations and the non-practicability of the approach when the number of free variables is considerable, in many cases they ended up resorting to approximate methods for the updating [18,24,25]. With the aim of reducing the unknown quantities that should be considered in the FE model updating, global sensitivity analysis methods can be adopted to measure the effective dependence of the structure's frequencies on the different parameters and better address their selection

[26–28]. Despite the inherent advantages, reducing the number of candidate parameters limits the updating problem to a particular condition state of the structure, thus the sensitivity analysis must be necessarily repeated every time new data are collected from the system in order to avoid an ill-conditioned updating that might preclude not only the representativeness of the model but also the assessment and evolution of localized damage mechanisms. To overcome this aspect, alternative optimization methods able to deal with large and multi-dimensional problems can be exploited [29,30], like nature-inspired metaheuristics [31].

Within this framework, the present work aims to provide a contribution to the field of structural assessment and damage identification of historic masonry structures by proposing an iterative updating procedure based on Genetic Algorithms (GA) to build a reliable reference model of a heritage tower located in Central Italy for future comparative analyses and health monitoring [29,32].

For the purpose of this work, the genetic algorithm provided by the open-source finite element solver Code\_Aster© is employed to automatically find the optimal values for the unknown material properties of the investigated tower, starting from the model calibrated against 2018 experimental results and then updated to match the behaviour identified with 2019 measurements [33–38]. To better assess the efficiency, accuracy and reliability of the proposed approach, the dimensionality of the problem is upscaled by increasing the number of updating variables to be determined, thereby allowing to take into account also the uncertainties associated with the modelling of masonry as an isotropic or orthotropic material. Without artificial intelligence, such a detailed study would not be possible.

In addition to this introductory section, the remaining of the paper is organized as follows. Section 2 describes the tower history and the outcome of the geometric and material surveys; Section 3 focuses on the identification of the modal parameters of the structure through OMA techniques; Section 4 presents and discusses in detail the model updating process using GAs. Finally, Section 5 summarizes the main conclusions that can be drawn from the work.

## **2. Ostra Civic Tower: description of the case study**

### **2.1 Historical survey**

Located about 40 km away from Ancona, Ostra is one of the typical villages of the Marche region, in Central Italy. Lying on a hill, overlooking the river Misa Valley, it is said that Ostra was founded by the exiles of the Roman Empire and its original name, till 1881, was Montalboddo. Destroyed during Goths invasion, the village was rebuilt, and during the Middle Age, it was surrounded by a protective wall, 1200 meters long, interspersed with square section towers, nine of those still existing today.

Nowadays, the centre of the city life is represented by the central Piazza dei Martiri, located in the upper part of the historic centre, where the most important buildings, such as Palazzo Comunale, San Francesco Church, La Vittoria Theatre, are found. Among them, the most emblematic building of the city – case study of this paper – stands: Ostra Civic Tower (Figure 1). Built in the XVI century, this tower is also known as “Clock Tower” because of the ancient clock gears still present today, even if no longer in operation.



*Figure 1 - Ostra Civic Tower localization.*

According to historical sources [39,40], the belfry tower was originally connected to San Giovanni Church (Figure 2a). The two buildings had autonomous origins: the church was mentioned for the first time in archival documents in 1454, while the tower was built in 1552 at the behest of the magistracy. The bell, hosted today by the third order of floors, dates to 1631.





Figure 2 - San Francesco Church and the Tower before bombardments (a) and a view of the central square to the present days (b).

With its architecture and double staircase, the church closed the fourth side of the square, making it an elegant “living room”. The interior of the structure treasured various artworks, including many altarpieces such as that of Andrea Sacchi (1599/1661) depicting San Bonaventura da Bagnoregio and San Tommaso d'Aquino (today stored at the Superintendence of Urbino). Though, following the aerial bombardments occurred in 1944 during the II World War, only the church façade and the civic tower survived.

Because of the precarious conditions of the structures, it was decided to intervene by demolishing the rests of the façade and strengthening the tower. Façade demolition led to the uncovering of the foundations of the tower walls and of the external staircase of the building, making them prone to degradation phenomena due to atmospheric agents and pollutants. Therefore, foundation works were promptly carried out along with the recovery of the base walls. Parts of the external walls and battlements damaged by the bursts of artillery bullets were also restored.

After the works, a new architectural arrangement of the square became indispensable. Some projects envisaged creating a decent background, in harmony with the palaces that frame the town square, and erecting a building that could replace the beautiful (demolished) façade and which could form, together with the civic tower, a single majestic and harmonious architectural complex (Figure 2b).

## 2.2 Geometrical and material survey

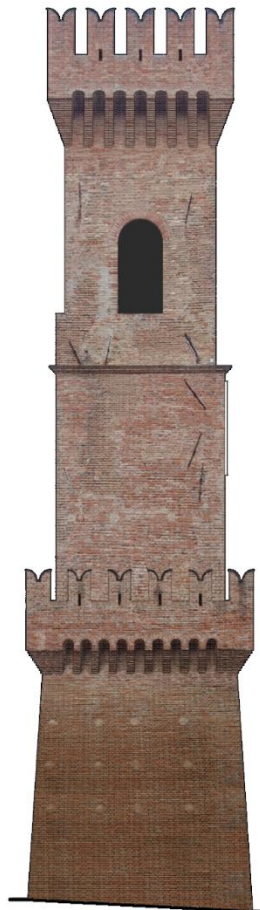
With an overall height of 30 meters (before the interventions executed in 1950, when the foundations were partially uncovered and the top part was added, the original height was 25 meters), the Civic Tower of Ostra is a historical masonry structure featuring four main parts: the basement, the central body, the bell cell and the top roof (Figure 3). In what concerns the parts belonging to the original tower, the bell cell is unchanged, while the central body is partially reconstructed, as the changes of the masonry texture reveal.

The basement consists of a truncated pyramid, whose lower base measures approximately  $7.30 \times 7.50 \text{ m}^2$ , while the upper base is about  $5.30 \times 5.60 \text{ m}^2$ . This part develops up to a height of 9.55 meters, culminating in an embattled balcony. Hereon, the parallelepipedal central body starts, keeping the same shape for additional 9.50 meters. Then, the cross section of the tower slightly reduces at the level of the bell cell and remains unchanged till the embattled enlargement of the upper part.

The tower results composed of five floors: the first three are connected through spiral staircases starting from the ground level, while the last two orders of floors are reachable using an iron ladder. The clock mechanism is located on the second floor, whereas the bell cell occupies the third level, whose perimetral walls are pierced by single-light arched windows, one per side. The entrance is located on the main façade (north-east oriented), which overlooks Piazza dei Martiri.



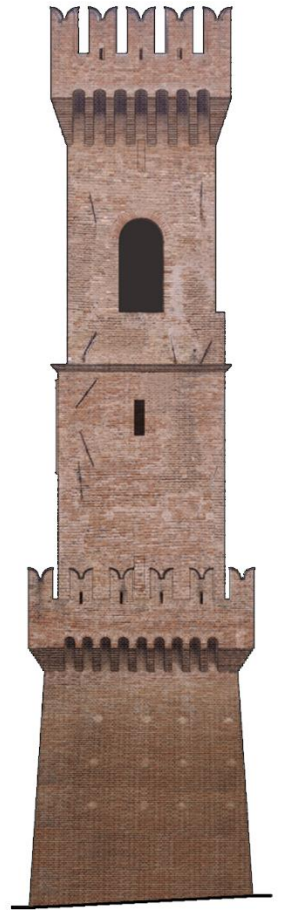
North-East Facade



South-East Facade



South-West Facade



North-West Facade

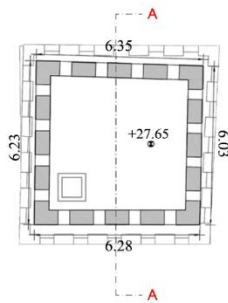
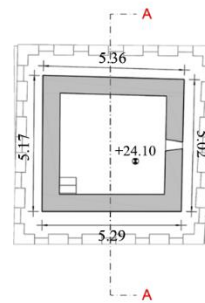
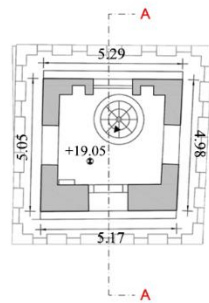
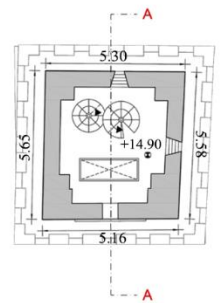
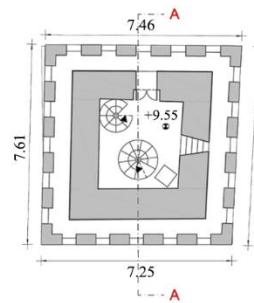
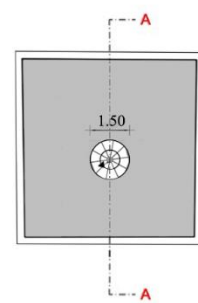
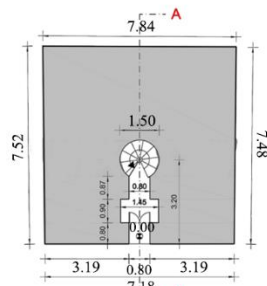
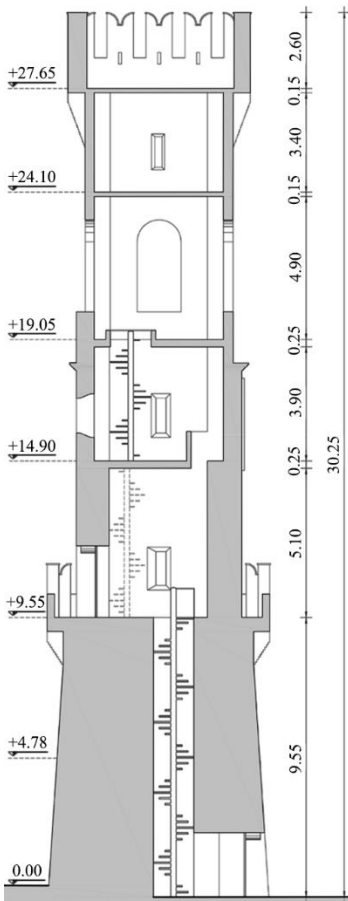


Figure 3 - Geometrical survey of the investigated tower: front views (top) and CAD sections (bottom).



The survey allowed to distinguish different construction features and materials across the tower (Figure 4). Particularly, the bearing walls, whose thickness ranges from 1.1 meters in the lower part (first floor) to 0.6 meters in the upper part (last floor), resulted built with solid brick masonry and thin mortar joints. As for the basement walls, their remarkable thickness let infer the presence of an inner rubble core between brick outer layers, though no investigation could be performed to confirm the hypotheses about their internal morphology. The structural interventions undergone by the tower include the reinforced concrete slabs constituting the floors, whose thickness varies from 0.11 meters to 0.27 meters, the concrete columns built to reinforce the corners at the third level, and the iron tie-rods installed after the 1997 seismic events of Umbria-Marche region aimed at restraining possible out-of-plane mechanisms. No worrying cracks nor other structural damages were detected during the visual inspection.



Figure 4 – Excerpts from the photographic survey of the tower:(1) trapdoor accessing the upper level and connecting iron ladder; (2) close-up of the 4<sup>th</sup> level brickwork; (3) concrete slab of the 3<sup>rd</sup> floor with ladder opening;(4) particular of the reinforcement intervention with tie rods; (5) close-up of the 2<sup>nd</sup> level internal brickwork; (6) external brickwork of the 1<sup>st</sup> level; (7) basement brickwork; (8) spiral staircase at the entrance level.

### 3. Ambient vibration testing

Given its non-destructive nature, Ambient Vibration Testing (AVT) has become a common in situ investigation technique for the estimation of dynamic parameters associated with the global behavior of historical structures. This tool results extremely useful to collect reliable experimental data and increase the level of knowledge of the structure whenever its historical value may pose limitations to the application of other diagnostic techniques for the system’s characterization. By deploying a set of sensors at selected locations and capturing the vibration response of the structure to random ambient excitations (traffic, wind, human walking, micro-tremors), the dynamic features of the system, namely natural frequencies ( $f$ ), damping ratios ( $\xi$ ) and mode shapes ( $\varphi$ ), can be extracted and used to better



interpret the actual behaviour of age-old constructions, which are often highly complex and mechanically diverse.

In the last years, numerous works showed the potentiality of vibration monitoring through accelerometric sensors in the study of the dynamic behavior of historical buildings, both for short-term [41,42] and long-term applications [43]. Indeed, besides the economic benefits associated with the possibility of using freely available environmental excitations, AVT allows to perform rapid screenings of the structural fitness under real operational and boundary conditions. Moreover, the processing of the acquired vibration data enables the construction of an Experimental Model (EM) of the structure, which provides the dynamic parameters that the Numerical Model (NM) has to match to realistically reproduce the structural response [44].

### 3.1 Field testing procedure

In order to characterize the dynamic behaviour of the Civic Tower of Ostra, two field dynamic testing campaigns in operational conditions were conducted in June 2018 and in February 2019. The sensor network was composed of four triaxial piezoelectric accelerometers, with an integrated MEMS tilt-meter system for correction of errors due to inclination, characterized by a maximum measurement range of 8 g, a sensitivity of 1000 mV/g and a bandwidth range from 0.8 to 100 Hz. The digitization process was automated through an A/D converter with 24 bits of resolution, 120 dB of dynamic range and provided with anti-aliasing filter. The synchronization between sensors was ensured by a 4-channel Sync Hub connecting the accelerometers to the PC for data storage.



Figure 5 - Instrumentation used for the ambient vibration tests.

In both campaigns, three setups were used to measure the response of the tower in 8 selected points evenly deployed on the opposite corners of four levels (Figure 6). Each setup consisted of four accelerometers: two were fixed on the top floor and kept as reference sensors, while the remaining two were moved downward in each acquisition so as to record the vibration processes of the tower along the three directions of the 8 identified points, allowing to catch all the meaningful modal displacements of the structure, including torsional components. It is noted that the sensor layouts for the signal acquisition were established in accordance with the results of a preliminary numerical modal analysis coupled with an Optimal Sensor Placement (OPT) procedure [45,46], with the intent of identifying the

best position for the accelerometers to maximize the quality of the AVT information despite the limited number of available sensors.

To comply with Rodriguez's indications [47], the total duration of the acquisition was set longer than 2000 times the estimated fundamental period of the structure: indeed, every registration lasted around 40 minutes, thereby assuring the elimination of the possible influence of non-stochastic excitations. Moreover, to guarantee a high frequency resolution for the spectral density estimation, a sampling frequency of 1024 Hz was adopted, resulting in 2,457,600 datapoints per time series.

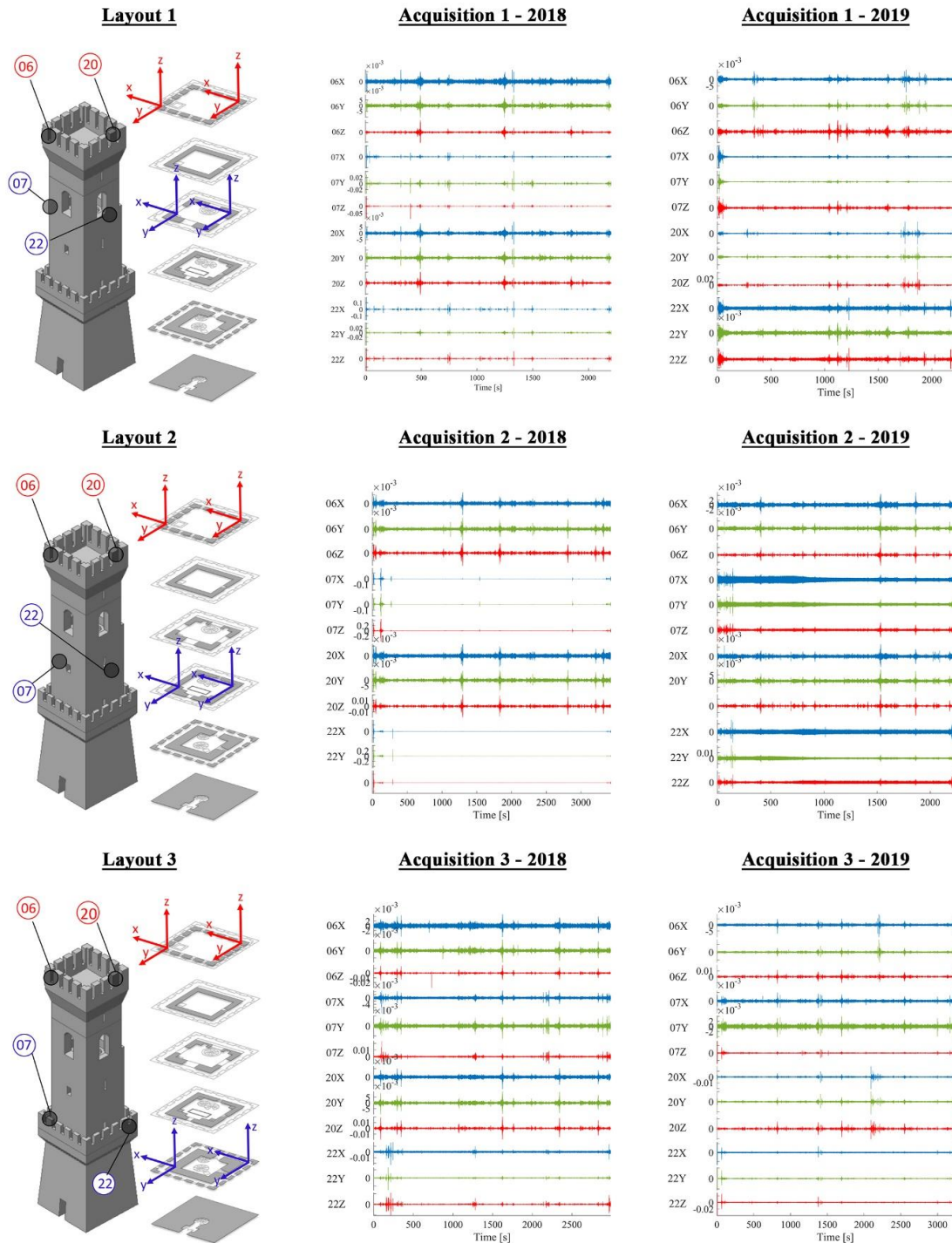


Figure 6 - Sensor layouts and corresponding acceleration time series for 2018 and 2019 dynamic testing campaigns (blue, green and red colours indicate signals in x, y and z direction, respectively).

## 3.2 Operational modal analysis

### 3.3.1 Data processing

The extraction of the dynamic features of the tower (i.e. natural frequencies  $f$ , damping ratios  $\xi$  and mode shapes  $\varphi$ ) was performed through the application of Operational Modal Analysis (OMA) techniques, using the acceleration time series acquired in operating conditions through the aforementioned contact sensor network. Many are the output-only dynamic identification approaches available in the literature that can be adopted for this purpose, both in the time and in the frequency domain [17,32,48,49]. Yet, regardless of the strategy, a pre-processing stage is needed before further data elaboration in order to remove residual noise and possible trends from the vibration signals, filter undesired frequency components, minimize leakage errors and eventually down-sample the time series to reduce the subsequent data processing time.

As for the present work, the pre-processing operation was executed through a Matlab© script, applying a 10<sup>th</sup> order Butterworth low-pass filter to the raw signals. Then, the cleaned data were down-sampled, passing from a spectral resolution of 1024 Hz to 100 Hz. As observed in analogous structures, the frequency content of interest for the tower fell in the range 0-10 Hz, thus data were further decimated with a factor of 8, reducing the analyzed range to 0-12.5 Hz. Finally, the pre-processed signals were analyzed through the Stochastic Subspace Identification (SSI) method available in the commercial software ARTEMIS [50].

### 3.3.2 Theoretical background on SSI-based methods

The SSI method can be considered as one of the principal approaches for the extraction of modal parameters from output-only vibration data. The large attention lately received by SSI methods is likely due to the fact that these techniques are apt to accurately identify closely spaced modes and especially suited to be automated [49]. For the sake of completeness, only a brief description of this modal identification procedure is provided hereafter; for further details the reader is referred to [51].

SSI can be implemented in two classic forms: covariance driven (SSI-cov) and data driven (SSI-data). Working in the time domain, the SSI method starts from the construction of a State Space model, where the second order equation of motion is converted into a system composed of two linear equations, called respectively “state equation” Eq. (1) and “observation equation” Eq. (2), which in the case of ambient vibration testing (unknown input) read:

$$\mathbf{x}_{k+1} = \mathbf{A}\mathbf{x}_k + \mathbf{w}_k \quad (1)$$

$$\mathbf{y}_k = \mathbf{C}\mathbf{x}_k + \mathbf{v}_k \quad (2)$$

where:

- $k$  is the generic time instant;
- $\mathbf{x} \in \mathcal{R}^{n \times 1}$  is the discrete-time state vector;
- $\mathbf{y} \in \mathcal{R}^{l \times 1}$  is the vector containing the  $l$  output measurements;
- $\mathbf{A} \in \mathcal{R}^{n \times n}$  is the system matrix that describes all the dynamic information of the system;
- $\mathbf{C} \in \mathcal{R}^{l \times n}$  is the corresponding output matrix;
- $\mathbf{w} \in \mathcal{R}^{n \times 1}$  is a white noise vector process representing disturbances and modelling inaccuracies;
- $\mathbf{v} \in \mathcal{R}^{l \times 1}$  is another white noise vector process representing the measurement noise due to sensor inaccuracy.

These equations represent the discrete-time state space form of the dynamics of a linear-time-invariant system under unknown excitation. Particularly, Eq. (1) models the dynamic behavior of the physical system, whereas Eq. (2) controls which part of the dynamic system can be observed in the output of the model. The core of the process aims at identifying the system dynamic matrix  $\mathbf{A}$  by fitting the state-



space model to the experimental data. In case of SSI-cov method, the modal estimates are obtained from the Singular Value Decomposition (SVD) of the block Toeplitz matrix, a matrix gathering the covariances of the measured output time series; while in case of SSI-data, the modal identification is performed starting from the SVD of the block Hankel matrix, a matrix containing past and future output measurements.

Like all parametric system identification techniques, a user-defined integer is required to process the data, i.e. the maximum model order. In principle, the model order must be twice the number of the modes that are needed to describe the dynamic response of the system. Notwithstanding, to identify weakly excited modes, it is often necessary to consider larger model orders which can lead in turn to the appearance of many spurious modes associated to the noise content of the measurements. To overcome this issue, different SSI analyses with a range of candidate model orders can be carried out trying to identify the model order that better fits the experimental data and leads to the best stabilization diagram. The latter is an order-frequency plot in which the estimated physical (structural) and computational (spurious) modes are represented as poles and discriminated based on the fulfilment of user-specified requirements (e.g. maximum allowed deviation between successive models in terms of modal frequencies, damping ratios and MAC values). If the model order is high enough, a repeated trend of stable poles will appear in the SSI output diagram, allowing the estimation of the structural modes characterizing the system.

### 3.3.3 Modal results

In both dynamic testing campaigns, five vibration modes were identified in the frequency range 0-10 Hz: two close-spaced translational modes ( $\varphi_1$ ) and ( $\varphi_2$ ) in  $x$  and  $y$  directions, respectively, featuring in-phase modal components; one torsion mode ( $\varphi_3$ ); and two dominant double bending modes ( $\varphi_4$ ), ( $\varphi_5$ ) in the  $xz$  and  $yz$  planes, respectively. As expected, the first two vibration modes exhibit relatively high frequency values compared to those featured by typical historical masonry towers. This outcome is imputable to the low aspect ratio ( $\lambda = 4$ ) characterizing the tower object of study as well as to the increased stiffness resulted from the past restoration works.

The estimated natural frequencies and damping ratios, used for the following calibration process, are reported in Table 1 for both campaigns, together with the Mode Complexity Factor (MCF) associated to each mode. This value is a scalar that lies in the range 0%-100% and quantifies the degree of complexity of a mode shape, namely how much the modal vector differs from a real-valued one [52–54]. Real-valued mode shapes feature complexities close to 0 (MCF = 0%), while mode shapes with predominant imaginary components exhibit complexity values close to 1 (MCF = 100%). The dispersion of the real and imaginary parts of each mode is further analysed by plotting their components in a two-dimensional polar coordinate system, namely through the complexity plots, as illustrated in Figure 7. It is observed that in the first dynamic testing campaign, the first three mode shapes, as well as the last one, are close to monophasic vectors (components are aligned along the horizontal direction) and only the fourth mode has a higher complexity, whereas in the second dynamic testing campaign the modal components of both the third and fourth modal vectors present greater complexities. This slight difference between the MCF values of the two campaigns is probably associated to the different level of ambient excitations present during the AVTs which might have affected the signal-to-noise ratio introducing some inaccuracy in the modal estimates. However, it is worth mentioning that the actual mode shapes of a physical system are never exactly monophasic vectors, thus some degree of complexity is always expected in the experimental modes.

Table 1 – Global modal parameters identified for EM 2018 and EM 2019.

Mode	<u>2018</u>			<u>2019</u>		
	$f$ [Hz]	$\xi$ [%]	MCF [%]	$f$ [Hz]	$\xi$ [%]	MCF [%]
$\varphi_1$	2.082	0.817	3.929	2.092	0.762	3.320
$\varphi_2$	2.156	0.893	0.178	2.165	0.787	0.370
$\varphi_3$	6.293	0.578	2.765	6.302	0.666	11.241
$\varphi_4$	6.442	2.423	12.471	6.449	3.397	19.642
$\varphi_5$	6.941	2.463	2.053	6.872	2.739	4.851

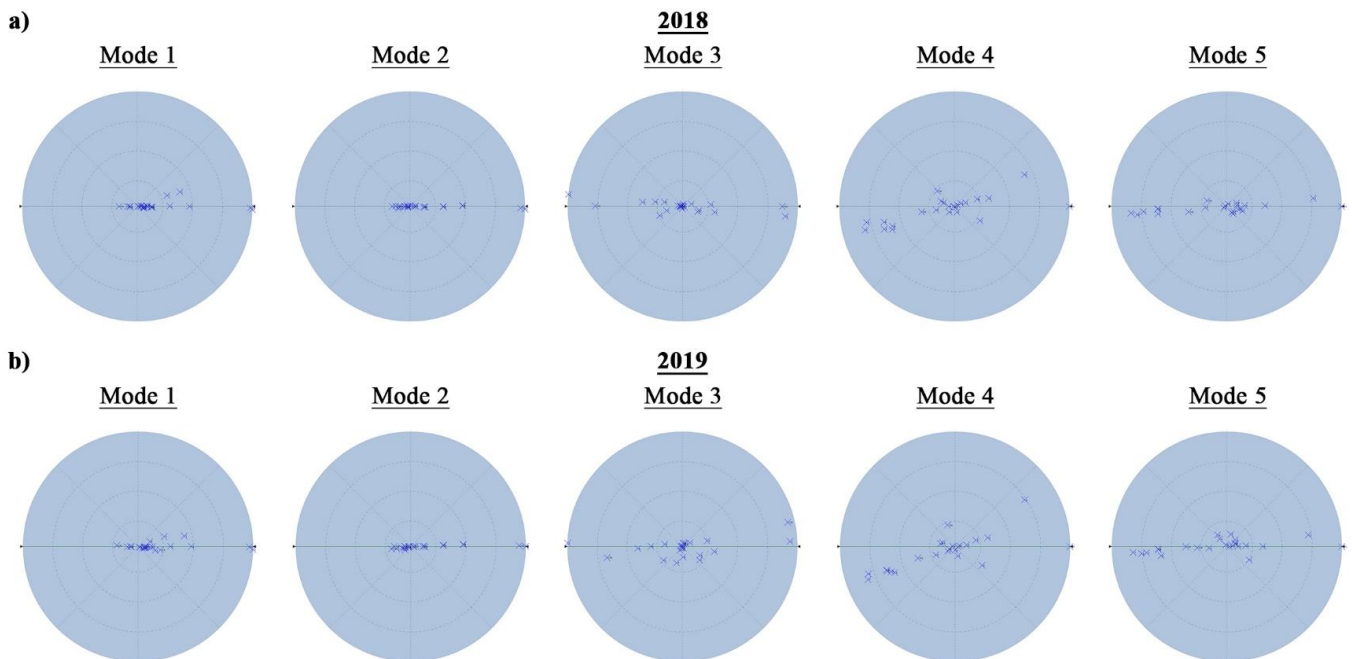


Figure 7 - Complexity plots of the identified experimental modes for EM 2018 (a) and EM 2019 (b).

To drive the accurate selection of the structural modes, a cross-validation was performed by comparing the modes identified with the SSI modal estimator against the ones extracted through another OMA technique operating in the frequency domain, namely the Enhanced Frequency Domain Decomposition (EFDD) [55,56]. The close pairwise correspondence of the five vibration modes estimated in each campaign is visually highlighted in Figure 8, where the mode shapes from the two modal estimators are superimposed, and also confirmed by the values of the Modal Assurance Criterion (MAC) reported both in Figure 8 and in Table 2. As well-known in the literature, the MAC is a statistical indicator used to measure the degree of similarity between mode shape vectors [57]: the closer the values are to 1 (MAC = 100%), the higher the correlation between modes and vice versa.

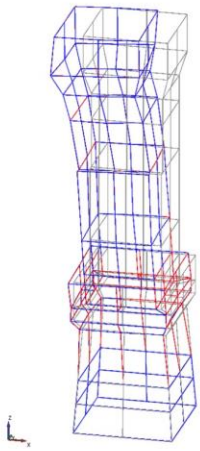
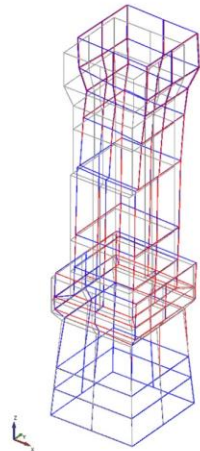
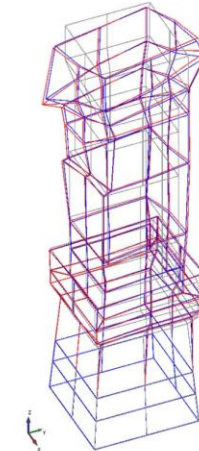
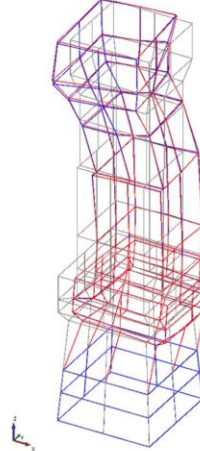

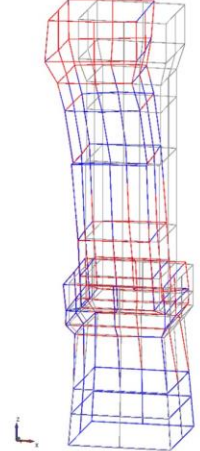
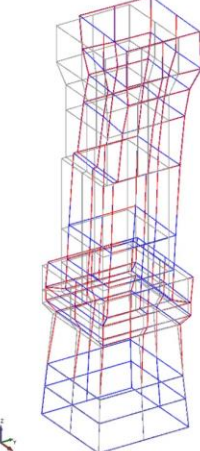
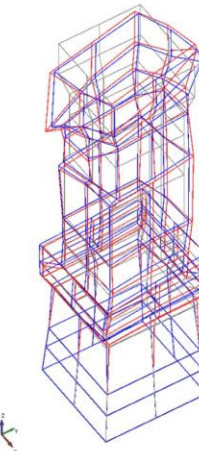
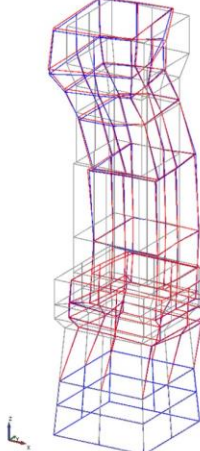
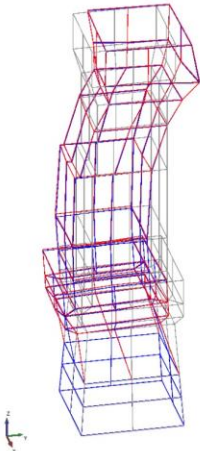
<b>2018</b>				
<b>Mode 1</b> $f_{SSI} = 2.082$ Hz $f_{EFDD} = 2.082$ Hz	<b>Mode 2</b> $f_{SSI} = 2.156$ Hz $f_{EFDD} = 2.155$ Hz	<b>Mode 3</b> $f_{SSI} = 6.293$ Hz $f_{EFDD} = 6.305$ Hz	<b>Mode 4</b> $f_{SSI} = 6.442$ Hz $f_{EFDD} = 6.459$ Hz	<b>Mode 5</b> $f_{SSI} = 6.941$ Hz $f_{EFDD} = 6.950$ Hz
				
Translational X	Translational Y	Torsional	Bending X	Bending Y
MAC <sub>SSI-EFDD</sub> = 100%	MAC <sub>SSI-EFDD</sub> = 99.8%	MAC <sub>SSI-EFDD</sub> = 86.7%	MAC <sub>SSI-EFDD</sub> = 92.4%	MAC <sub>SSI-EFDD</sub> = 98.0%
<b>2019</b>				
<b>Mode 1</b> $f_{SSI} = 2.092$ Hz $f_{EFDD} = 2.090$ Hz	<b>Mode 2</b> $f_{SSI} = 2.165$ Hz $f_{EFDD} = 2.165$ Hz	<b>Mode 3</b> $f_{SSI} = 6.302$ Hz $f_{EFDD} = 6.301$ Hz	<b>Mode 4</b> $f_{SSI} = 6.449$ Hz $f_{EFDD} = 6.443$ Hz	<b>Mode 5</b> $f_{SSI} = 6.872$ Hz $f_{EFDD} = 6.893$ Hz
				
Translational X	Translational Y	Torsional	Bending X	Bending Y
MAC <sub>SSI-EFDD</sub> = 99.9%	MAC <sub>SSI-EFDD</sub> = 99.7%	MAC <sub>SSI-EFDD</sub> = 81.2%	MAC <sub>SSI-EFDD</sub> = 89.1%	MAC <sub>SSI-EFDD</sub> = 94.3%

Figure 8 - Mode shapes of 2018 and 2019 EMs identified with SSI method (in blue) and cross-comparison with the respective mode shapes identified with EFDD method (in red).

Table 2 - MAC between mode shapes identified with SSI and EFDD methods: (a) EM 2018 and (b) EM 2019.

Cross-MAC 2018		SSI				
		2.082 Hz	2.156 Hz	6.293 Hz	6.442 Hz	6.941 Hz
EFDD	2.082 Hz	1.000	0.000	0.000	0.032	0.002
	2.155 Hz	0.002	0.998	0.001	0.000	0.024
	6.305 Hz	0.003	0.002	0.867	0.028	0.001
	6.459 Hz	0.036	0.000	0.039	0.924	0.021
	6.950 Hz	0.001	0.026	0.002	0.010	0.980

Cross-MAC 2019		SSI				
		2.092 Hz	2.165 Hz	6.302 Hz	6.449 Hz	6.872 Hz
EFDD	2.090 Hz	0.999	0.001	0.001	0.034	0.003
	2.165 Hz	0.003	0.997	0.002	0.000	0.027
	6.301 Hz	0.004	0.002	0.812	0.006	0.003
	6.443 Hz	0.034	0.001	0.061	0.891	0.020
	6.893 Hz	0.002	0.028	0.002	0.008	0.943



Analysing in depth the global modal parameters estimated in 2018 and 2019, no significant change is found in terms of frequency values ( $f$ ) as the percentage variations recorded between corresponding modes are less than or equal to 1.0% (Table 3), meaning that the global dynamic behaviour of the tower remained unchanged in the period elapsed between the two campaigns. As concerns modal damping ( $\xi$ ), relatively high percentage variations are found when comparing the damping ratios of corresponding modes between 2018 and 2019, with a maximum difference greater than 20% for the 4<sup>th</sup> mode (Table 3). Unlike frequencies, damping values are much more prone to be affected by measurement uncertainties and random error sources. Still, all the estimated values are consistently under 5% in each campaign, allowing to infer that, in the present case, the observed scatter is not associated with incipient damage mechanisms, but it is related to the intrinsic complex nature of this modal parameter.

Table 3 - Percentage variation between modal frequencies and damping ratios of EM2018 and EM2019.

Mode	$f_{EM18}$ [Hz]	$\xi_{EM18}$ [%]	$f_{EM19}$ [Hz]	$\xi_{EM19}$ [%]	$\Delta f$ [%]	$\Delta \xi$ [%]
$\varphi_1$	2.082	0.817	2.092	0.762	0.478	-7.218
$\varphi_2$	2.156	0.893	2.165	0.787	0.416	-13.469
$\varphi_3$	6.293	0.578	6.302	0.666	0.143	13.213
$\varphi_4$	6.442	2.423	6.449	3.397	0.109	28.672
$\varphi_5$	6.941	2.463	6.872	2.739	-1.004	10.077

In what concerns the experimental mode shapes estimated from 2018 and 2019 AVT data (Figure 9), their configuration is consistent over time and clearly points out the typical behavior of a monolithic cantilever beam with rigid constraint at the base. The principal components of displacement result well-defined for each mode and a nearly perfect correlation is found between corresponding mode pairs. The cross-validation process operated through the MAC matrix (Table 4) also proves the modes to be consistent, well-decoupled and accurately identified from both field campaigns.

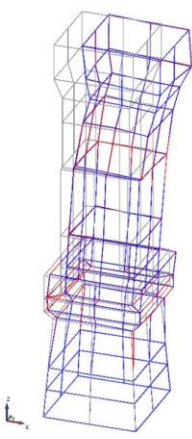
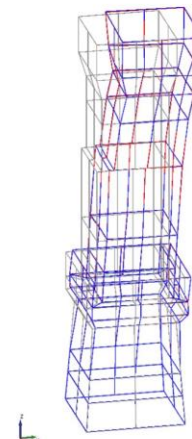
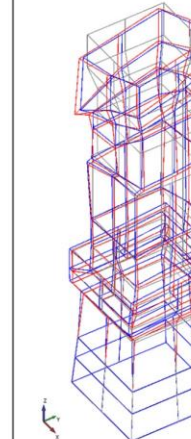
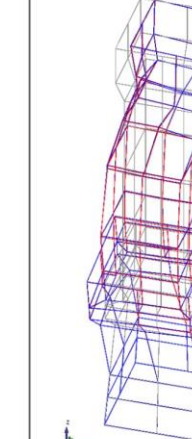
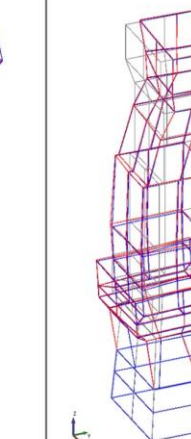
Mode 1	Mode 2	Mode 3	Mode 4	Mode 5
$f_{SSI2018} = 2.082$ Hz $f_{SSI2019} = 2.092$ Hz	$f_{SSI2018} = 2.156$ Hz $f_{SSI2019} = 2.165$ Hz	$f_{SSI2018} = 6.293$ Hz $f_{SSI2019} = 6.302$ Hz	$f_{SSI2018} = 6.442$ Hz $f_{SSI2019} = 6.449$ Hz	$f_{SSI2018} = 6.941$ Hz $f_{SSI2019} = 6.872$ Hz
				
Translational X	Translational Y	Torsional	Bending X	Bending Y
MAC = 99.2%	MAC = 99.5%	MAC = 98.1%	MAC = 99.0%	MAC = 97.1%

Figure 9 - Comparison between mode shapes of EM 2018 (in blue) and the corresponding ones of EM 2019 (in red).

Table 4 - MAC between EMs mode shapes identified with SSI method.

CrossMAC 2018-2019		EM19				
		2.092 Hz	2.165 Hz	6.302 Hz	6.449 Hz	6.872 Hz
EM18	2.082 Hz	0.992	0.000	0.001	0.037	0.001
	2.156 Hz	0.003	0.995	0.004	0.001	0.026
	6.293 Hz	0.002	0.000	0.981	0.077	0.018
	6.442 Hz	0.030	0.000	0.110	0.990	0.010
	6.941 Hz	0.005	0.025	0.009	0.002	0.971

#### 4. Numerical modelling and updating via Genetic Algorithm

The uniqueness and complexity of heritage structures make the understanding of their actual behaviour a true challenge. By updating FE models with OMA information, one can reproduce as closely as possible the measured response of the structure and carry out a reliable condition assessment. The process consists in updating the system matrices of the FE model (mass, stiffness and possibly damping matrices) till the difference between experimental and numerical modal data is minimized. If the FE model is not adequately representative of the reality, structural assessment cannot be performed.

Despite the degree of maturity of existing modal-based updating techniques for the calibration of realistic numerical models, experience has shown that the updating process is not trivial especially when trying to upgrade these procedures for damage localization purposes [58,59]. First and foremost, the FE model for updating requires a level of detail sufficient enough to represent both geometric and structural forms. Moreover, the number of parameters to update should be selected in order to guarantee a well-conditioned problem, independent of the contingent state of the structure and easily replicable in nearly real-time to evaluate possible global and local changes with respect to the reference modal data. The determination of reasonable initial values for the updating parameters, together with the definition of their lower and upper bounds, also plays an important role to guarantee the convergence of the iterative process and the physical significance of the final updated parameters.

Rooted in these considerations, a modal-based updating procedure relying on Genetic Algorithms (GA) is hereafter presented and employed to calibrate a realistic FE model of the masonry tower under investigation and establish baseline information for future comparative analyses at global and local level.

##### 4.1 Preliminary FE model

An initial 3D FE model (NM<sub>0</sub>) of the tower was built using MidasFea© in order to preliminary assess the meaningful dynamic characteristics of the structure. The peculiar geometry of the tower, which is one of the parameters that mostly affects its global dynamic response, required a very high degree of detail in the modelling process of the different elements and construction features like openings, wall thickness, geometrical irregularities, etc. Particular attention was given to the reproduction of the rubble-filled masonry of the basement of the tower as well as to the concrete floors of the higher levels which were considered as rigid diaphragms in their plane. As concerns secondary elements, like stairs, deformable wooden floors, clock mechanism and bells, they were not explicitly modelled, but their influence was accounted for as added masses.

Once the geometry of the tower was defined (Figure 10), all the solids composing the model were discretized as 4-node tetrahedral elements, whose mesh size was set equal to 0.3 m, resulting into a

model with 21,726 nodes, 78,926 volume elements and 67806 DOFs. Considering the tower as a cantilever beam, rigid constraints were applied at the base.

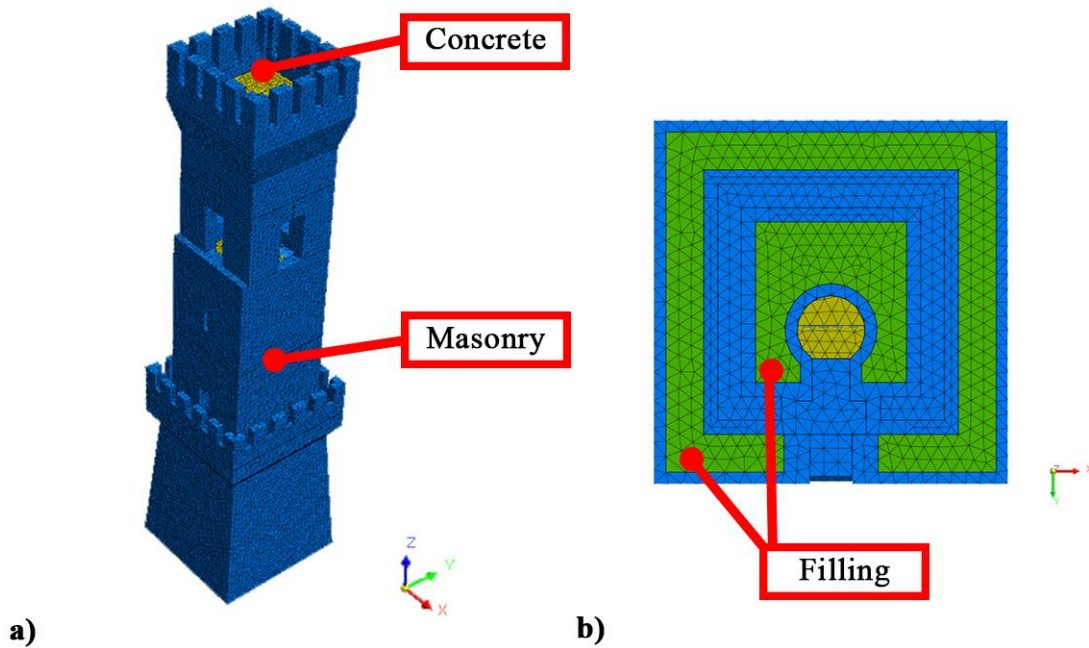


Figure 10 – FE modelling of the Civic Tower of Ostra:  
 (a) Assonometric view, (b) Bottom view at foundation level

At first, a three-group material discretization was applied, modelling each material as homogeneous and isotropic, with Young’s modulus ( $E$ ), Poisson’s ratio ( $\nu$ ) and mass density ( $\gamma$ ) chosen according to the Italian Technical Standards for Structures [60]. The initial values assumed for the afore-mentioned elastic parameters are reported in Table 5. It is noticed that in the definition of the elastic modulus of the concrete, a 30% reduction was considered, because of the uncertainties linked to aging effects, while for the rubble masonry properties the values suggested in the Italian code [60] for irregular masonry were assigned.

Table 5 - Elastic properties of the initial FE model.

Material	$E$ [MPa]	$\nu$ [-]	$\gamma$ [kN/m <sup>3</sup> ]
Masonry	1800	0.20	18
Concrete	18000	0.20	25
Filling	1100	0.20	18

A preliminary modal analysis, implemented through the Lanczos method [30,61–63], was carried out on the initial FE model to evaluate the dynamic properties of the tower and quantify the residuals between numerical and experimental modal parameters. The results from this first step are reported in Table 6, where the remarkable differences between actual experimental frequencies (EM) and calculated numerical frequencies (NM<sub>0</sub>) of the not yet calibrated model are highlighted.



Table 6 – Preliminary numerical results ( $NM_0$ ) and differences with the experimental frequency values ( $EM$ ).

Mode	$f_{NM0}$ [Hz]	$T_{NM0}$ [s]	Eff. Mass Direction X [%]	Eff. Mass Direction Y [%]	$f_{EM18}$ [Hz]	$f_{EM19}$ [Hz]	$ \Delta f_{EM18-NM0} $ [%]	$ \Delta f_{EM19-NM0} $ [%]
$\varphi_1$	1.509	0.663	35.80	0.00	2.082	2.092	27.52	27.87
$\varphi_2$	1.536	0.651	0.00	35.72	2.156	2.165	28.76	29.05
$\varphi_3$	5.012	0.200	0.02	0.00	6.293	6.302	20.36	20.47
$\varphi_4$	5.821	0.172	21.21	0.00	6.442	6.449	9.64	9.74
$\varphi_5$	5.883	0.170	0.00	29.38	6.941	6.872	15.24	14.39

With respect to the mode shapes (Figure 11), their main displacement components present a good visual correlation with their experimental counterpart, being the first two modes translational in the  $x$  and  $y$  direction, respectively, the third mode a torsional one, and the last two being dominant bending modes in the  $xz$  and  $yz$  planes.

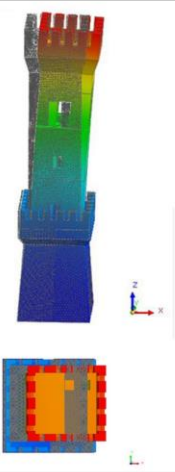
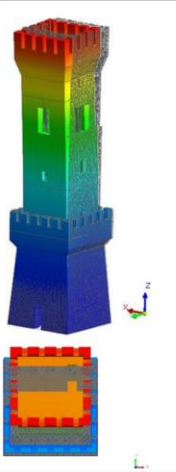
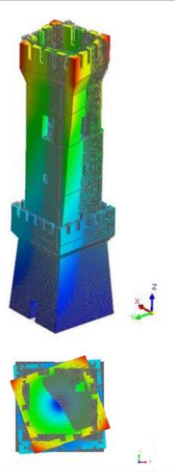
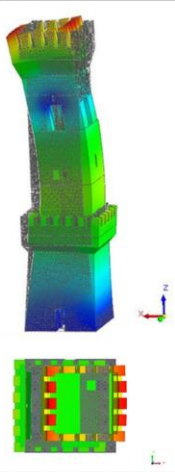
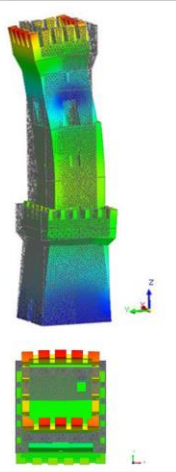
Mode 1 $f = 1.509$ Hz	Mode 2 $f = 1.536$ Hz	Mode 3 $f = 5.012$ Hz	Mode 4 $f = 5.821$ Hz	Mode 5 $f = 5.883$ Hz
				
Translational X	Translational Y	Torsional	Bending X	Bending Y
$MAC_{NM0-EM18} = 77.6\%$ $MAC_{NM0-EM19} = 82.5\%$	$MAC_{NM0-EM18} = 81.5\%$ $MAC_{NM0-EM19} = 67.2\%$	$MAC_{NM0-EM18} = 22.1\%$ $MAC_{NM0-EM19} = 2.6\%$	$MAC_{NM0-EM18} = 52.2\%$ $MAC_{NM0-EM19} = 47.6\%$	$MAC_{NM0-EM18} = 1.1\%$ $MAC_{NM0-EM19} = 44.7\%$

Figure 11 - Frequencies values and mode shapes resulting from modal analysis operated on the preliminary FE model.

On the other hand, the comparison of the degree of consistency between numerical and experimental modal vectors in terms of MAC values (Table 7) shows a fair correlation only for the first two fundamental modes of the tower, while higher modes feature quite a poor (4<sup>th</sup> and 5<sup>th</sup> modes) or no (3<sup>rd</sup> mode) correlation either using 2018 or 2019 modal data as comparative metric.

Table 7 - MAC between numerical and experimental mode shapes: (a) NM0-EM 2018 and (b) NM0-EM 2019. NM0 stands for preliminary numerical model.

		a)					b)				
		EM18					EM19				
Cross-MAC		2.082 Hz	2.156 Hz	6.293 Hz	6.442 Hz	6.941 Hz	2.092 Hz	2.165 Hz	6.302 Hz	6.449 Hz	6.872 Hz
NM0	1.509 Hz	0.776	0.023	0.016	0.038	0.003	0.825	0.025	0.000	0.066	0.005
	1.536 Hz	0.002	0.815	0.002	0.002	0.040	0.001	0.672	0.007	0.003	0.026
	5.012 Hz	0.004	0.006	0.221	0.000	0.003	0.050	0.038	0.026	0.029	0.029
	5.821 Hz	0.010	0.000	0.054	0.522	0.011	0.005	0.003	0.031	0.476	0.020
	5.883 Hz	0.042	0.007	0.091	0.019	0.650	0.005	0.025	0.124	0.000	0.447

## 4.2 GA-based model updating

As mentioned in the Introduction, iterative model updating procedures aim at calibrating an FE model through the solution of an inverse problem based on modal analysis, where corrections are applied to local physical and/or mechanical parameters of the FE model by setting an objective function and searching for the optimum solution till the difference between experimental and numerical modal data is minimized. To overcome the limitations inherently associated to manual or approximate updating processes, a genetic algorithm (GA) implemented in Code\_Aster© software environment [64] was used in this work to calibrate the FE model of Ostra Civic Tower.

The genetic algorithms are inspired by Darwin's theory and are based on the process of natural selection. These algorithms are considered robust tools for solving optimization problems and explore diverse regions of interest by running the same problem on different conditions and allowing to locate with high probability the global optimum without getting trapped into local minima [29,30,65,66]. They are part of a stochastic method that "mimics" the evolution through combinations of random mutations and natural selection in order to find optimal numerical values of functions. A better understanding of the methodology can be achieved through the description of the updating process scheme as it was implemented.

NM and EM were initially imported and read by Code\_Aster©, where a condensed experimental model (CEM) containing the frequency and mode shape data belonging to the five estimated modes was created. Then, CEM data were projected onto the NM (Figure 12) in order to upscale the EM DOFs. This operation enabled the possibility to visualize and interact with the data onto a 3D model while also creating the dependencies for the displacement calculations between the existing nodes of the NM with respect to the data of the EM.

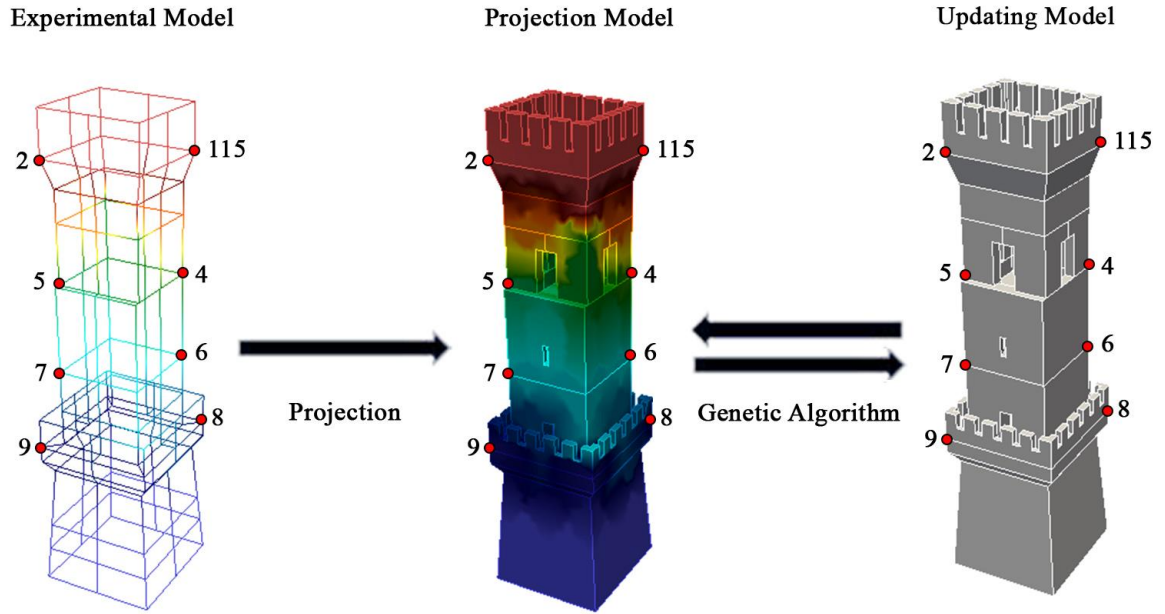


Figure 12 - Workflow for the projection of the experimental data onto the NM for the genetic algorithm updating, with measured nodes highlighted.

Once the projection was done, a preliminary modal analysis was performed, generating the initial population for the values of the unknown material properties to be considered in the calibration process. Upper and lower bounds of physical significance were also set for each updating parameter based on values retrieved from the literature and belonging to analogous structures. Any value within the bounds was a candidate solution.

For each iteration, the fulfilment of convergence criteria established beforehand was progressively checked using a very strict two-term objective function that accounted for both frequencies and mode shapes residuals between EM and NM models, as reported below:

$$\Delta f + \Delta_{crossMAC} = \sqrt{\sum_{i=1}^n \left( \frac{f_{exp}^i - f_{num}^i}{f_{exp}^i} \right)^2} + \sqrt{\sum_{i=1}^n (1 - MAC^i)^2} \leq 0.05 \quad (3)$$

The model updating process was set to stop either when the residual tolerance of two consecutive steps reached  $1e^{-4}$  or after 2000 evaluations (Figure 13), hence ensuring the stability of the iterative solution.

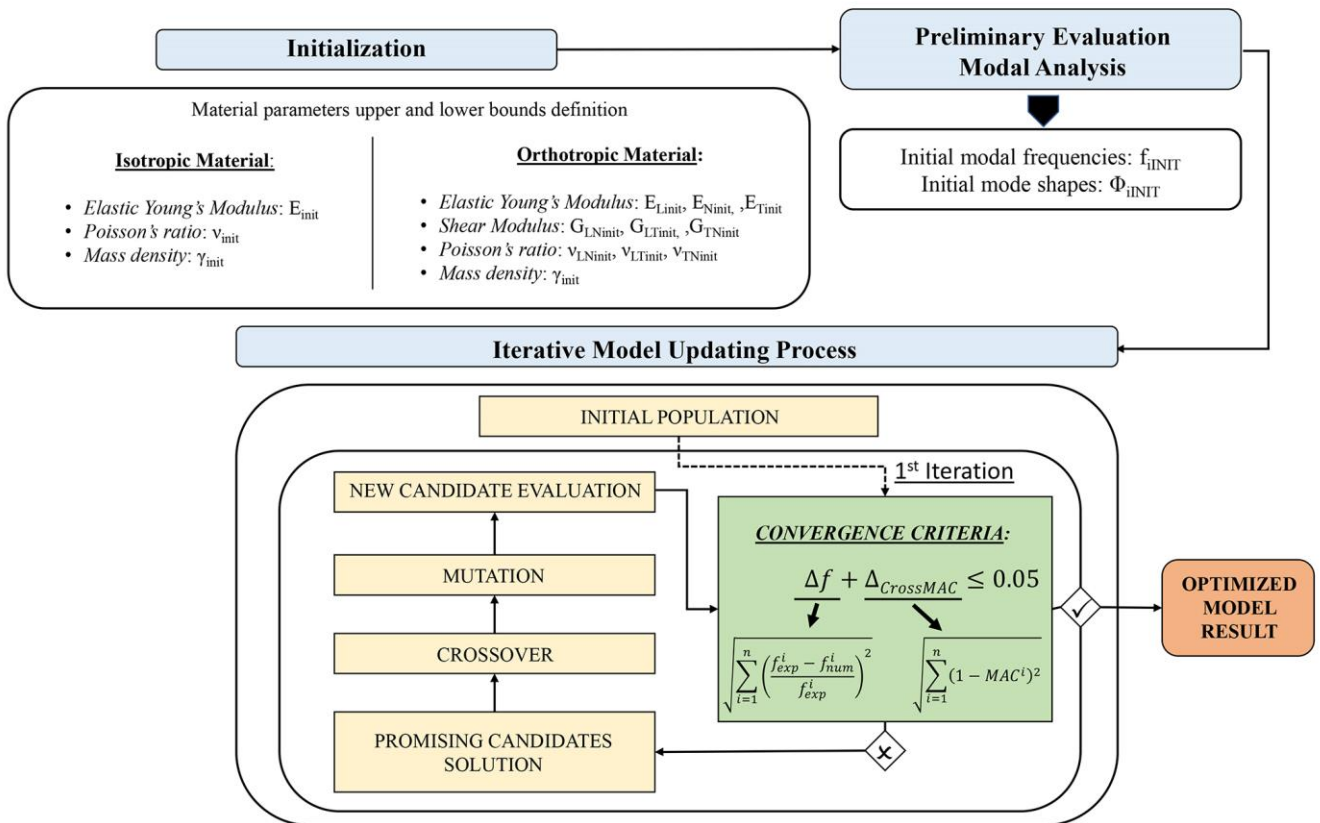


Figure 13 - GA-based model updating flowchart.

## 4.3 Calibration process

### 4.3.1 Twelve-group discretization approach

To account for the visible variability of the masonry properties across the tower and better tune the model dynamic response, the number of updating parameters was increased by further discretizing the preliminary FE model into twelve parts, or solid groups (Figure 14). The GA-based updating process was then repeated by employing as reference modal data the frequencies and MAC values of the five vibration modes estimated from both the 2018 and 2019 AVT measurements, and iteratively varying the elastic parameters assigned to each of the twelve parts till the residuals between numerical and experimental modal data were minimized. The final number of updating parameters thus greatly exceeded the initial number considered in the preliminary assessment.



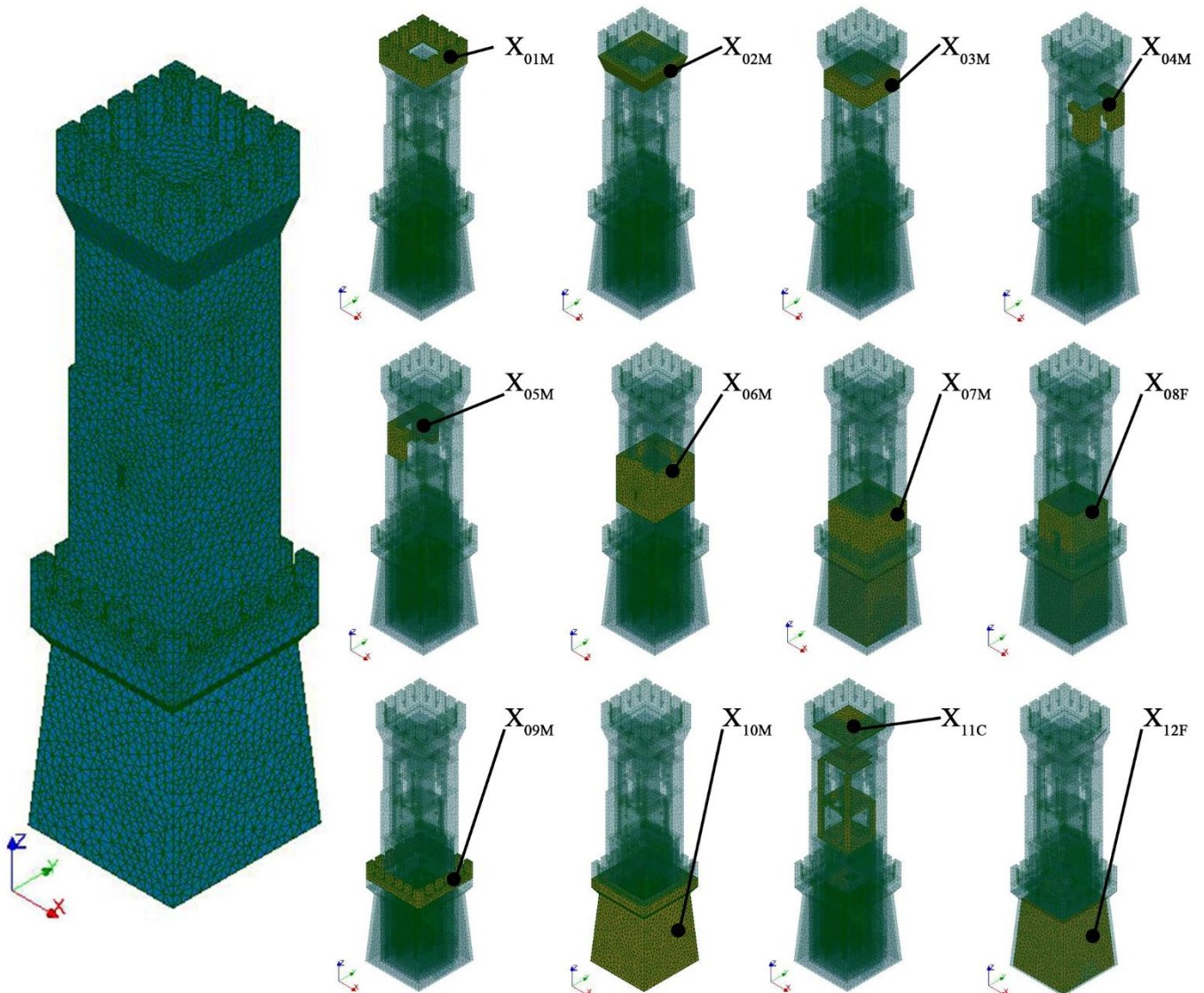


Figure 14 – Updating variables for the twelve-group discretization of the FE model. Each material group is named as “X” followed by a subscript composed by a number (from 00 to 12) which stands for the group and a letter (“M” is masonry, “C” is concrete and “F” is the filling material).

The elastic properties of the twelve parts were attributed considering two different behavioural models for the materials: in the first stage all materials were modelled as homogeneous and isotropic, requesting the solution of a thirty-six parameters convergence problem ( $3 \times 12 = 36$ ), whereas in the second stage the masonry material was modelled as orthotropic due to its complex and non-homogeneous internal structure, leading to the calibration of one hundred-thirteen updating parameters (masonry:  $10 \times 11 = 110$ ; concrete:  $3 \times 1 = 3$ ). It is remarked how the complexity and high dimensionality of the optimization problem could not be tackled via a manual updating procedure but required a sophisticated algorithm capable of dealing with large and multi-dimensional problems. Reasonable variation ranges for the material parameters were assigned to each part in accordance with the values provided by the Italian Technical Standards for Structures [60] as well as with the values retrieved from the literature for analogous materials and in light of the outcome of the condition survey. The established upper and lower bounds [67–69] are summarized in Table 8 and Table 9 for the isotropic and orthotropic cases, respectively. The initial population of updating variables used in the GA-based updating process was randomly selected within these bounds.

Table 8 – Lower and upper bounds for isotropic elastic properties ( $E$  is the Elastic Young's Modulus,  $\nu$  is the Poisson's ratio and  $\gamma$  is the mass density).

Material	E	$\nu$	$\gamma$
	[MPa]	[-]	[kN/m <sup>3</sup> ]
	Min - Max	Min - Max	Min - Max
Masonry	600 - 3300	0.01 – 0.45	15 - 20
Filling	600 - 2400	0.01 - 0.45	15 - 20
Concrete	27000 - 32000	0.01 – 0.45	23 - 26

Table 9 – Lower and upper bounds for orthotropic elastic properties ( $G$  is the shear Modulus, while the subscripts  $L$ ,  $N$  and  $T$  indicate Longitudinal, Normal and Tangential components respectively).

(\*) Concrete stayed as isotropic material.

Material	$E_L$	$E_N$	$E_T$	$G_{LN}$	$G_{LT}$	$G_{TN}$	$\nu_{LN}$	$\nu_{LT}$	$\nu_{TN}$	$\gamma$
	[MPa]	[MPa]	[MPa]	[MPa]	[MPa]	[MPa]	[-]	[-]	[-]	[kN/m <sup>3</sup> ]
	Min-Max	Min-Max	Min-Max	Min-Max	Min-Max	Min-Max	Min-Max	Min-Max	Min-Max	Min-Max
Masonry	600-3300	600-3300	600-3300	230-1400	230-1400	230-1400	0.01-0.45	0.01-0.45	0.01-0.45	15-20
Filling	600-2400	600-2400	600-2400	230-1400	230-1400	230-1400	0.01-0.45	0.01-0.45	0.01-0.45	15-20
Concrete	27000-32000			(automatically calculated)				0.01-0.45		23-26

The main scope of this GA-based model updating procedure, run first considering 36 variables (isotropic material) and then accounting for 113 unknowns (orthotropic material), was to produce a refined baseline model closely representative of the initial experimental target and that could be speedily updated with new data to serve as a future digital twin of the physical structure for predicting its performance against different scenarios. Hence the need of collecting data from two distinct AVT campaigns. In the second updating phase against 2019 experimental data, an in-depth sensitivity analysis [70,71], whose results are illustrated and widely discussed in APPENDIX A - Evaluation of the influence of material parameters in automatic calibration, was also conducted to evaluate the influence of every single material parameter on the outcome of the updating process. In light of the results, although reducing the number of unknowns is common practice in the literature [35], it was decided to continue calibrating the model through the proposed GA-based procedure and keep all the afore-mentioned parameters as updating variables, given the greater computational efficiency of the proposed method and considering this the only solution for a future extent of this study to the damage localization field.

#### 4.3.2 Model updating results

The optimal mechanical parameters obtained downstream the GA-based updating process of the isotropic FE model of Ostra Civic Tower are reported in Table 10. It is interesting to notice that the final values of the material properties are consistent with the expected ranges and clearly reflect the visible masonry changes resulting from past interventions and restoration works. Particularly, the Young's moduli of the masonry tend to decrease from the basement (reinforced during the 1950s restoration works) to the central body (which was only partially reconstructed) and increase again towards the upper part of the tower (added later), reading values consistent with those reported in the Italian code [60].

Table 10 – Optimal values for the material parameters of the isotropic FE models after calibration and successive updating.

Updating parameter	2018 NM			2019 NM		
	E [MPa]	$\nu$ [-]	$\gamma$ [kN/m <sup>3</sup> ]	E [MPa]	$\nu$ [-]	$\gamma$ [kN/m <sup>3</sup> ]
X <sub>01M</sub>	2036	0.18	15	2092	0.17	15
X <sub>02M</sub>	2112	0.22	15	1960	0.24	15
X <sub>03M</sub>	1278	0.21	15	1074	0.22	15
X <sub>04M</sub>	1325	0.20	16	1220	0.20	16
X <sub>05M</sub>	1267	0.23	15	1113	0.28	15
X <sub>06M</sub>	2471	0.18	20	3133	0.17	20
X <sub>07M</sub>	3289	0.19	20	3288	0.19	20
X <sub>08F</sub>	2396	0.18	20	2399	0.18	20
X <sub>09M</sub>	2667	0.19	20	2521	0.17	20
X <sub>10M</sub>	3052	0.20	20	3282	0.21	20
X <sub>11C</sub>	27615	0.26	24	27037	0.25	23
X <sub>12F</sub>	1681	0.21	20	1470	0.21	20

Analogous observations can be drawn for the updating parameters calibrated through the GA-based updating process of the orthotropic FE model of the tower, whose results are reported in Table 11 and Table 12. The optimal values obtained for the elastic moduli of the masonry material feature a similar trend of variation as compared to the isotropic FE model, being consistent with the range of values expected from the visual assessment of the masonry quality. Meaningful values are found as far as the material density is concerned, whereas consistent but slightly larger variations are obtained for the Poisson's ratios.

Table 11 - Optimal values for the material parameters of the orthotropic FE model after calibration against 2018 EM modal data. (\*) Concrete stayed as isotropic material.

Updating parameter	E <sub>L</sub> [MPa]	E <sub>N</sub> [MPa]	E <sub>T</sub> [MPa]	G <sub>LN</sub> [MPa]	G <sub>LT</sub> [MPa]	G <sub>TN</sub> [MPa]	$\nu_{LN}$ [-]	$\nu_{LT}$ [-]	$\nu_{TN}$ [-]	$\gamma$ [kN/m <sup>3</sup> ]
X <sub>01M</sub>	2148	2007	1784	1005	894	970	0.20	0.19	0.19	15
X <sub>02M</sub>	2188	2238	2125	679	911	981	0.18	0.20	0.20	15
X <sub>03M</sub>	2449	1877	1726	552	784	663	0.20	0.28	0.19	15
X <sub>04M</sub>	1800	1033	1941	625	939	999	0.21	0.19	0.18	15
X <sub>05M</sub>	1822	1343	2103	627	825	415	0.18	0.18	0.17	15
X <sub>06M</sub>	1607	2091	2439	1258	1168	1077	0.17	0.19	0.16	19
X <sub>07M</sub>	2300	3248	2410	1357	988	1392	0.19	0.19	0.20	20
X <sub>08F</sub>	1974	2387	2283	515	511	712	0.20	0.20	0.18	20
X <sub>09M</sub>	2079	1898	2074	1034	1116	870	0.19	0.17	0.20	20
X <sub>10M</sub>	1700	2978	2322	972	991	991	0.22	0.16	0.21	20
*X <sub>11C</sub>		27345		(automatically calculated)				0.31		24
X <sub>12F</sub>	2007	2212	2118	345	558	748	0.17	0.19	0.20	20

Table 12 - Optimal values for the material parameters of the orthotropic FE model after updating with 2019 EM modal data. (\*) Concrete stayed as isotropic material.

Updating parameter	$E_L$ [MPa]	$E_N$ [MPa]	$E_T$ [MPa]	$G_{LN}$ [MPa]	$G_{LT}$ [MPa]	$G_{TN}$ [MPa]	$\nu_{LN}$ [-]	$\nu_{LT}$ [-]	$\nu_{TN}$ [-]	$\gamma$ [kN/m <sup>3</sup> ]
X <sub>01M</sub>	2145	2031	1908	946	916	1022	0.21	0.20	0.20	15
X <sub>02M</sub>	2121	2397	1882	636	950	996	0.18	0.20	0.21	15
X <sub>03M</sub>	2294	1909	1761	460	725	614	0.18	0.27	0.19	15
X <sub>04M</sub>	1682	967	1946	564	924	1036	0.22	0.19	0.17	15
X <sub>05M</sub>	1694	1301	2133	528	770	338	0.18	0.17	0.16	15
X <sub>06M</sub>	1615	2092	2230	1374	1122	1221	0.17	0.18	0.16	20
X <sub>07M</sub>	2327	3297	2508	1400	1092	1391	0.19	0.19	0.20	20
X <sub>08F</sub>	1711	2397	2351	563	516	772	0.20	0.21	0.18	20
X <sub>09M</sub>	2048	1956	2143	1038	1116	899	0.20	0.18	0.21	20
X <sub>10M</sub>	1743	3016	2507	1126	1054	1054	0.19	0.16	0.20	20
*X <sub>11C</sub>		27106		(automatically calculated)				0.33		25
X <sub>12F</sub>	2035	2201	2060	330	542	795	0.17	0.20	0.20	20

The frequency results obtained from the modal-based FE model updating of Ostra Civic Tower through GA are exposed in Table 13 and Table 14. For both material modelling approaches, the comparison between EM and NM frequency values is more than satisfactory, being the absolute value of their relative errors always under 4%, with the largest percentage error in correspondence of the 4<sup>th</sup> mode, error that consistently reduces if an orthotropic material is considered for masonry. In general, the orthotropic model allows to better tune the frequencies of the fundamental global modes of the tower and to closely reproduce the frequencies of higher modes, which are notably more sensitive to localized damage.

Table 13 - Comparison between 2018 experimental (EM) and numerical (NM) frequencies for different material modelling approaches and different updating parameters.

Mode	$f_{EM18}$ [Hz]	$f_{NM18}$ [Hz] 36 variables (Isotropic)	$f_{NM}$ [Hz] 113 variables (Orthotropic)	Eff. Mass Direction X [%]	Eff. Mass Direction Y [%]	$ \Delta f_{EM18-NM18} $ [%] (Isotropic)	$ \Delta f_{EM18-NM18} $ [%] (Orthotropic)
$\varphi_1$	2.082	2.070	2.084	34.14	0.01	0.58	0.10
$\varphi_2$	2.156	2.111	2.137	0.01	33.53	2.09	0.88
$\varphi_3$	6.293	6.245	6.284	0.26	0.00	0.76	0.14
$\varphi_4$	6.442	6.693	6.516	29.89	0.11	3.90	1.15
$\varphi_5$	6.941	6.839	6.907	0.12	29.25	1.47	0.49

Table 14 - Comparison between 2019 experimental (EM) and numerical (NM) frequencies for different material modelling approaches and different updating parameters.

Mode	$f_{EM19}$ [Hz]	$f_{NM19}$ [Hz] 36 variables (Isotropic)	$f_{NM19}$ [Hz] 113 variables (Orthotropic)	Eff. Mass Direction X [%]	Eff. Mass Direction Y [%]	$ \Delta f_{EM19-NM19} $ [%] (Isotropic)	$ \Delta f_{EM19-NM19} $ [%] (Orthotropic)
$\varphi_1$	2.092	2.079	2.091	33.94	0.00	0.62	0.05
$\varphi_2$	2.165	2.123	2.143	0.00	33.41	1.94	1.02
$\varphi_3$	6.302	6.277	6.229	0.41	0.06	0.40	1.16
$\varphi_4$	6.449	6.645	6.510	29.22	0.03	3.04	0.95
$\varphi_5$	6.872	6.789	6.930	0.02	28.48	1.21	0.84

The numerical mode shapes corresponding to the FE model calibrated with the optimal values of the material parameters are displayed in Figure 15 and Figure 16. Similar considerations can be drawn in



this case. Indeed, a very good agreement is visually observed between experimental and numerical mode shape configurations: the 1<sup>st</sup> and 2<sup>nd</sup> mode are in-phase translational modes in  $x$  and  $y$  directions, respectively, the 3<sup>rd</sup> mode is torsional, while the 4<sup>th</sup> and 5<sup>th</sup> modes result dominant bending modes in the  $xz$  and  $yz$  planes.

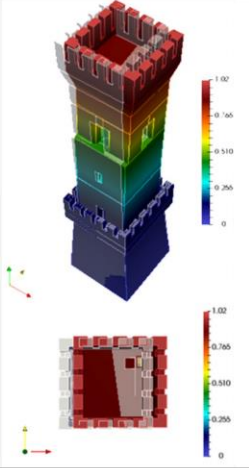
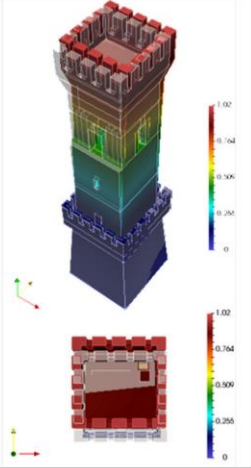
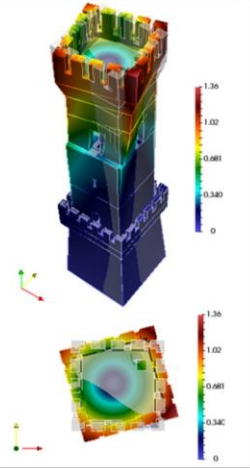
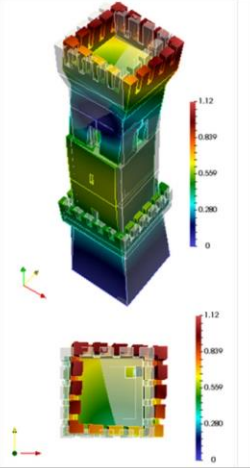
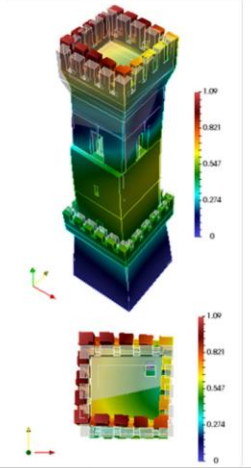
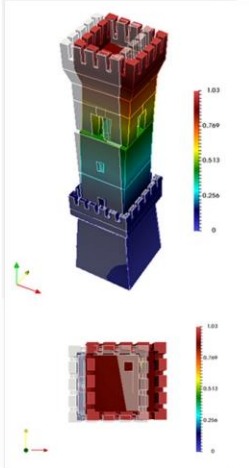
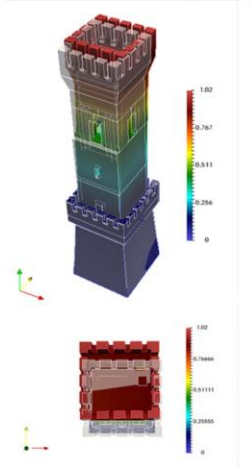
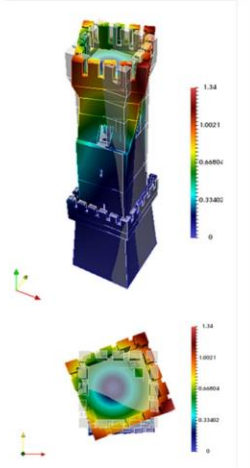
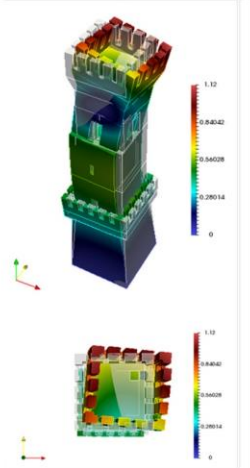
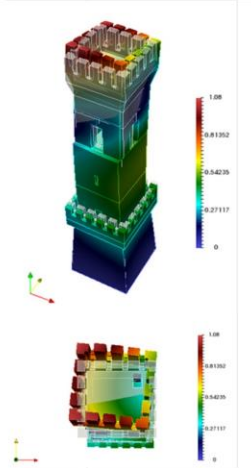
<b>2018</b>				
Mode 1 $f_{NM} = 2.070$ Hz $f_{EM} = 2.082$ Hz	Mode 2 $f_{NM} = 2.111$ Hz $f_{EM} = 2.156$ Hz	Mode 3 $f_{NM} = 6.245$ Hz $f_{EM} = 6.293$ Hz	Mode 4 $f_{NM} = 6.693$ Hz $f_{EM} = 6.442$ Hz	Mode 5 $f_{NM} = 6.839$ Hz $f_{EM} = 6.941$ Hz
				
Translational X	Translational Y	Torsional	Bending X	Bending Y
MAC <sub>NM-EM</sub> = 97.9%	MAC <sub>NM-EM</sub> = 97.3%	MAC <sub>NM-EM</sub> = 97.2%	MAC <sub>NM-EM</sub> = 95.7%	MAC <sub>NM-EM</sub> = 95.3%
<b>2019</b>				
Mode 1 $f_{NM} = 2.079$ Hz $f_{EM} = 2.092$ Hz	Mode 2 $f_{NM} = 2.123$ Hz $f_{EM} = 2.165$ Hz	Mode 3 $f_{NM} = 6.277$ Hz $f_{EM} = 6.302$ Hz	Mode 4 $f_{NM} = 6.645$ Hz $f_{EM} = 6.449$ Hz	Mode 5 $f_{NM} = 6.789$ Hz $f_{EM} = 6.872$ Hz
				
Translational X	Translational Y	Torsional	Bending X	Bending Y
MAC <sub>NM-EM</sub> = 96.5%	MAC <sub>NM-EM</sub> = 96.6%	MAC <sub>NM-EM</sub> = 95.7%	MAC <sub>NM-EM</sub> = 95.8%	MAC <sub>NM-EM</sub> = 95.8%

Figure 15 – Numerical mode shapes after calibration using isotropic material modelling.

<b>2018</b>				
<u>Mode 1</u> $f_{NM} = 2.084$ Hz $f_{EM} = 2.082$ Hz	<u>Mode 2</u> $f_{NM} = 2.137$ Hz $f_{EM} = 2.156$ Hz	<u>Mode 3</u> $f_{NM} = 6.284$ Hz $f_{EM} = 6.293$ Hz	<u>Mode 4</u> $f_{NM} = 6.516$ Hz $f_{EM} = 6.442$ Hz	<u>Mode 5</u> $f_{NM} = 6.907$ Hz $f_{EM} = 6.941$ Hz
Translational X	Translational Y	Torsional	Bending X	Bending Y
MAC <sub>NM-EM</sub> = 98.4%	MAC <sub>NM-EM</sub> = 97.8%	MAC <sub>NM-EM</sub> = 96.8%	MAC <sub>NM-EM</sub> = 96.5%	MAC <sub>NM-EM</sub> = 96.3%
<b>2019</b>				
<u>Mode 1</u> $f_{NM} = 2.091$ Hz $f_{EM} = 2.092$ Hz	<u>Mode 2</u> $f_{NM} = 2.143$ Hz $f_{EM} = 2.165$ Hz	<u>Mode 3</u> $f_{NM} = 6.229$ Hz $f_{EM} = 6.302$ Hz	<u>Mode 4</u> $f_{NM} = 6.510$ Hz $f_{EM} = 6.449$ Hz	<u>Mode 5</u> $f_{NM} = 6.693$ Hz $f_{EM} = 6.872$ Hz
Translational X	Translational Y	Torsional	Bending X	Bending Y
MAC <sub>NM-EM</sub> = 98.1%	MAC <sub>NM-EM</sub> = 98.4%	MAC <sub>NM-EM</sub> = 95.0%	MAC <sub>NM-EM</sub> = 96.1%	MAC <sub>NM-EM</sub> = 95.9%

*Figure 16 – Numerical mode shapes after calibration using orthotropic material modelling.*

The direct cross-validation between EM and NM mode shapes through the MAC further proves the good agreement between experimental and numerical counterparts, being all five modes very well correlated ( $MAC > 95\%$ ) and decoupled, as demonstrated by the low values of the out-of-diagonal elements of the Cross-MAC matrix (Table 15). It is worth highlighting the relevance of the achieved results: in fact, the majority of FE model updating techniques applied in the literature typically result into much higher relative errors between experimental and numerical frequencies and, in the rare instances in which a two-term objective function is adopted, into MAC values sensibly lower than 80% for higher order modes.

Table 15 - CrossMAC between EMs and calibrated NMs considering isotropic and orthotropic materials:  
 (a) NM 2018 with isotropic material, (b) NM 2019 with isotropic material, (c) NM 2018 with orthotropic material, (d)  
 NM 2019 with orthotropic material.

		a)					b)						
		EM18					EM19						
Cross-MAC		2.082 Hz	2.156 Hz	6.293 Hz	6.442 Hz	6.941 Hz	Cross-MAC		2.092 Hz	2.165 Hz	6.302 Hz	6.449 Hz	6.872 Hz
NM18_iso	2.070 Hz	0.976	0.011	0.001	0.018	0.002	NM19_iso	2.079 Hz	0.962	0.016	0.000	0.019	0.000
	2.111 Hz	0.021	0.969	0.000	0.000	0.026		2.123 Hz	0.040	0.963	0.002	0.002	0.027
	6.245 Hz	0.000	0.000	0.972	0.015	0.015		6.277 Hz	0.001	0.000	0.958	0.010	0.024
	6.693 Hz	0.035	0.002	0.011	0.965	0.001		6.645 Hz	0.033	0.001	0.011	0.966	0.002
	6.839 Hz	0.003	0.015	0.005	0.010	0.960		6.789 Hz	0.006	0.017	0.006	0.024	0.960
		c)					d)						
		EM18					EM19						
Cross-MAC		2.082 Hz	2.156 Hz	6.293 Hz	6.442 Hz	6.941 Hz	Cross-MAC		2.092 Hz	2.165 Hz	6.302 Hz	6.449 Hz	6.872 Hz
NM18_Ortho	2.084 Hz	0.981	0.005	0.001	0.018	0.002	NM19_Ortho	2.091 Hz	0.979	0.004	0.000	0.021	0.001
	2.137 Hz	0.013	0.977	0.000	0.000	0.027		2.143 Hz	0.019	0.981	0.003	0.001	0.028
	6.284 Hz	0.000	0.000	0.959	0.014	0.006		6.229 Hz	0.001	0.000	0.963	0.011	0.013
	6.516 Hz	0.033	0.002	0.013	0.957	0.005		6.510 Hz	0.031	0.001	0.009	0.971	0.020
	6.907 Hz	0.002	0.010	0.001	0.002	0.965		6.693 Hz	0.003	0.011	0.001	0.002	0.968

## 5. Discussion

The results obtained in Section 4 show that GA-based model updating approaches can be profitably coupled with AVT techniques to simulate the realistic behaviour of masonry structures despite the limited information available about the internal morphology of structural elements and the unknown mechanical properties of constituent materials. Although from a theoretical standpoint, due to the heuristic nature of the method, it is impossible to ensure that all the local minima – from which the global minimum is recovered – are found during the updating process, the method has been proved effective, robust, and less computationally demanding than conventional global sensitivity analyses. The adopted optimization process also corroborated the hypothesis of using an isotropic model to realistically describe the behaviour of large-scale masonry structures, which is quite a common simplification in the literature [17,26]. This was possible thanks to one of the main innovative aspects of this work, namely the exploitation of an automatic procedure capable of handling a very large number of unknowns, which enabled to consider as variables all the meaningful parameters describing the orthotropic behaviour of the masonry material and to compare the goodness of the simulated modal response against the one obtained from the isotropic model. Overall, although the orthotropic approach produced slightly better results in terms of final modal residuals, the improvement was not as marked as it could be expected. Due to the complexity of orthotropic modelling when dealing with unconventional historical structures in both linear and non-linear fields, resorting to the isotropic assumption can allow to greatly reduce the computational effort inherent to the calibration process and subsequent analyses, without compromising the accuracy and reliability of the results. Finally, it is

worth stressing that, unlike most of current FE model updating techniques, the method herein proposed does not run into difficulties when tackling a great number of parameters and has been demonstrated feasible even when the number of subproblems to solve grows exponentially, confirming its suitability to be employed as preferred tool to optimize the control of the structural integrity at global and local level.

## **6. Conclusions**

The paper discussed the combination of vibration-based identification methods and automated modal updating techniques relying on GAs for reproducing the dynamic behaviour of an iconic masonry tower located in Central Italy, i.e. the Ostra Civic Tower.

After a preliminary geometrical and material survey aimed at identifying the main characteristics of the structure necessary for the creation of a reliable numerical model to be later exploited as reference configuration for more sophisticated linear and non-linear analyses, two field testing campaigns were carried out to acquire the vibration response of the tower to ambient noise under operational conditions. These data, after pre-processing operations, were analysed using two modal estimators in order to extrapolate the dynamic parameters related to the principal modes of the structure, allowing to build a target experimental model for the calibration of the numerical tower. Such a calibration process consisted in a perturbation of the mass and stiffness matrices of the system in order to find physically meaningful values for the unknown material properties that could minimize the deviation between the eigenvalues and eigenvectors provided by the OMA. The approach was done through an automatic model updating with genetic algorithm of the OMA eigen-data projected onto the equivalent numerical model. By profiting of a biologically inspired algorithm, the optimization problem was solved by adopting two modelling assumptions for masonry, namely an isotropic and an orthotropic constitutive behaviour, where the latter led to a threefold increase in the number of candidate solutions. The low percentage errors recorded in the eigenvalue comparison for both cases, despite the significant number of updating parameters, demonstrated the efficiency of metaheuristics as compared to time-consuming manual procedures or to other automatic approaches unable to solve global multi-dimensional optimization problems.

Further studies and investigations are to be made to attain a thorough knowledge of this artefact, also considering the soil-structure interaction to evaluate the effects that the unconventional boundary conditions of the Ostra tower have in terms of global structural performance against dynamic actions. Once a full comprehension of the structural behaviour will be reached, surrogate models concerning the tower dynamic properties can be generated to provide a quick tool for examining in nearly real-time the health state of the tower.



## APPENDIX A - Evaluation of the influence of material parameters in automatic calibration

This appendix details in the first part the workflow of the Genetic Algorithm (GA) model updating procedure employed in the present work along with the construction and validation of the relevant metamodel, and reports in the second part all the results from the sensitivity analyses carried out to evaluate the influence of different unknown parameters on the structure's natural frequencies, namely their impact on the outcome of the modal-based updating process. What emerged from the analyses, particularly when comparing the results with those obtained from a second automatic GA-based calibration using the NM18 as initial baseline model, is summarized below:

- Considering all the unknown parameters in the updating procedure leads to final values of material properties consistent with those obtained by performing the model updating only with a reduced number of parameters;
- The frequencies and mode shapes residuals resulting from the model updated through GA are smaller in comparison to the residuals estimated by updating only the most sensitive parameters of the model, hence the FE model calibrated via GA is more representative of the real physical structure;
- When considering an orthotropic material behaviour, the computational costs of the GA-based approach are reduced as compared to apparently more manageable sensitivity analyses, being unnecessary to create a new metamodel and to assess again the most influential parameters.

### A.1. Genetic algorithm workflow

The steps followed by the genetic algorithm are described below:

#### a) Initialization:

Once the parameter ranges and initial values are defined, a population is randomly generated, and all individuals are initialized for the adjustment. The size of the population is given by the value of the parameter NB\_PARENTS and is imposed by the user in the command file. This value is dependent on several factors such as the uncertainty of the solution. The greater the uncertainty, the larger the population. The stabilized value for the study was set to 10.

#### b) Functional Evaluation:

In the first stage only one evaluation is made because the populations are identical, then in the recalibration loop, as many evaluations of the functional are made during this one iteration as the number of children defined by the parameter NB\_FILLS, which is in turn defined by the user. The larger the parameter that defines the renewal of the population, the more CPU time is required for the step by the algorithm. For the present case, 6 parameters, corresponding to half the size of the population, were defined.

#### c) Stopping Criteria:

Once the population of  $n$  parents is defined along with the individuals, the value of the criteria set to stop the calibration process is automatically checked and the best individual of the renewed population is returned as the solution. The check is performed over two variables:

- The best value of the functional calculation;
- The number of iterations already performed by the algorithm.

The former implies that the algorithm stops when the residual tolerance of two consecutive steps reaches the value defined by the user, which in the current case was set equal to  $1e^{-4}$ ; the latter means that the algorithm stops when the maximum number of iterations specified by the user is attained. In the present application, an increasing number of iterations was set for the algorithm, starting with 100 and then moving to 200, 500 and finally 2000.

#### d) Selection – Crossover – Mutation:

The best individual parent is drawn from the population according to a Tournament selection method [73]. In order to combine the genetic information of two parents and generate new offspring, a uniform crossover operator [74–78] is employed, meaning that information is taken from either parent with equal probability. The mutation operator [73,79] also follows a uniform scheme, in which the values of selected genes are replaced by uniform random values falling within the user-defined upper and lower bounds. All the operations are controlled by the value of the parameter ECART\_TYPE (standard deviation) defined as:

$$\sigma = \sqrt{\frac{\sum_{i=1}^N (x_i - \mu)^2}{N}} \quad (\text{A1.1})$$

where  $x_i$  is the  $i^{\text{th}}$  value from the population,  $\mu$  is the population mean, and the denominator  $N$  stands for the population size. For the present study, the value of the parameter ECART\_TYPE was defined as 0.5.

**e) Replacement:**

Once the  $m$  children are generated, the global population of the iteration stage results equal to  $n + m$  (i.e. NB\_PARENTS + NB\_FILLS). In the current implementation, this value was set as 15. The operator that controls the replacement realizes a hierarchy of the individuals according to the values associated by the calculus and replaces the population with the best parents found among the global population.

## A.2. Metamodel

In the model updating field, it is common practice to reduce the computational strain by building metamodels. Metamodels, also referred as “surrogate models”, are a sort of “low computational weight” models of physical systems, in which specifically set model inputs are related to determined model outputs [80–82]. If a model  $F$  is considered, whose behaviour can be described by a vector  $x = (x_1, x_2, x_3 \dots x_n) \in R$ , then the relation of the vector  $x$  and the associated output of the response quantities is given by the function:

$$Y = F(x) \quad (\text{A.2.1})$$

where:

- $F: R^N \rightarrow R^M$ .

In order to reduce the computational strain and effectively calculate the Sobol Indices, surrogate models were constructed. The procedure took place considering as input vectors the material parameters of the isotropic and orthotropic models. The design of experiment utilized was based on a probabilistic approach where all the parameter ranges were defined by normal distributions and the data was then selected for the design of experiments by a Monte-Carlo algorithm. The whole process was carried out in the Openturns environment [83]. The output, that was thoroughly calculated considering not only the eigenvalues of the physical system, but also the MAC values between the experimental and numerical models, was used to create the metamodel with a Kriging approach.

The Kriging metamodel [35,84–88] has its origins in Geostatistics [89] and it is a common technique for the interpolation of spatial data. The whole process aims at creating a predictor that can be denoted as  $\check{G}$  and is assumed as a realization of the normal process  $Y: \Omega \times R^d \rightarrow R$ , defined by:

$$Y(\omega, x) = f(x) + F(\omega, x) \quad (\text{A.2.2})$$

where:

- $f(x)$  defines the trend;

- $F(x, \omega)$  is a zero-mean Gaussian process with a covariance function  $C: R^d \times R^d \mapsto R$  dependent on the vector of parameters  $x \in R$ , for some given event  $\omega \in \Omega$ :

$$E[F(x), F(y)] = C_\theta(x, y). \quad (\text{A.2.3})$$

The trend is taken equal to the generalized linear model:

$$f(x) = f(x)^t \beta \quad (\text{A.2.4})$$

The method approximates the model F by the means of the Y given that:

$$Y(\omega, x^{(i)}) = y^{(i)}, \quad \forall i = 1, \dots, n \quad (\text{A.2.5})$$

It follows that the metamodel can be written as:

$$\check{G} = E[Y(\omega, x) | Y(\omega, x^{(i)}) = y^{(i)}, \quad \forall i = 1, \dots, n] \quad (\text{A.2.6})$$

and defined as:

$$\check{G} = (f(x))^t \check{\beta} + (C_\theta(x))^t C_\theta^{-1} (y - F \check{\beta}) \quad (\text{A.2.7})$$

with  $\check{\beta}$  being the least squares estimator for  $\beta$  :

$$\check{\beta} = (F^t C_\theta^{-1} F)^{-1} F^t C_\theta^{-1} y \quad (\text{A.2.8})$$

Having the functions defined, the Kriging predictor is constructed by selection of  $\beta$  parameters and  $\theta$  correlation parameters. Given the high coefficient of determination ( $R^2$ ) obtained from different stages of validation (see sub-Section A.2.2), this model was ultimately employed as reference for the calculation of the Sobol Indices.

### A.2.1. Parameters definition

Normal probability distribution was the base for defining Young's moduli (E) [MPa], Poisson coefficient ( $\nu$ ) [-], and mass density ( $\gamma$ ) [kN/m<sup>3</sup>] in the metamodel. At first, it was decided to consider the whole ranges of parameters allowed by the Italian technical regulations, having distribution values of the Young's moduli from 800 MPa to 5000 MPa for masonry, and from 17000 MPa to 38000 MPa for concrete.

Table A.1 - Initial parameters normal probabilistic distribution.

	Mean	Standard Deviation	Min - Max
Masonry E [MPa]	3000	600	800 - 5000
Concrete E [MPa]	28000	2800	17000 - 30000
Masonry $\nu$ [-]	0.25	0.05	0.05 - 0.45
Concrete $\nu$ [-]	0.25	0.05	0.05 - 0.45
Masonry $\gamma$ [kN/m <sup>3</sup> ]	18	1	13 - 22
Concrete $\gamma$ [kN/m <sup>3</sup> ]	25	1	21 - 26

### A.2.2 Validation

The validation of the metamodel, namely its capability to explain the observed outcome, was done by selecting a three-way approach and assuming as acceptable statistic an  $R^2$  index greater than or equal

to 0.9 for each resulting prediction. For the first check, validation solutions were provided as follows: 1) analytically; 2) dividing the dataset into an 80% – 20% scheme, using the 80% percentage as training (820 samples) and the 20% (204 samples) as validation of the trained model; 3) using a K-Fold procedure.

The results of the analytical validation, for both material approaches, are shown below (Figure A.1÷A.4).

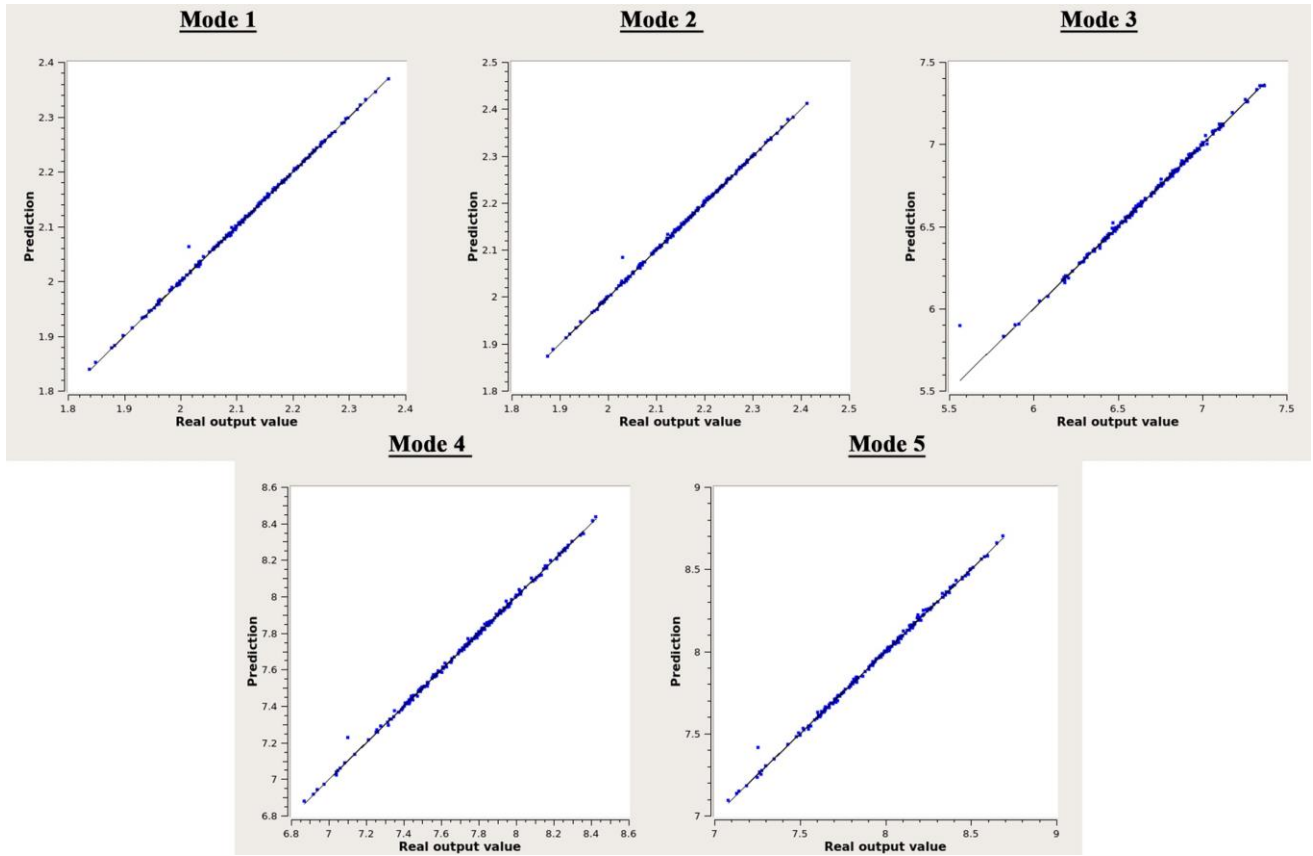


Figure A.1- Analytical model validation for Isotropic model: curve fitting of frequencies test samples.



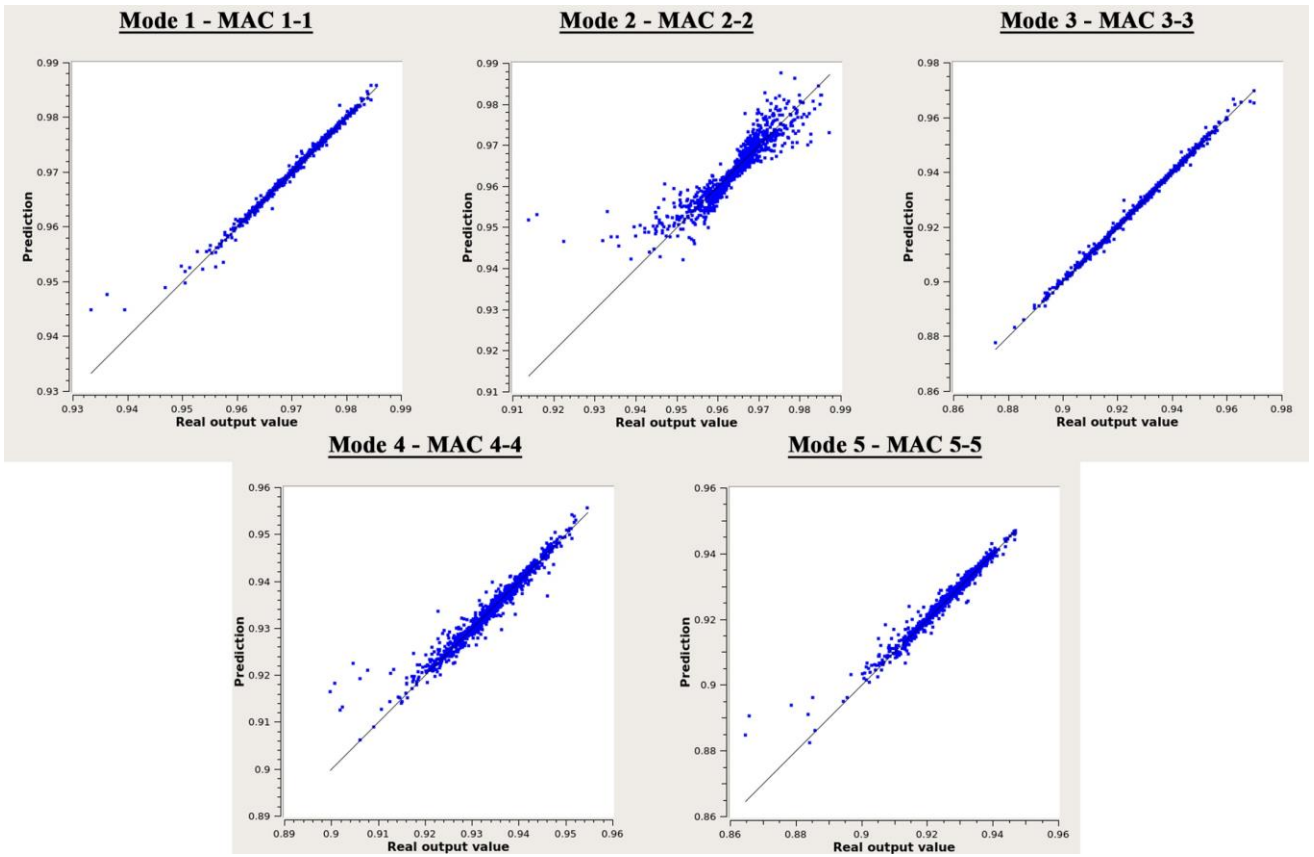


Figure A.2- Analytical model validation for Isotropic model: curve fitting of mode shapes test samples.

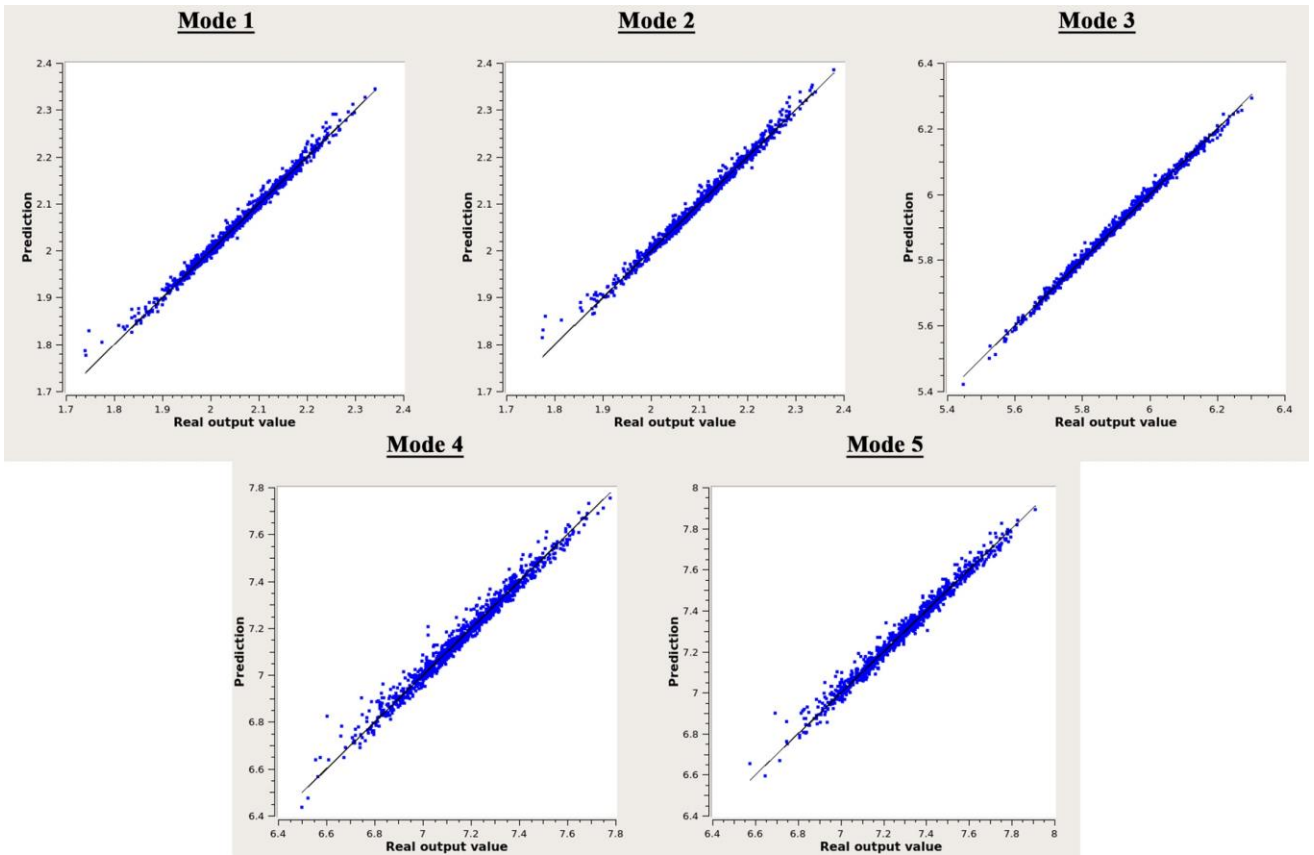


Figure A.3- Analytical model validation for Orthotropic model: curve fitting of frequencies test samples.

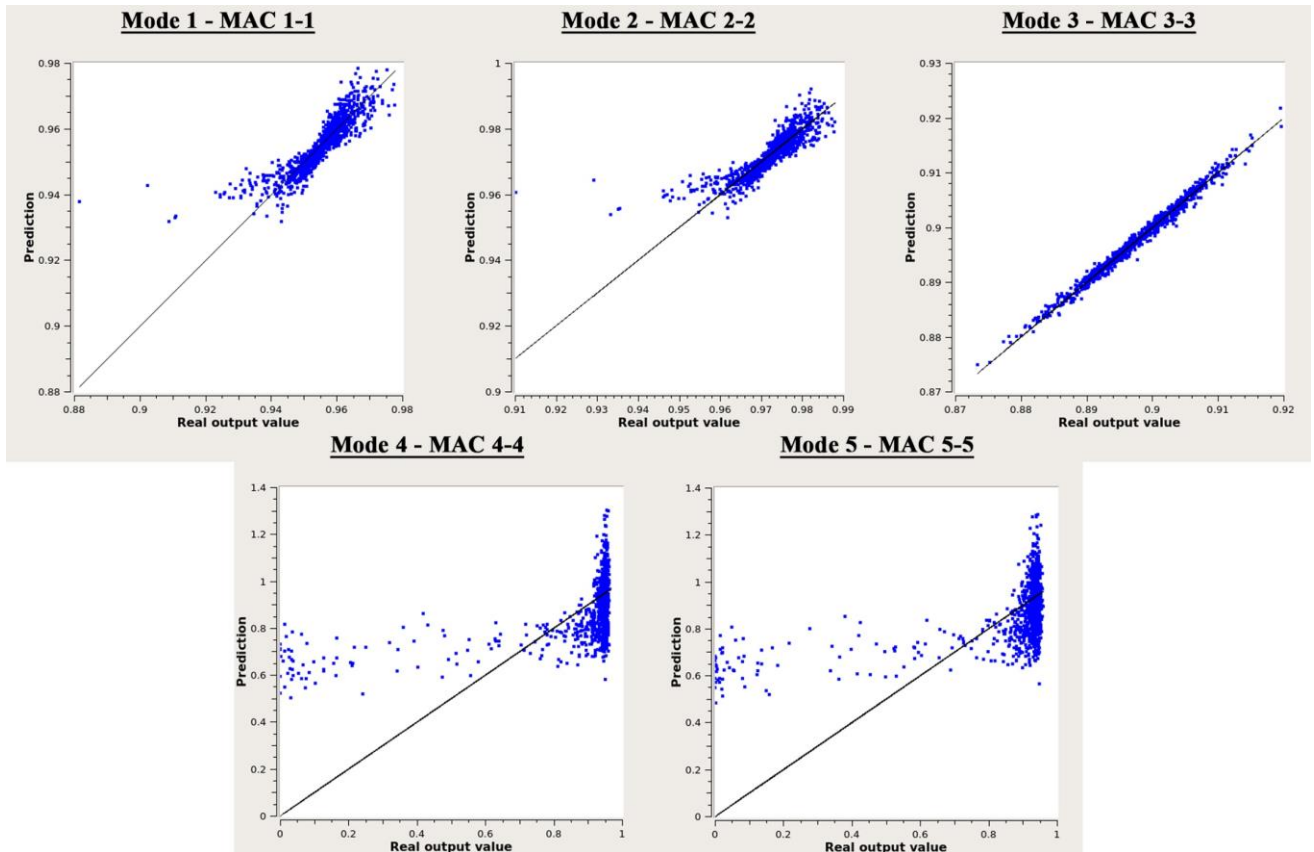


Figure A.4 - Analytical model validation for Orthotropic model: curve fitting of mode shapes test samples.

In Table A.2 and Table A.3 it is possible to observe the values of the coefficient of determination for both frequencies and MAC coefficients. It is noticed how  $R^2$  is practically near to 1 when predicting frequency values either with an isotropic or an orthotropic approach, while it sensibly decreases for the higher order modes when evaluating the mode shapes using an orthotropic model.

Table A.2 - Analytical validation of frequencies.

Mode	Number of points	Percentage training/validation	Isotropic model		Orthotropic model	
			Residual	$R^2$	Residual	$R^2$
1	1024	80 - 20	0.000075	0.999	0.000289	0.990
2	1024	80 - 20	0.000084	0.999	0.000301	0.989
3	1024	80 - 20	0.000464	0.997	0.000298	0.995
4	1024	80 - 20	0.000323	0.999	0.000967	0.978
5	1024	80 - 20	0.000365	0.999	0.000897	0.982

Table A.3 - Analytical validation of mode shapes.

MAC	Number of points	Percentage training/validation	Isotropic model		Orthotropic model	
			Residual	R <sup>2</sup>	Residual	R <sup>2</sup>
1_1	1024	80 - 20	0.000022	0.985	0.000140	0.752
2_2	1024	80 - 20	0.000109	0.814	0.000119	0.723
3_3	1024	80 - 20	0.000024	0.997	0.000024	0.987
4_4	1024	80 - 20	0.000057	0.945	0.005210	0.251
5_5	1024	80 - 20	0.000057	0.963	0.005294	0.246

The second validation scheme was done on the model where the predictor was trained with 80% of the data and the residual 20% was used for the validation test, whose results are presented in the following Figures A.5-A.8.

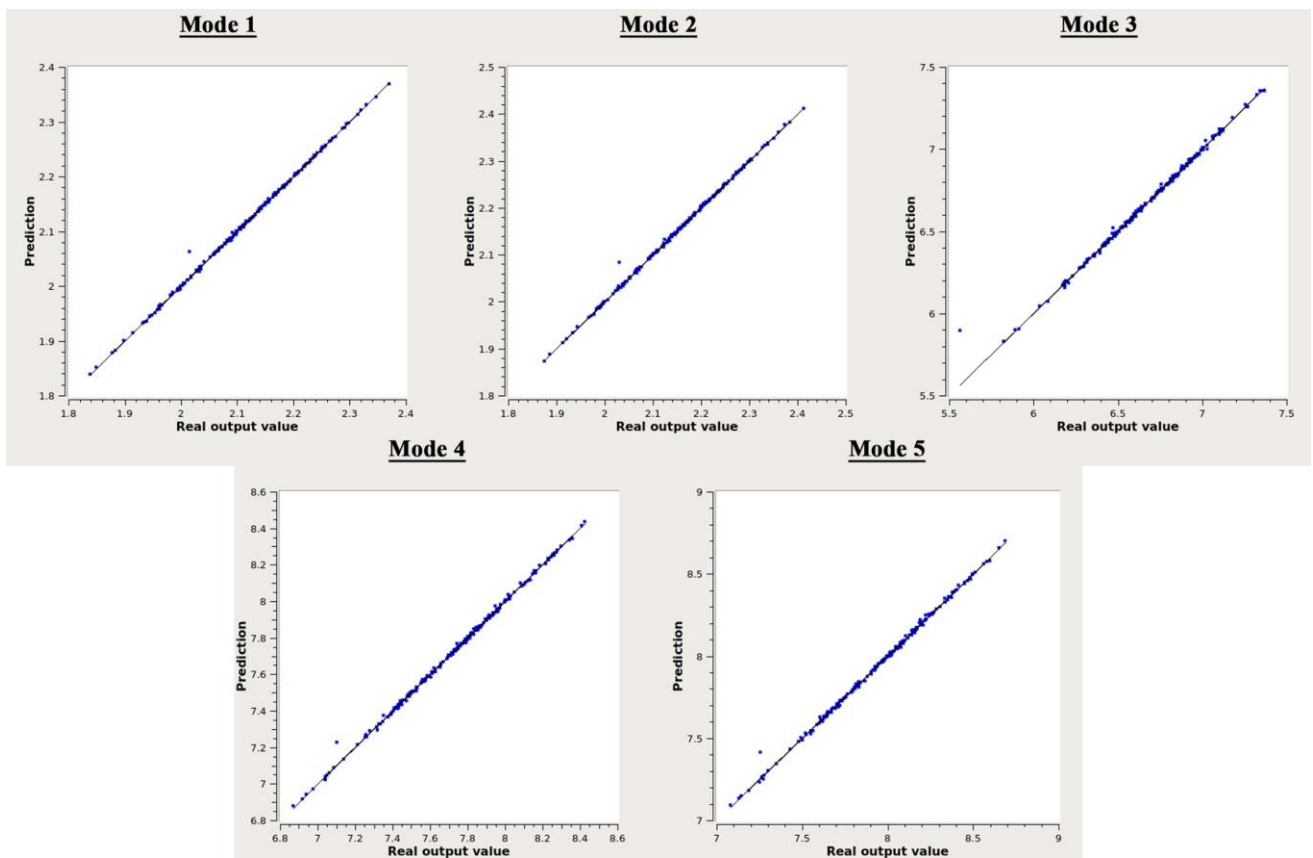


Figure A.5 - Train/Test split validation for Isotropic model: curve fitting of frequencies test samples.

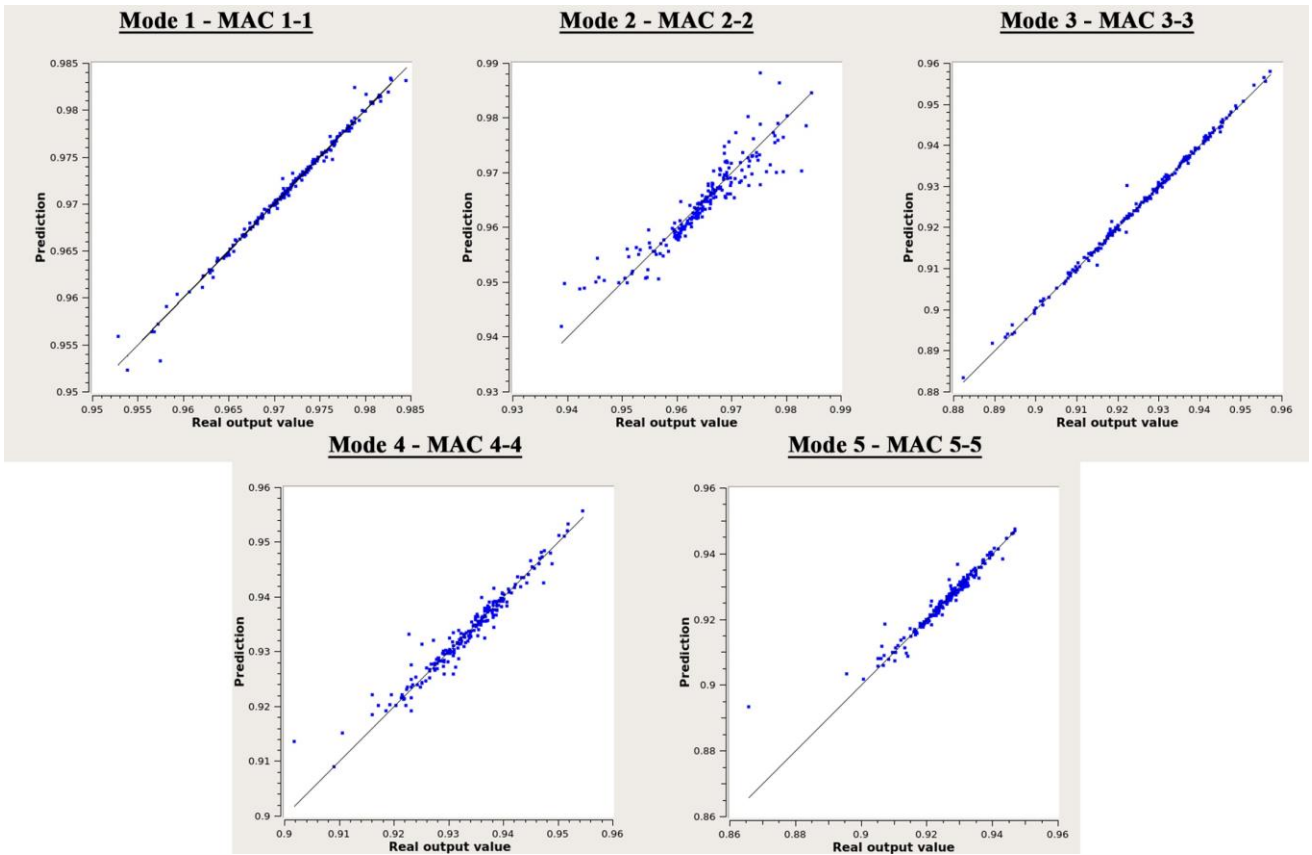


Figure A.6 - Train/Test split validation for Isotropic model: curve fitting of mode shapes test samples.

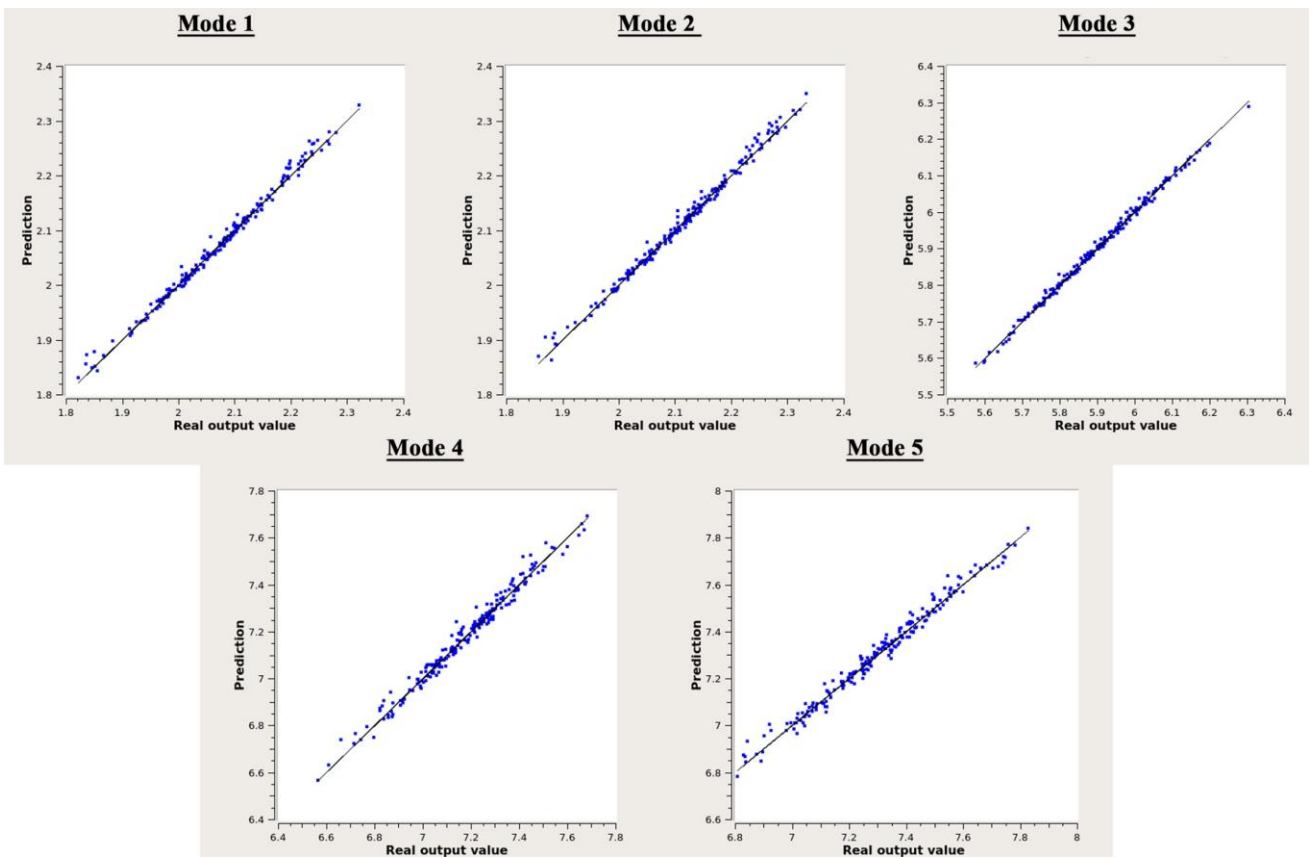


Figure A.7 - Train/Test split validation for Orthotropic model: curve fitting of frequencies test samples.

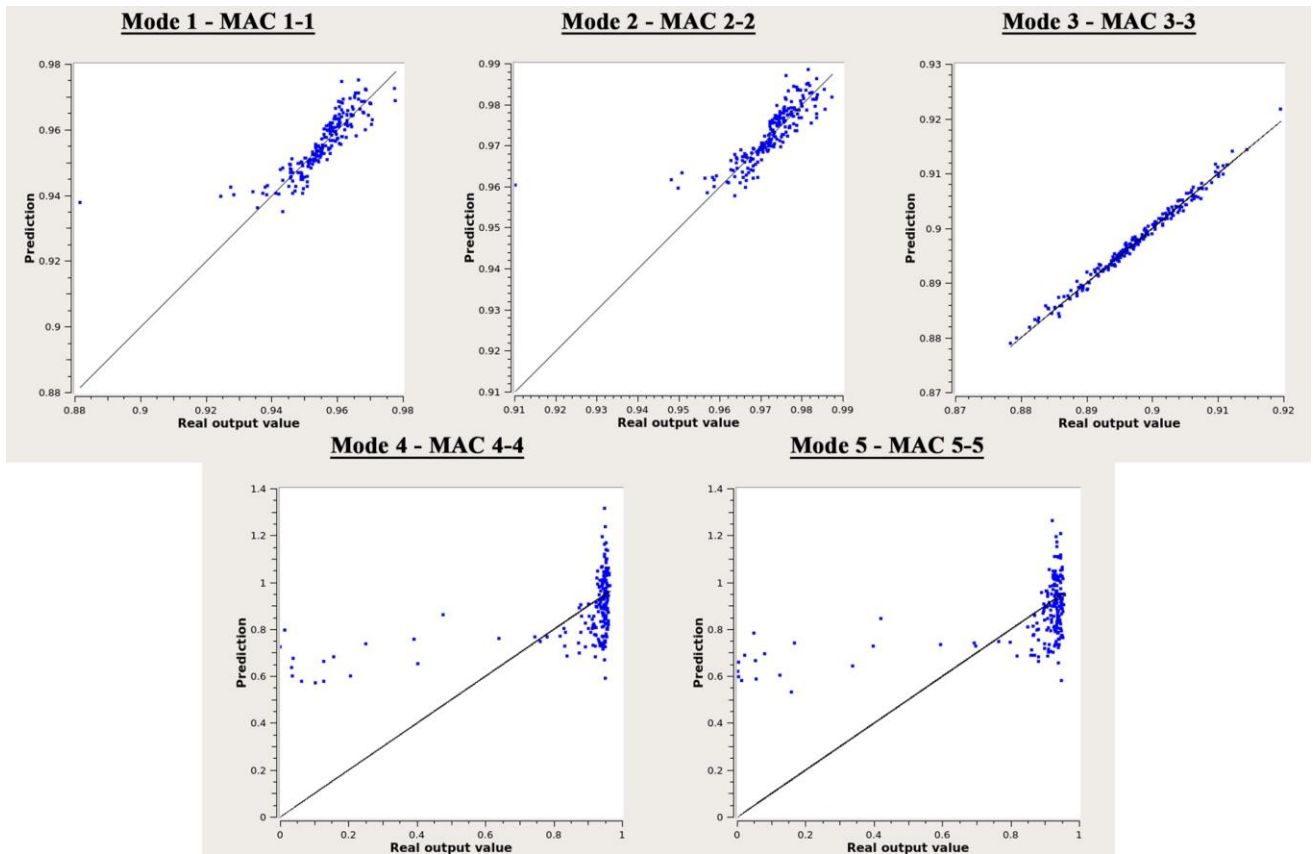


Figure A.8 - Train/Test split validation for Orthotropic model: curve fitting of mode shapes test samples.

Looking at Table A.4 and Table A.5 one can notice that the trend of the analytical validation is maintained and confirmed also by the Train/Test approach.

Table A.4- Train/Test split validation of frequencies.

Mode	Number of points	Percentage	Isotropic model		Orthotropic model	
			Residual	R <sup>2</sup>	Residual	R <sup>2</sup>
1	204	20	0.000266	0.999	0.000639	0.991
2	204	20	0.000301	0.998	0.000668	0.991
3	204	20	0.001779	0.993	0.000606	0.996
4	204	20	0.000863	0.998	0.002086	0.980
5	204	20	0.001026	0.998	0.001967	0.982

Table A.5- Train/Test split validation of mode shapes.

MAC	Number of points	Percentage	Isotropic model		Orthotropic model	
			Residual	R <sup>2</sup>	Residual	R <sup>2</sup>
1_1	204	20	0.000042	0.988	0.000395	0.668
2_2	204	20	0.000213	0.854	0.000337	0.625
3_3	204	20	0.000063	0.996	0.000054	0.988
4_4	204	20	0.000133	0.944	0.012807	0.234
5_5	204	20	0.000182	0.929	0.013189	0.233

Lastly, the K-Fold method was employed using 10 numbers of folds. The K-fold cross validation technique relies on the division of the dataset (called X) into K mutually exclusive sub-samples ( $X_n$  with  $n = 1, 2, \dots, m$ ). A sub-sample is set aside for the response surface to be built on the remaining



sub-samples. The approximation error is then estimated utilizing the sub-sample that was left aside and is defined as:

$$R_i = \frac{1}{|X_i|} \sum_{X \in N} |h(X) - h^N(X_i)|^2 \quad (\text{A.2.9})$$

in which the quantity  $|h(X) - h^N(X_i)|^2$  is the predicted residual, namely the difference between the evaluation and the prediction at point  $X_i$  of the sub-sample. The approximation errors are estimated using each sub-sample as validation, whereas the remaining sub-samples are used for training. At the end of the process, the K-fold cross validation error estimate is obtained as the average:

$$R_{K-Fold} = \frac{1}{K} \sum_{i=1}^K R_i \quad (\text{A.2.10})$$

The results obtained through the K-Fold method confirm the results obtained from the previous validation approaches and are reported from Figure A.9 to Figure A.12 as well as in Table A.6 and Table A.7.

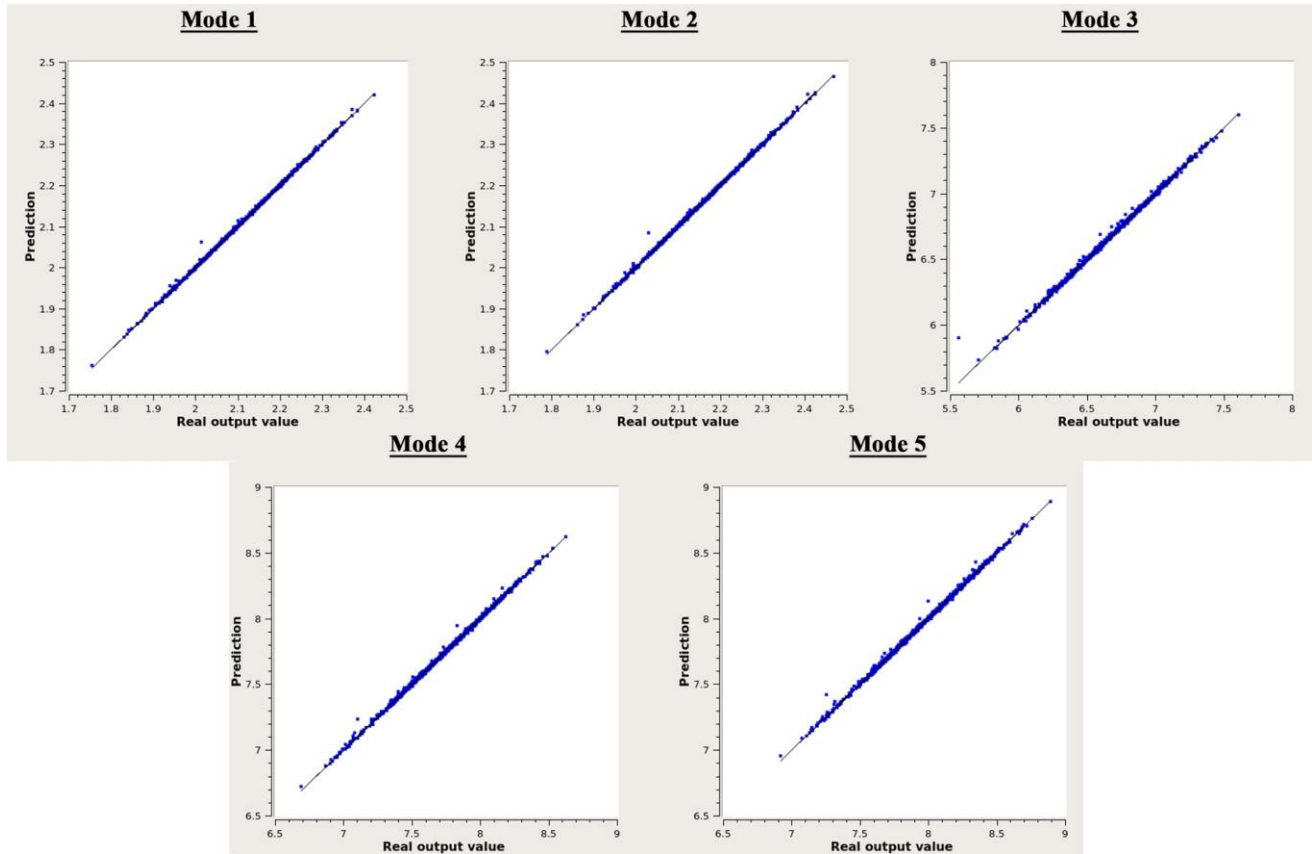


Figure A.9 - K-Fold validation for Isotropic model: curve fitting of frequencies test samples.

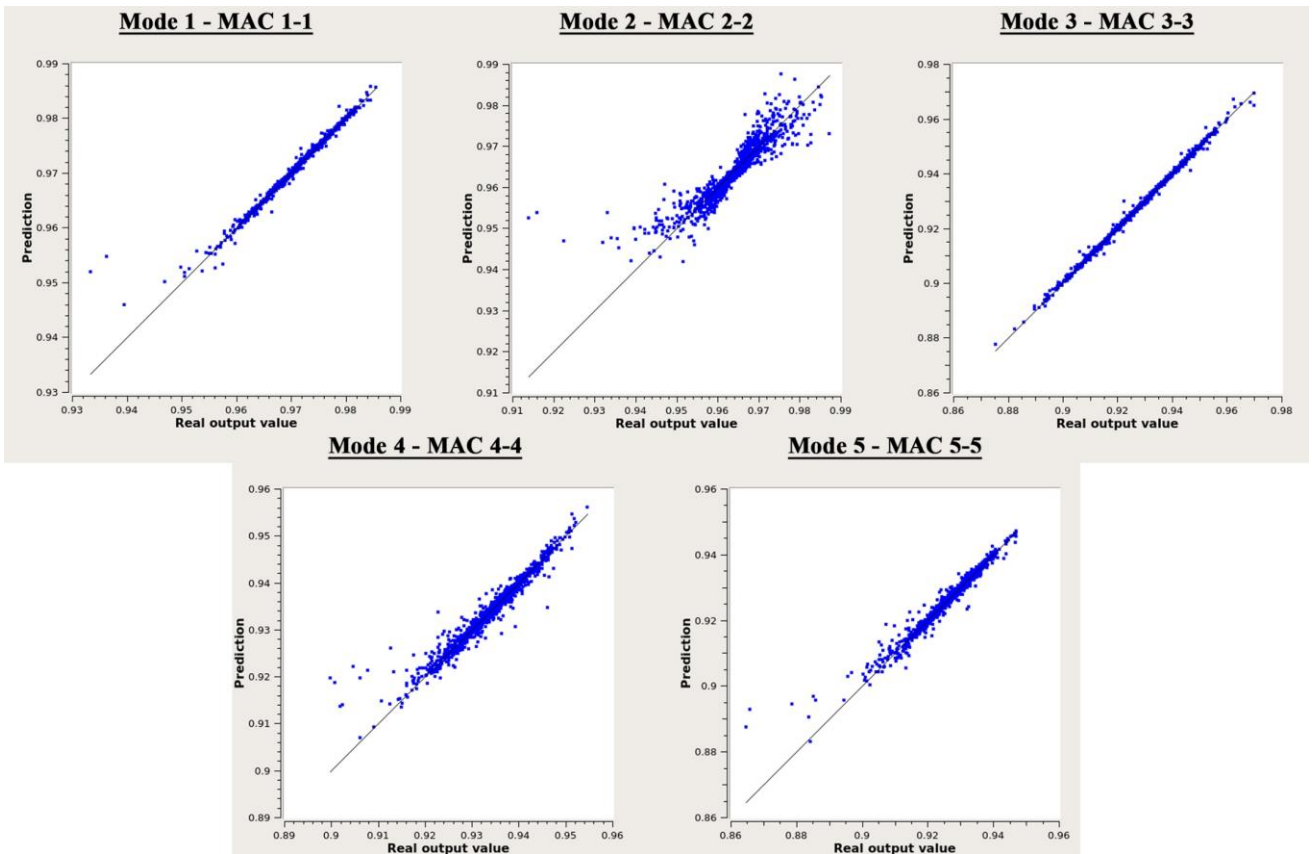


Figure A.10 - K-Fold validation for Isotropic model: curve fitting of mode shapes test samples.

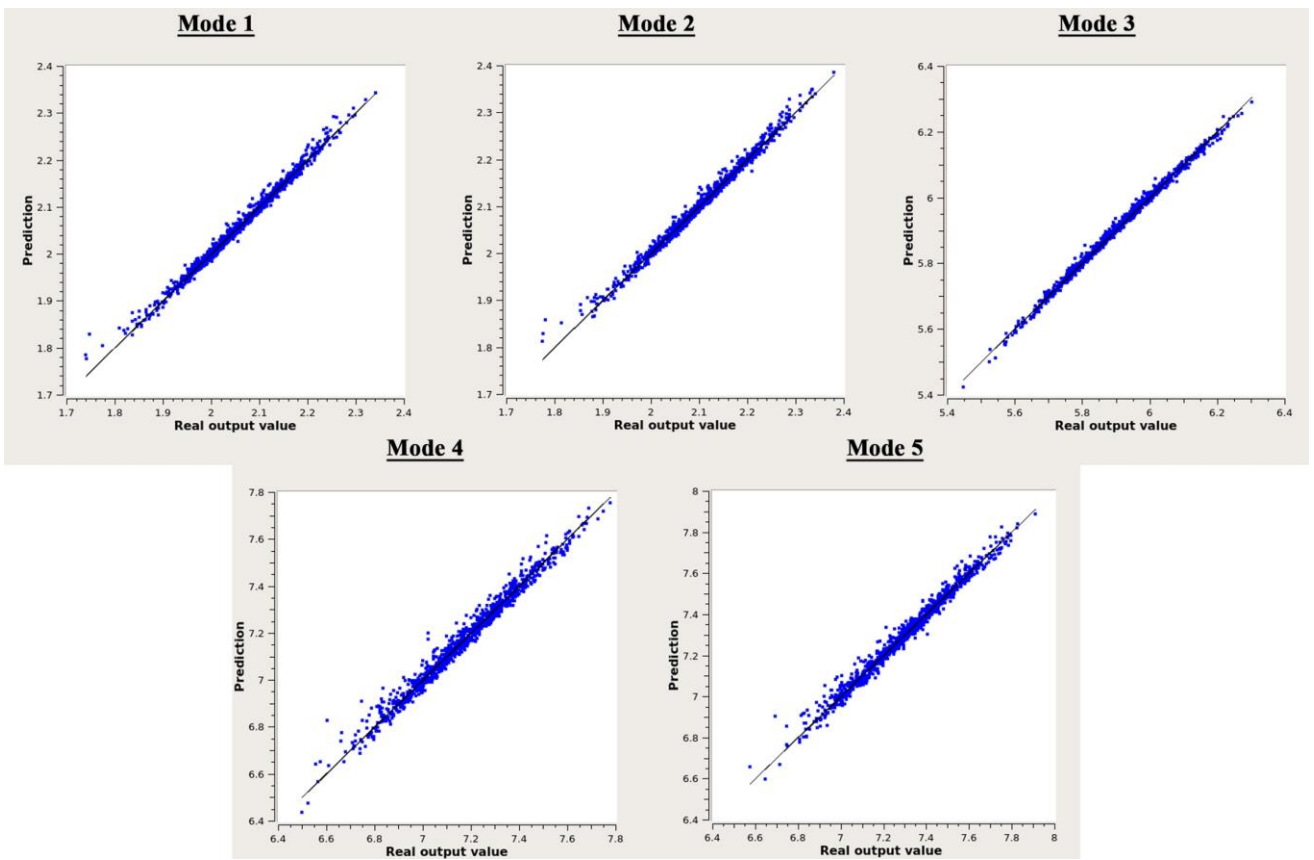


Figure A.11 - K-Fold validation for Orthotropic model: curve fitting of frequencies test samples.

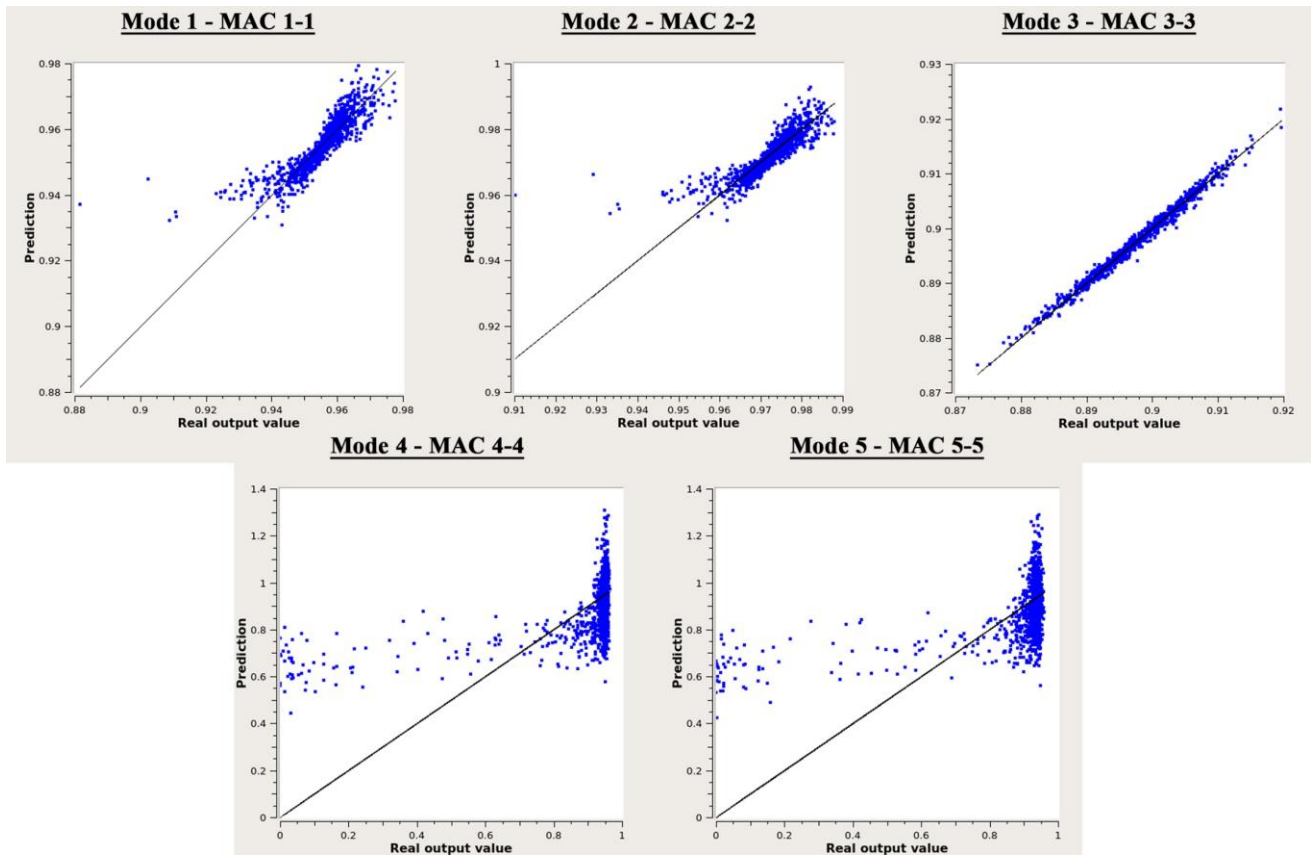


Figure A.12 - K-Fold validation for Orthotropic model: curve fitting of mode shapes test samples.

Table A.6- K-Fold validation of frequencies.

Mode	Number of points	Number of folds	Isotropic Approach		Orthotropic Approach	
			Residual	R <sup>2</sup>	Residual	R <sup>2</sup>
1	1024	10	0.000226	0.999	0.000918	0.989
2	1024	10	0.000255	0.999	0.000956	0.989
3	1024	10	0.001338	0.997	0.000950	0.995
4	1024	10	0.001030	0.999	0.003051	0.977
5	1024	10	0.001142	0.998	0.002865	0.981

Table A.7- K-Fold validation of mode shapes.

MAC	Number of points	Number of folds	Isotropic Approach		Orthotropic Approach	
			Residual	R <sup>2</sup>	Residual	R <sup>2</sup>
1_1	1024	10	0.000072	0.979	0.000438	0.747
2_2	1024	10	0.000334	0.821	0.000372	0.720
3_3	1024	10	0.000079	0.997	0.000077	0.987
4_4	1024	10	0.000190	0.939	0.016444	0.231
5_5	1024	10	0.000187	0.958	0.016704	0.225

### A.3. Sensitivity analyses for isotropic material approach

Sensitivity analyses based on the Sobol Index (SI) calculation were conducted in order to evaluate the influence of isotropic material parameters in the outcome of the model updating process for NM19, starting from the model of 2018 (NM18) already calibrated through the GA procedure.

SI was calculated as:

$$SI_{ik} = \left| \frac{X_k}{Y_i} \cdot \frac{\Delta Y_i}{\Delta X_k} \right| \cdot 100 \quad (\text{A.3.1})$$

where:

- $X_k$  is the  $k$ -th uncertain parameter;
- $Y_i$  is the  $i$ -th predicted parameter;
- $\Delta$  the variation produced in the relevant parameter.

SIs were calculated both in relation to the output variation produced by changing every single parameter by 100% (indicated as “First Order Index”) and in relation to the output variation produced in correlation with other updating parameters changes (“Total Order Index”), as shown in Figure A.13 and Figure A.14. Moreover, to better track the influence of the number of updating parameters in the calibration process outcome, simulations were run considering different SI thresholds (1%, 5% and 10%). It is found that the highest changes in the modal frequencies produced by a first order index are mainly associated to the materials Young’s modulus of basement inner walls and central body as far as the first two vibration modes are concerned, whereas higher order bending modes result sensitive to both the variations of Poisson’s coefficient and mass density in the different parts. Moving to a total order index, the range of parameters influencing the natural frequencies of the different modes reduces to the Young’s modulus of the materials composing the basement and the central body of the tower. Yet, this reduction comes at a very high computational cost which strongly undermines the efficiency of the updating process and that could be easily bypassed resorting to the proposed GA-based approach.

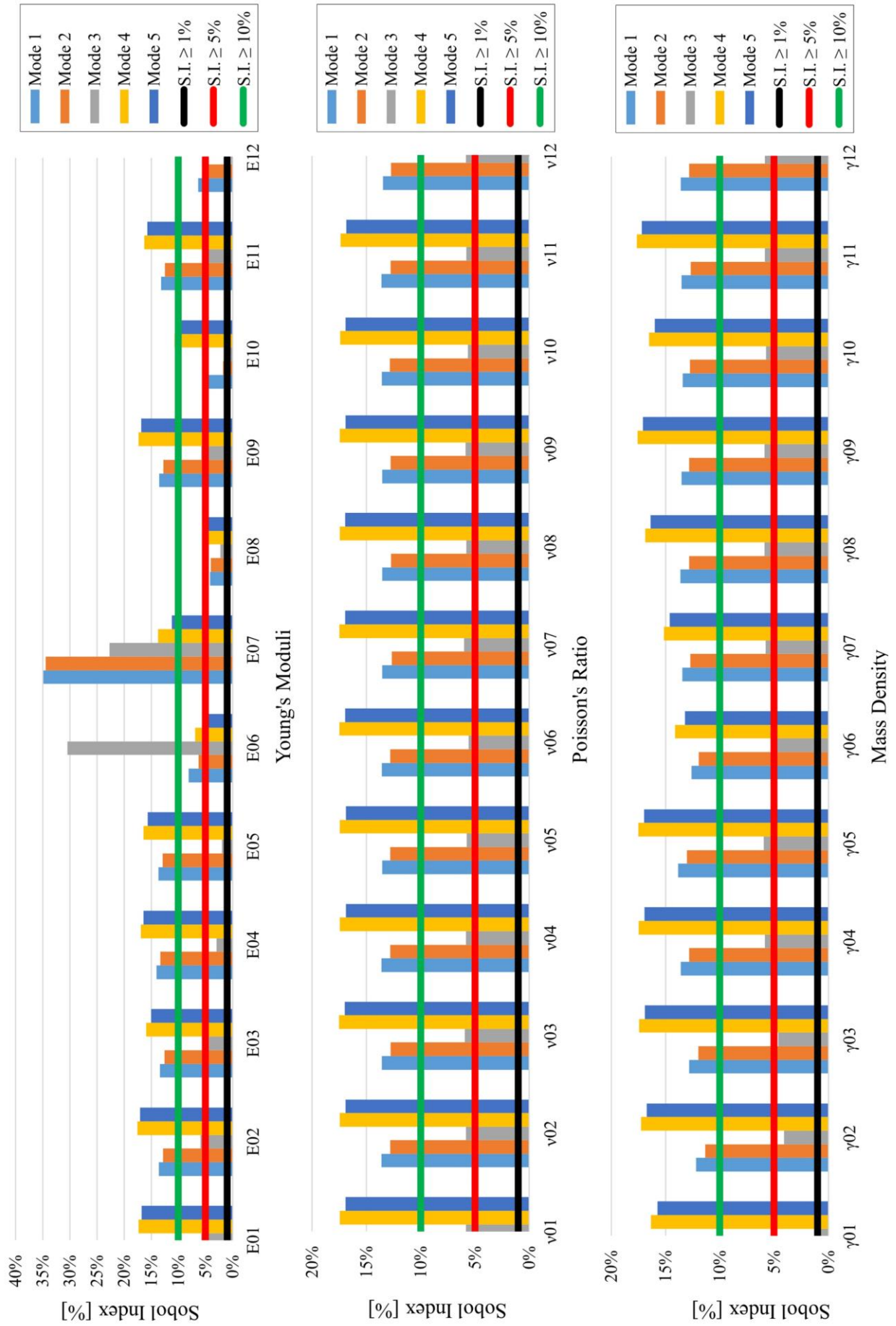


Figure A.13- Sobol sensitivity analysis over first order indices for Kriging method. Thresholds of Sobol Indices (SI) respectively highlighted in black (SI = ±1%), red (SI = ±5%) and green (SI = ±10%).



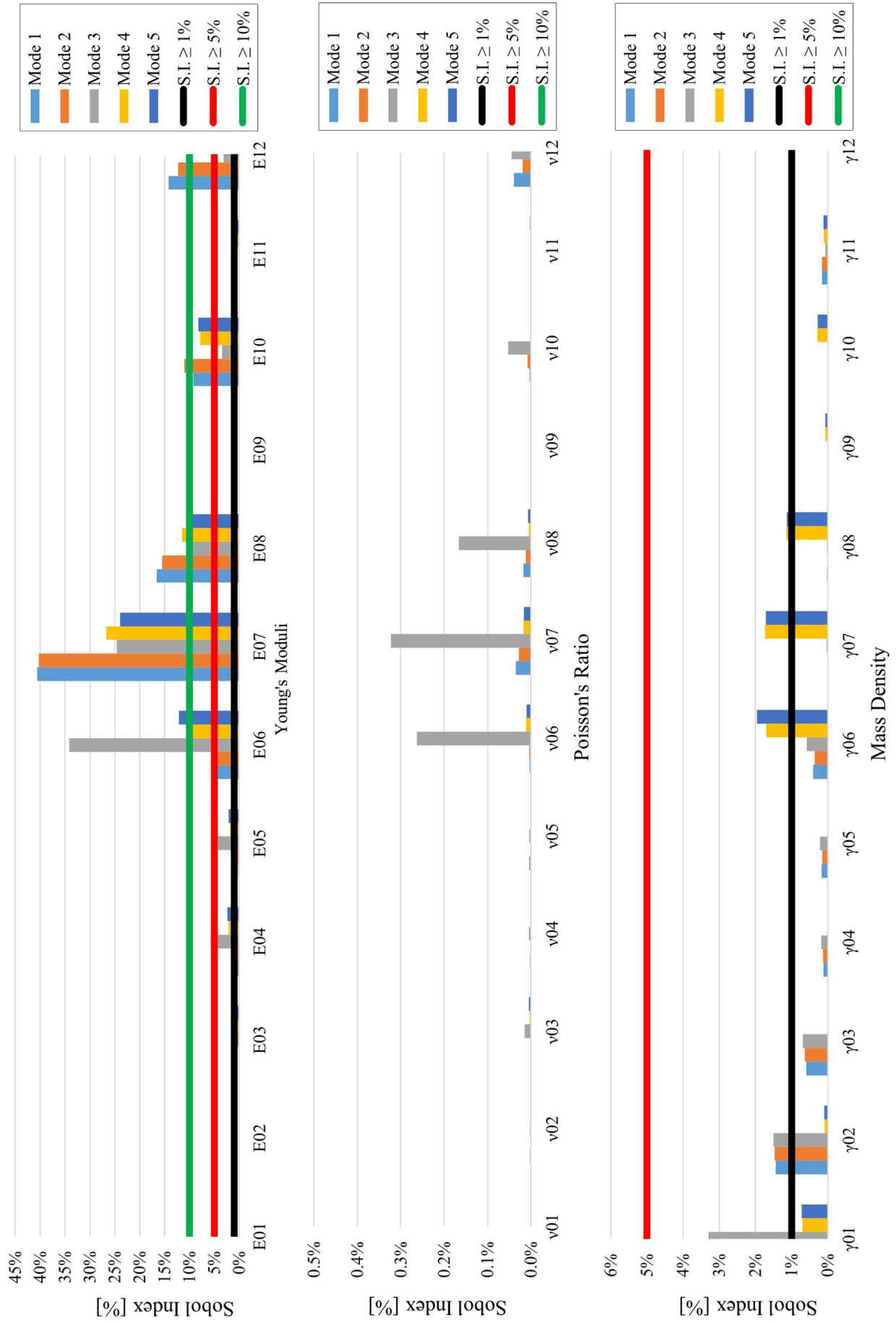


Figure A.14- Sobol sensitivity analysis over total order indices for Kriging method. Thresholds of Sobol Indices (SI) respectively highlighted in black (SI = 1%), green (SI = 5%) and red (SI = 10%).

In light of the results obtained considering Total Order Sobol sensitivity analysis the following parameters were considered for calibration of NM19 with orthotropic material approach (Table A.8).

*Table A.8 - Material parameters considered for calibration of NM19 after Sobol sensitivity analysis, using isotropic approach.*

	<b>Isotropic material parameters</b>	<b>Total</b>
<b>S.I. <math>\geq</math> 1%</b>	E <sub>03</sub> - E <sub>04</sub> - E <sub>05</sub> - E <sub>06</sub> - E <sub>07</sub> - E <sub>08</sub> - E <sub>10</sub> - E <sub>12</sub> $\gamma_{01}$ - $\gamma_{02}$ - $\gamma_{06}$ - $\gamma_{07}$ - $\gamma_{08}$	13
<b>S.I. <math>\geq</math> 5%</b>	E <sub>04</sub> - E <sub>06</sub> - E <sub>07</sub> - E <sub>08</sub> - E <sub>10</sub> - E <sub>12</sub>	6
<b>S.I. <math>\geq</math> 10%</b>	E <sub>06</sub> - E <sub>07</sub> - E <sub>08</sub> - E <sub>10</sub> - E <sub>12</sub>	5

Afterwards, the results from the calibration process of NM19, updated from the baseline numerical model of 2018, were compared first against the ones obtained from the optimized NM18, and then against those achieved with NM19\_0, i.e. a model built from scratch and calibrated directly via GA using the experimental results of 2019 and considering all the parameters as updating variables (Figure A.15). Except for a few cases, the variation of NM19 materials Young's moduli with respect to NM18 and NM19\_0 counterparts shows a better agreement with the first model, proving that updating with new information a refined baseline model previously calibrated with reference data not only is faster and less demanding from a computational point of view, but also less prone to statistical variations from random error sources.

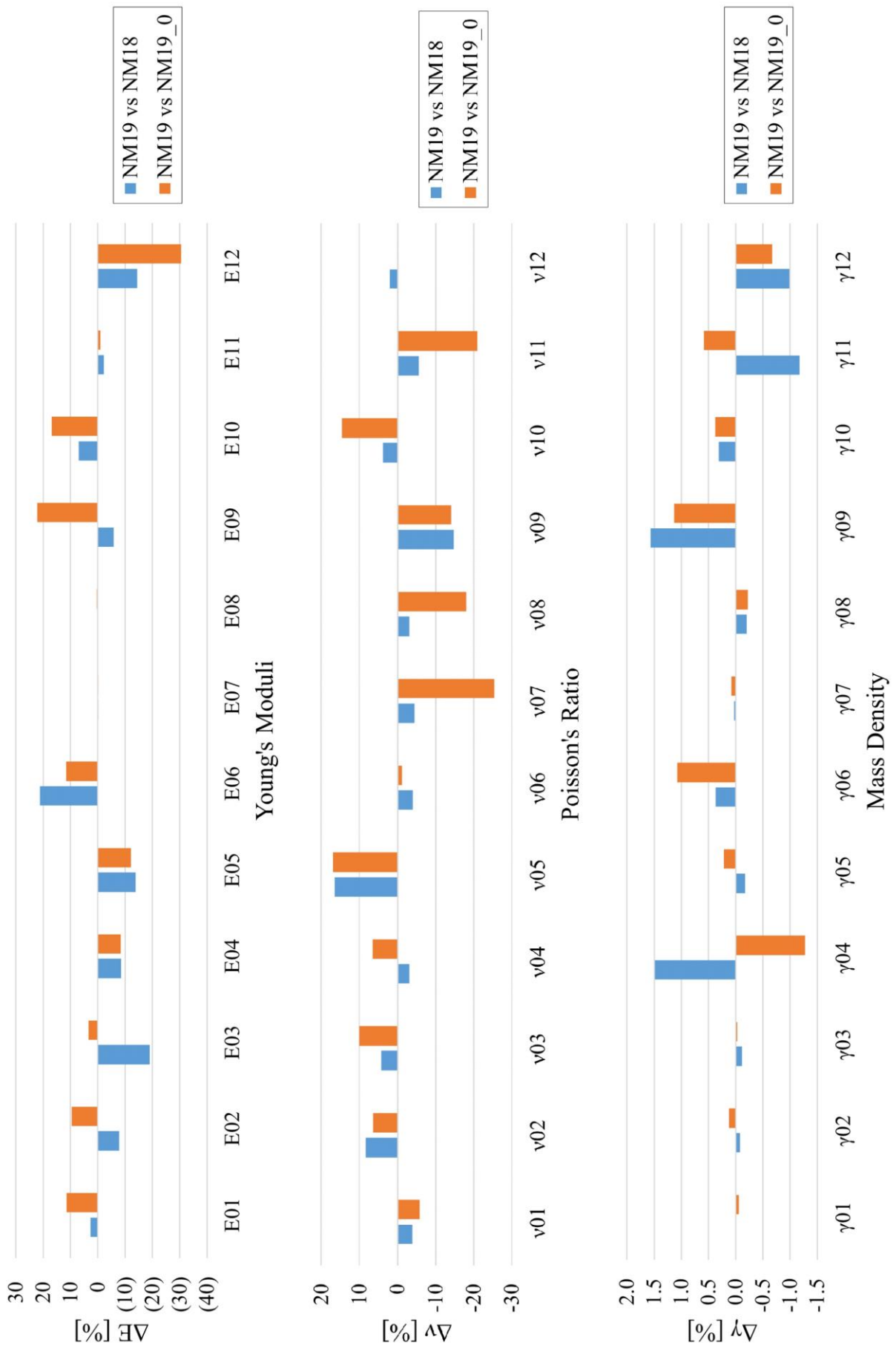


Figure A.15 - Variation of NM19 material parameters in comparison to NM18 (in blue) and NM19\_0 (in orange), considering all parameters in the calibration process.



Figure A.16 - Variation of NM19 material parameters with respect to NM18 considering a reduced number of variables based on different thresholds of SI.

Figure A.16 compares the percentage variation of the Young's moduli, Poisson's coefficients and mass density of NM19 materials with respect to those of NM18 considering a number of parameters reduced on the basis of the sensitivity analyses previously described and for different thresholds of SI. The comparison shows levels of variation similar or marginally better than those obtained by considering all the material parameters in the calibration. Nevertheless, the improvement is very little to justify the excessive computation time of a global sensitivity analysis. Furthermore, looking at the frequency relative errors, it is observed that the natural frequencies of the first five modes featured by the updated model of the tower (NM19) show very low variations ( $\Delta f < 0.8\%$ ) regardless of the number of parameters considered in the calibration process (Table A.9).

Table A.9 - Variation of calibrated frequencies of NM19 in relation to the number of parameters subdued to updating process.

Mode	All Parameters					S.I. = 1%		S.I. = 5%		S.I. = 10%	
	$f_{NM18}$ [Hz]	$f_{NM19_0}$ [Hz]	$f_{NM19}$ [Hz]	$ \Delta f_{NM18} $ [%]	$ \Delta f_{NM19_0} $ [%]	$f_{NM19}$ [Hz]	$ \Delta f_{NM18} $ [%]	$f_{NM19}$ [Hz]	$ \Delta f_{NM18} $ [%]	$f_{NM19}$ [Hz]	$ \Delta f_{NM18} $ [%]
$\varphi_1$	2.070	2.078	2.079	0.43	0.05	2.076	0.29	2.062	0.39	2.064	0.29
$\varphi_2$	2.111	2.121	2.123	0.57	0.09	2.121	0.47	2.109	0.09	2.110	0.05
$\varphi_3$	6.245	6.279	6.277	0.51	0.03	6.283	0.60	6.342	1.53	6.338	1.47
$\varphi_4$	6.693	6.693	6.645	0.72	0.72	6.647	0.69	6.671	0.33	6.674	0.28
$\varphi_5$	6.839	6.843	6.789	0.74	0.80	6.793	0.68	6.824	0.22	6.826	0.19

#### A.4. Sensitivity analyses for orthotropic material approach

Sensitivity analyses for orthotropic material approach were carried out with the same methodology applied for the isotropic model. The first order influence of the different material parameters on the global behaviour of the orthotropic model NM19, built again using NM18 as starting model, is shown in Figure A.17. The results for the total order index are reported in Figure A.18.

It is immediately observable how in the orthotropic model, even considering different thresholds of the SI, other parameters, such as mass density, give non negligible contributions to the model updating in comparison to the isotropic model, for which the most burdensome parameters resulted to be the Young's moduli. Overall, it is found again that the highest changes in the modal frequencies produced by a first order index are essentially associated to the materials Young's modulus of basement inner walls and central body as far as the first two vibration modes are concerned, whereas the torsion mode is particularly sensitive also to the variations of shear modulus, Poisson's coefficient and mass density of the different parts. Considering a total order index, the range of parameters influencing the natural frequencies of the different modes sensibly reduces, but as previously referred, such a reduction comes at a very high computational cost which is not required by the proposed GA-based model updating procedure.



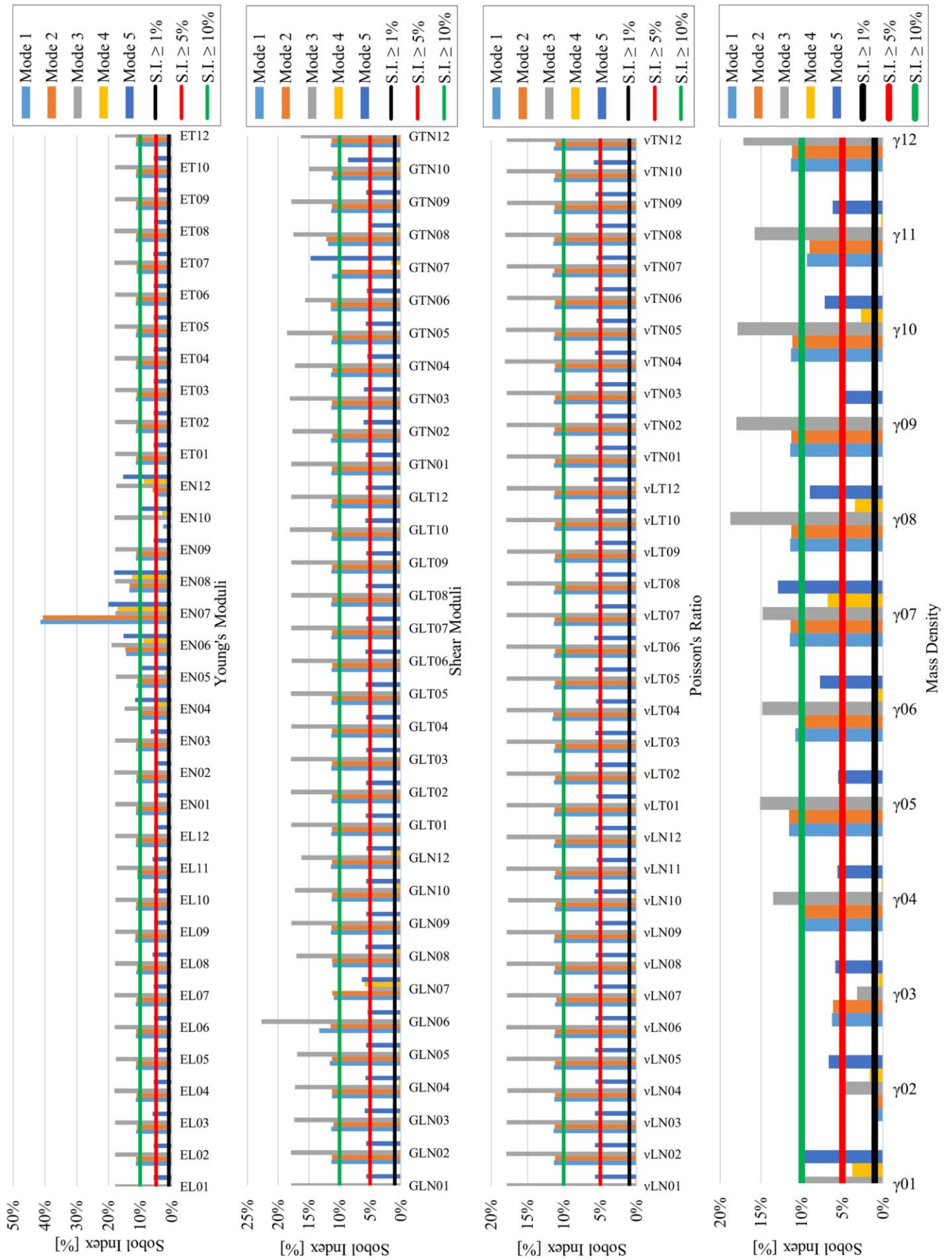


Figure A.17 - Sobol sensitivity analysis over first order indices for Kriging method. Thresholds of Sobol Indices (SI) respectively highlighted in black (SI =  $\pm$ 1%), green (SI =  $\pm$ 5%) and red (SI =  $\pm$ 10%).

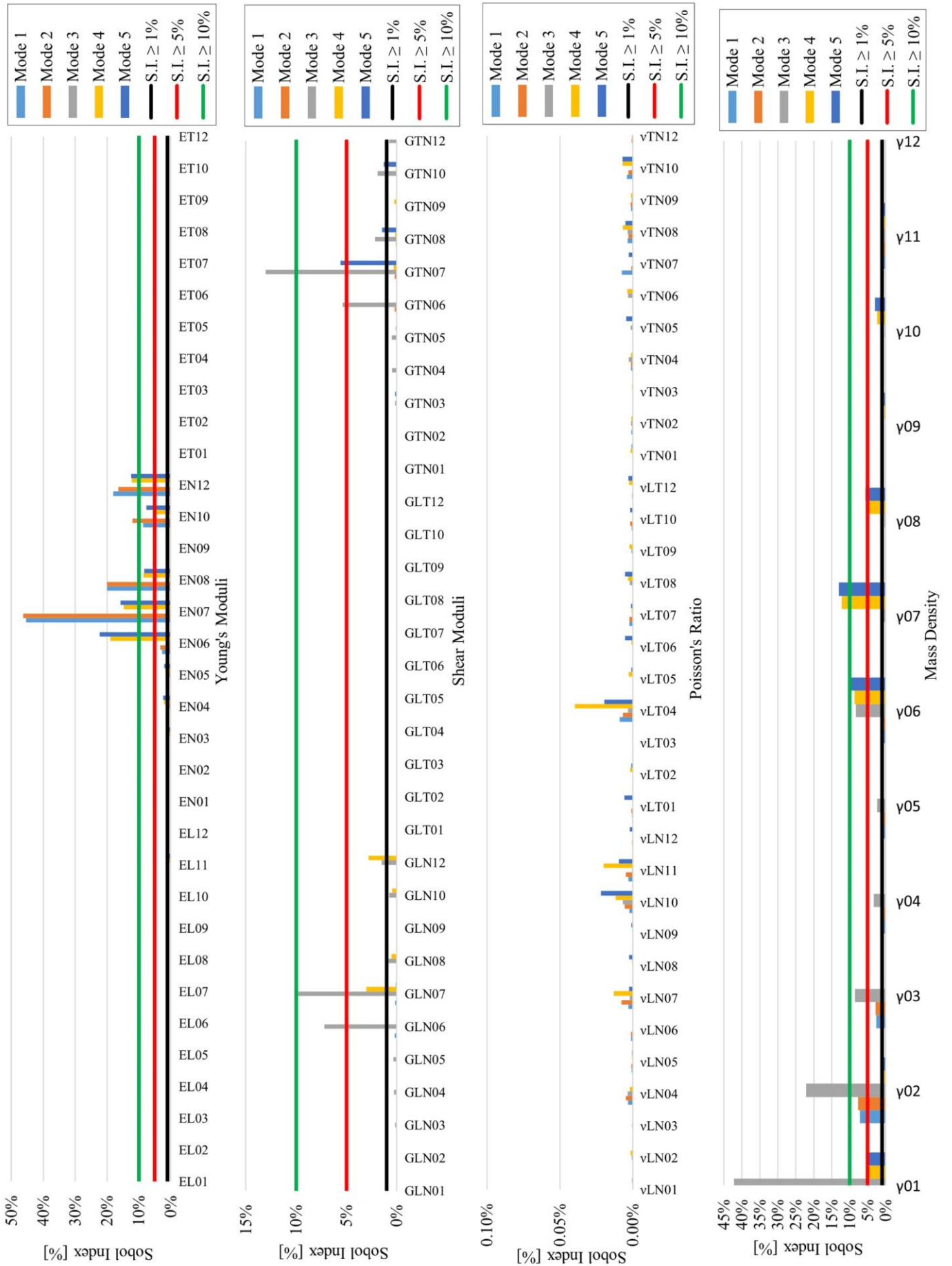


Figure A.18 - Sobol sensitivity analysis over total order indices for Kriging method. Thresholds of Sobol Indices (SI) respectively highlighted in black (SI = 1%), green (SI = 5%) and red (SI = 10%).

In light of the results obtained considering Total Order Sobol sensitivity analysis the following parameters were considered for calibration of NM19 with orthotropic material approach (Table A.10).

*Table A.10 Material parameters considered for calibration of NM19 after Sobol sensitivity analysis, using orthotropic approach.*

	<b>Orthotropic material parameters</b>	<b>Total</b>
<b>S.I. <math>\geq 1\%</math></b>	$E_{N04} - E_{N05} - E_{N06} - E_{N07} - E_{N08} - E_{N10} - E_{N12}$ $G_{LN06} - G_{LN07} - G_{LN08} - G_{LN12} - G_{TN06} - G_{TN07} - G_{TN08} - G_{TN10} - G_{TN12}$ $\gamma_{01} - \gamma_{02} - \gamma_{03} - \gamma_{04} - \gamma_{05} - \gamma_{06} - \gamma_{07} - \gamma_{08} - \gamma_{10} - \gamma_{11} - \gamma_{12}$	27
<b>S.I. <math>\geq 5\%</math></b>	$E_{N06} - E_{N07} - E_{N08} - E_{N10} - E_{N12}$ $G_{LN06} - G_{LN07} - G_{TN06} - G_{TN07}$ $\gamma_{01} - \gamma_{02} - \gamma_{06} - \gamma_{07} - \gamma_{08}$	14
<b>S.I. <math>\geq 10\%</math></b>	$E_{N06} - E_{N07} - E_{N08} - E_{N10} - E_{N12}$ $G_{LN07} - G_{TN07}$ $\gamma_{01} - \gamma_{02} - \gamma_{07}$	10

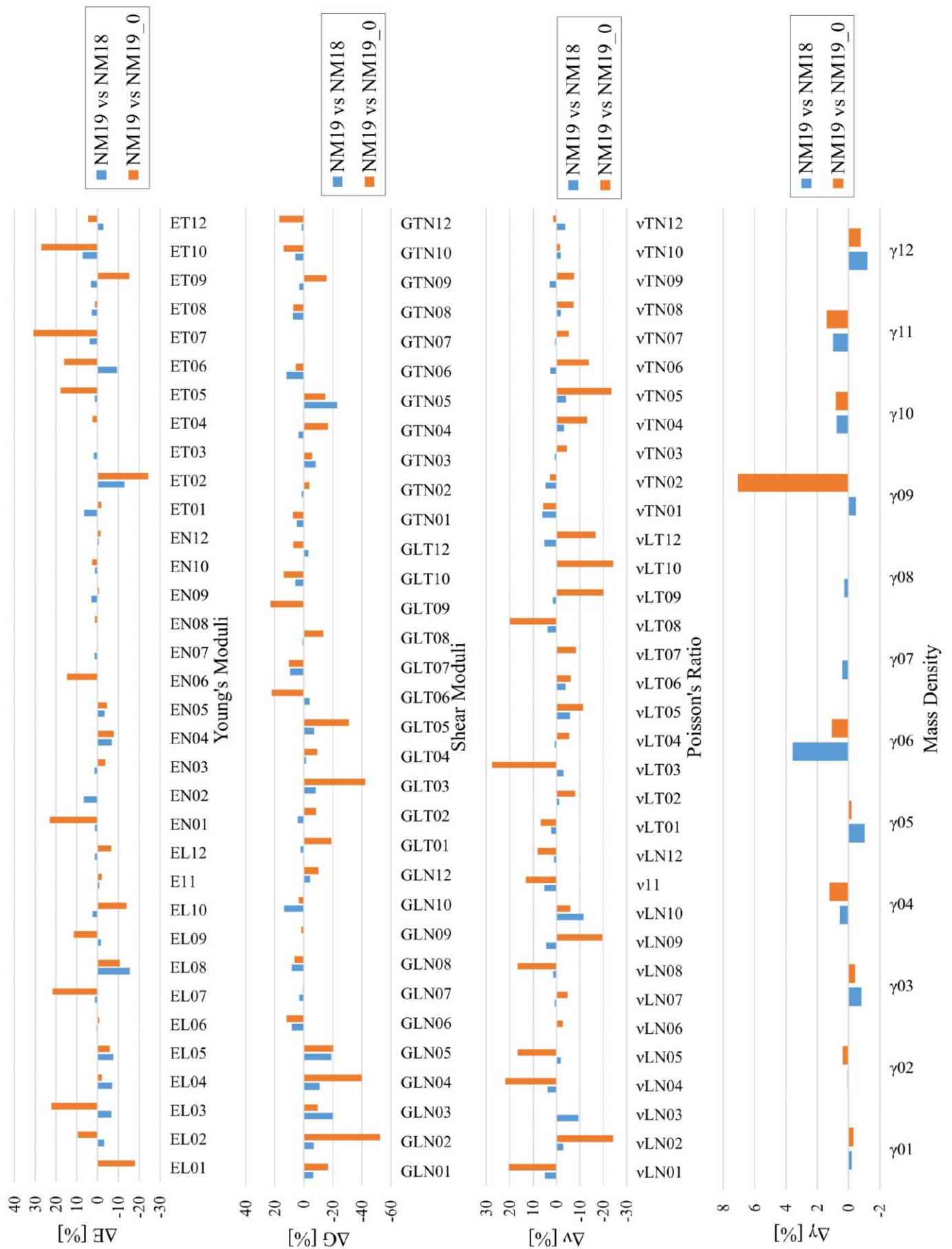


Figure A.19 - Variation of NM19 material parameters in comparison to NM18 (in blue) and NM19\_0 (in orange), considering all parameters in the calibration process.

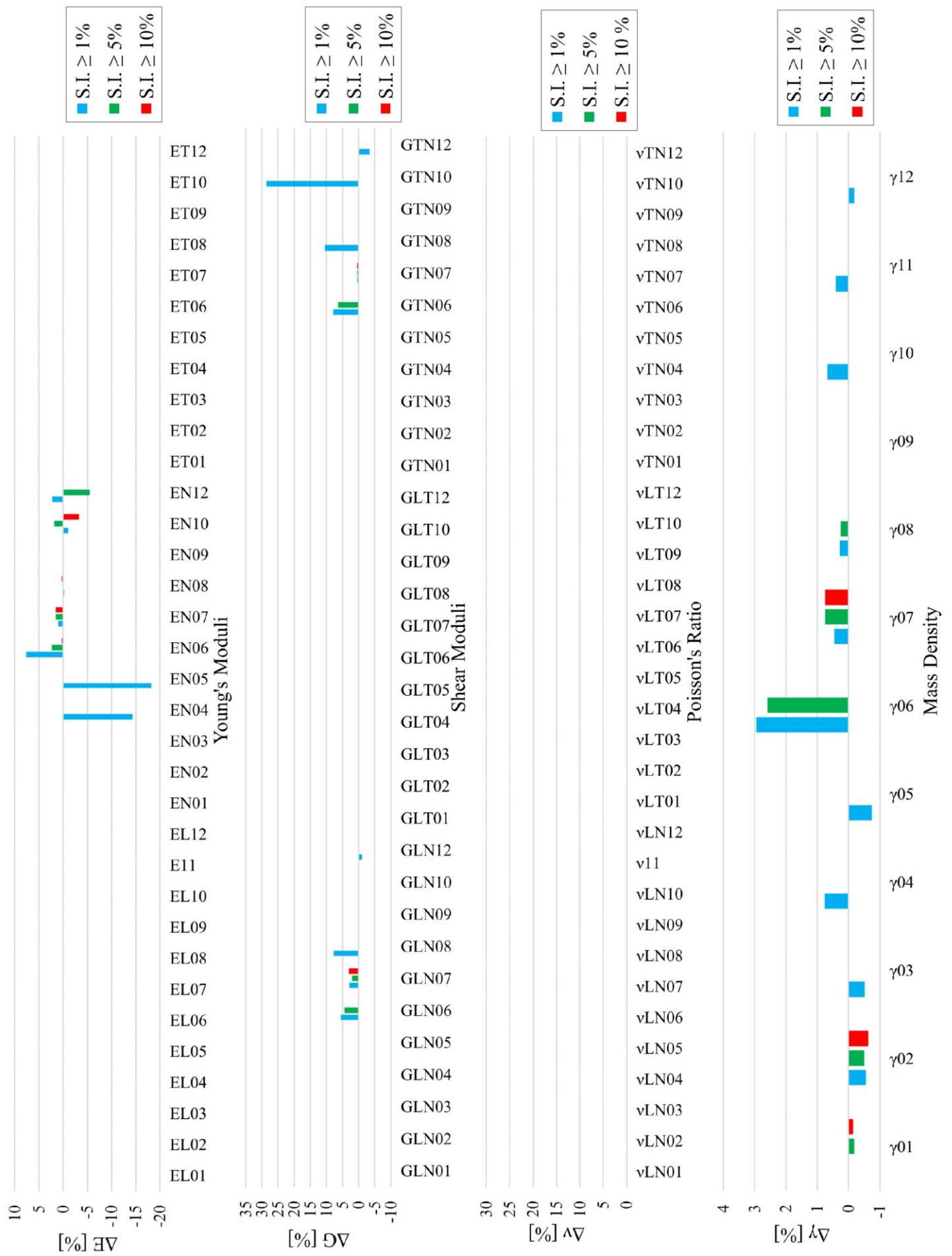


Figure A.20 - Variation of NM19 material parameters with respect to NM18 considering a reduced number of variables based on different thresholds of SI.



Comparing the final values of the material parameters of the updated model of 2019 (NM19) with those obtained from models NM18 and NM19\_0, both calibrated directly against experimental data, it is observed a better agreement between NM19 and NM18 (Figure A.19). This allows to draw the same conclusions emerged for the isotropic counterparts, namely that updating with new information a refined baseline model previously calibrated not only is faster and less demanding from a computational viewpoint as compared to the construction and full updating of another metamodel from scratch, but also less prone to statistical variations from random error sources. Still, if weighing up the total percentage variation of the parameters with respect to the relevant isotropic models, the differences become larger due to the greater number of parameters involved in the updating process of the orthotropic models.

Lastly, the comparison between NM18 and NM19, both calibrated with a reduced number of parameters chosen on the basis of the sensitivity analyses previously described, shows a very marginal level of variation among the final materials variables, confirming the goodness of the sensitivity-based calibration process (Figure A.20). Nevertheless, the very high computational cost required by the global sensitivity analysis with respect to the optimization procedure herein proposed cannot be overlooked. Moreover, analogously to the isotropic case, the frequency relative errors of the first five modes of the tower are always very low regardless of the number of updating parameters considered in the optimization (Table A.11), thus no substantial improvement is found by reducing the unknown variables beforehand.

Table A.11- Variation of calibrated frequencies of NM19 in relation to the number of parameters subdued to updating process.

Mode	All Parameters					S.I. = 1%		S.I. = 5%		S.I. = 10%	
	$f_{\text{NM18}}$ [Hz]	$f_{\text{NM19}_0}$ [Hz]	$f_{\text{NM19}}$ [Hz]	$ \Delta f_{\text{NM18}} $ [%]	$ \Delta f_{\text{NM19}_0} $ [%]	$f_{\text{NM19}}$ [Hz]	$ \Delta f_{\text{NM18}} $ [%]	$f_{\text{NM19}}$ [Hz]	$ \Delta f_{\text{NM18}} $ [%]	$f_{\text{NM19}}$ [Hz]	$ \Delta f_{\text{NM18}} $ [%]
$\varphi_1$	2.084	2.093	2.091	0.33	0.10	2.095	0.53	2.092	0.38	2.093	0.43
$\varphi_2$	2.137	2.134	2.143	0.28	0.42	2.143	0.28	2.141	0.19	2.139	0.09
$\varphi_3$	6.284	6.288	6.229	0.88	0.95	6.278	0.10	6.280	0.06	6.265	0.30
$\varphi_4$	6.516	6.532	6.510	0.09	0.34	6.488	0.43	6.495	0.32	6.508	0.12
$\varphi_5$	6.907	6.852	6.930	0.33	1.13	6.878	0.42	6.903	0.06	6.913	0.09

## A.5. Convergence criteria

This section summarizes the comparison among the convergence rates of the different optimization processes, namely the GA-based updating versus the Sobol method. The latter was carried out using the parameters reported in Table A.8 and Table A.10.

These rates are analysed for both isotropic and orthotropic material approaches, considering the convergences of the models calibrated from zero (NM18 and NM19\_0) – i.e. directly targeting the corresponding EM results (see Figure A.21, Figure A.22, Figure A. 24, Figure A.25) – and the convergence of the optimization process performed to update model NM18 with 2019 experimental information (indicated as EM19), see Figure A.23 and Figure A.26.

In order to ensure the stability of the global optimal solution, the processes have been repeated by increasing progressively the number of iterations. In the first run of the optimization procedure this number was set equal to 100, in the second run equal to 200, 500 for the third run and 2000 for the last calibration. Noticeable differences can be seen among the convergence rates of the various optimization procedures.

It must be noted that, in the plots, the number of iterations visible along the horizontal axis corresponds to the product between the total number of iterations previously listed and the generated sub-iterations. This happens because, as it was indicated in Section A.1, the number of sub-iterations that are calculated during one iteration are as many as the NB\_FILLS. Having this parameter defined as 6, the

number of iterations multiplied by the number of sub-iterations gives the total number of operations reported in the figures of the convergence rates.

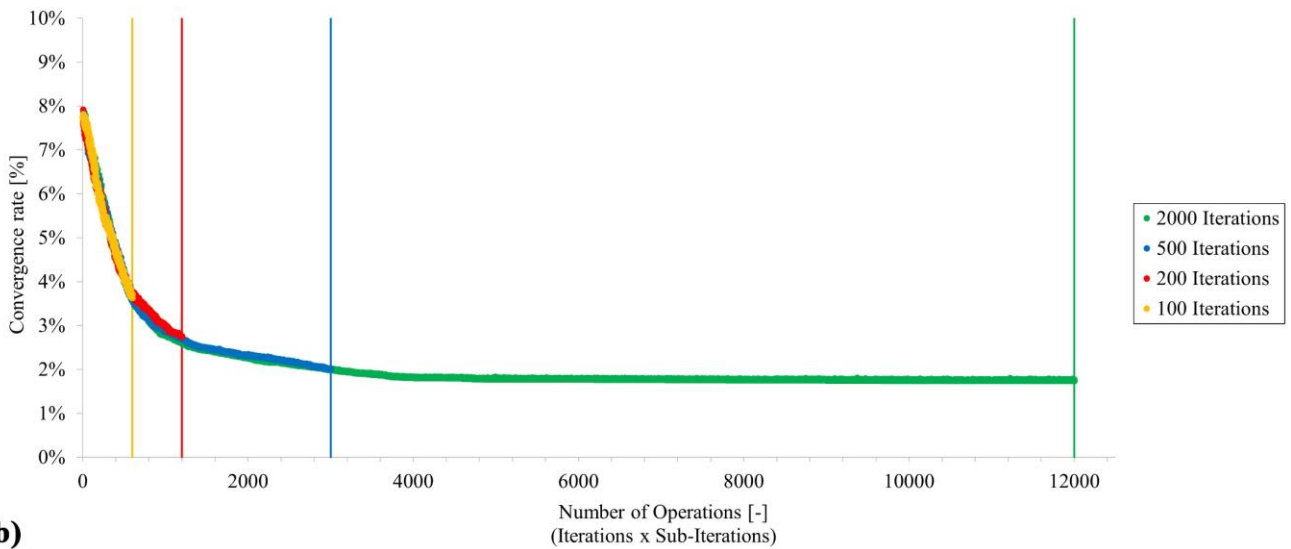
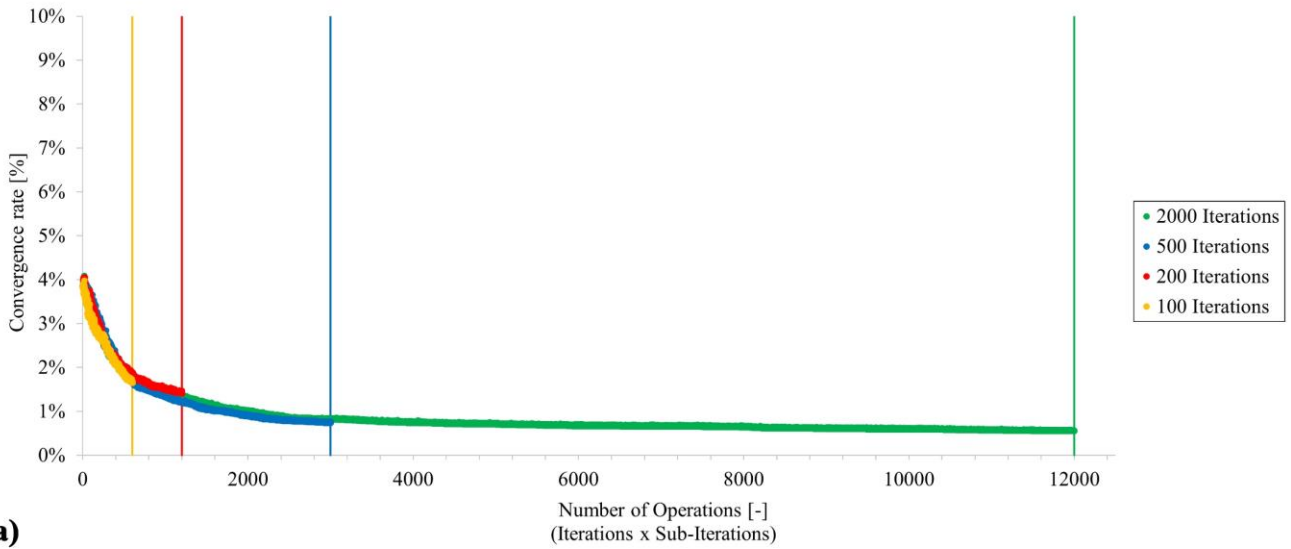


Figure A.21- Influence of number of iterations on the convergence rate of NM2018 with isotropic material approach: calibration considering (a) all material parameters and (b) reduced number of parameters (based on thresholds fixed for SI).

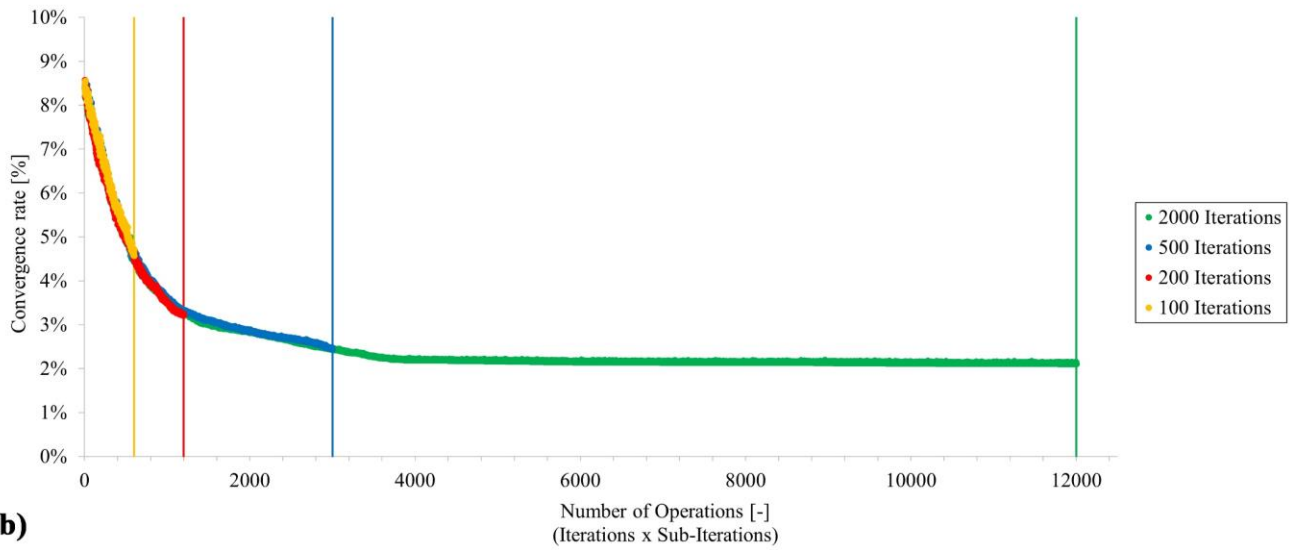
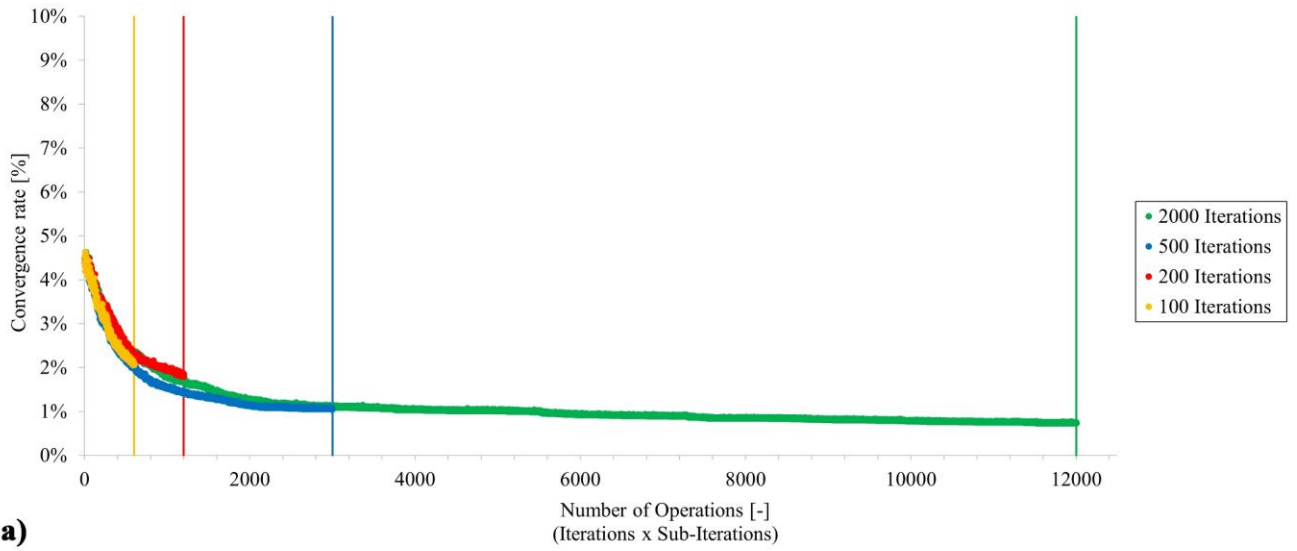


Figure A.22 - Influence of number of iterations on the convergence rate of NM2019\_0 with isotropic material approach: calibration considering (a) all material parameters and (b) reduced number of parameters (based on thresholds fixed for SI).

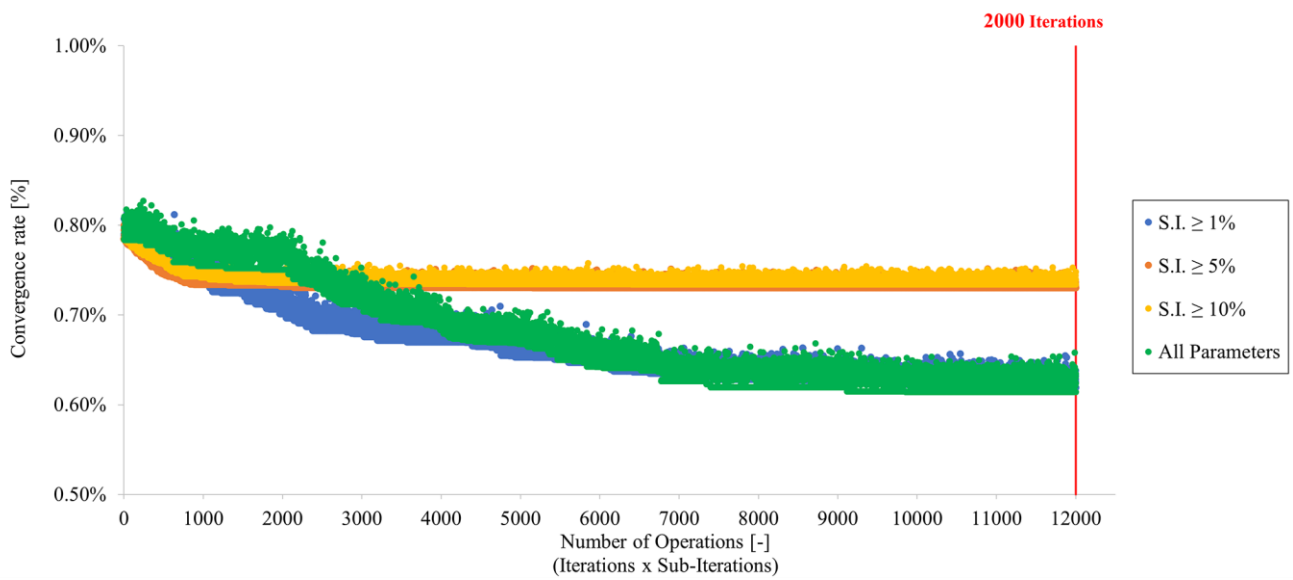
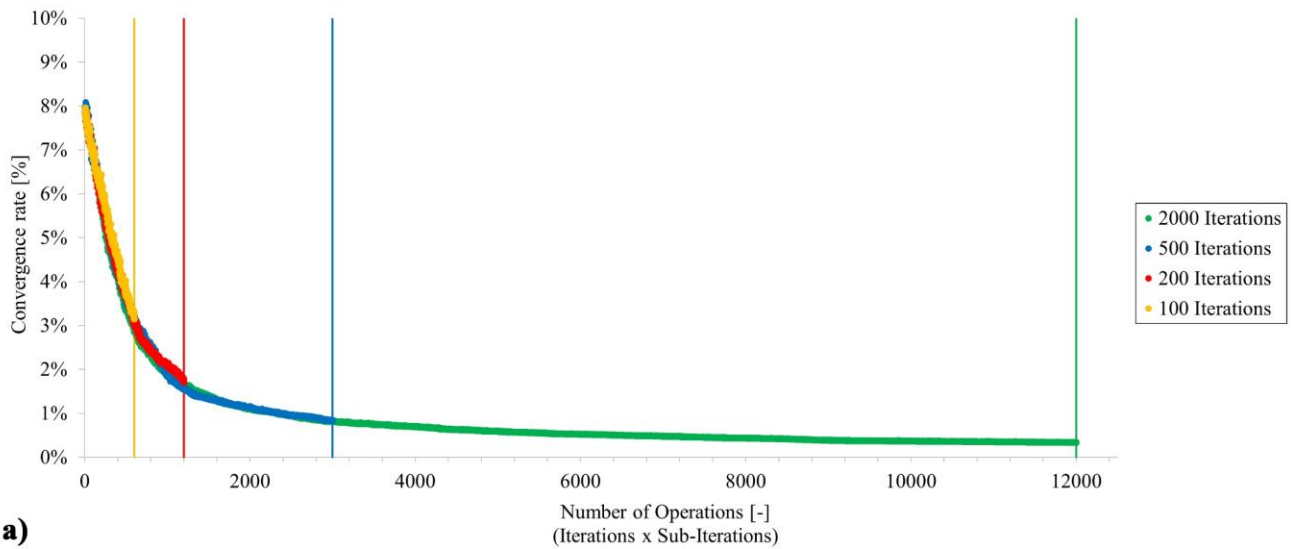
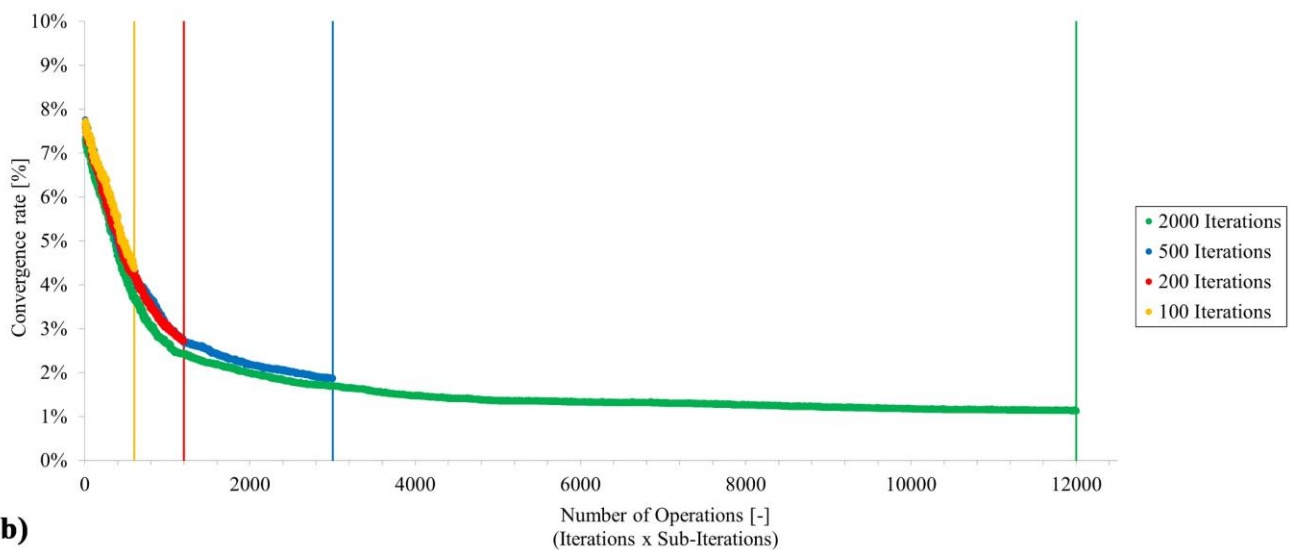


Figure A.23 - Comparison of convergence rate variations in the updating process of NM2019 isotropic model starting from NM2018 and using 2000 iterations: GA-based approach (green) versus Sobol method for different thresholds (blue, orange and yellow).



a)



b)

Figure A. 24 - Influence of number of iterations on the convergence rate of NM2018 with orthotropic material approach: calibration considering (a) all material parameters and (b) reduced number of parameters (based on thresholds fixed for SI).

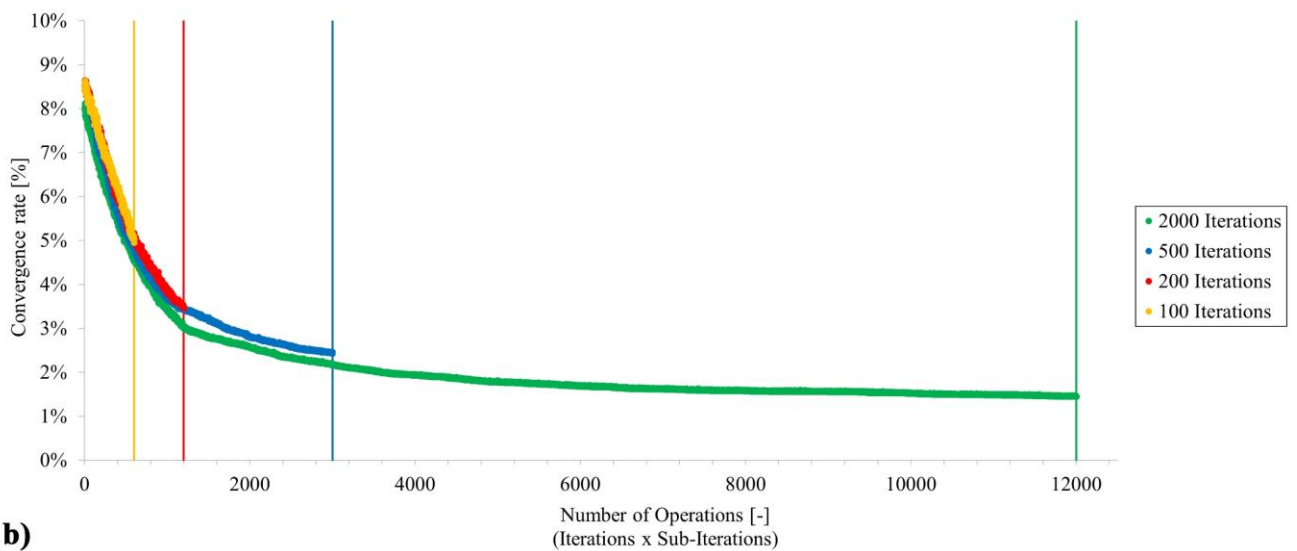
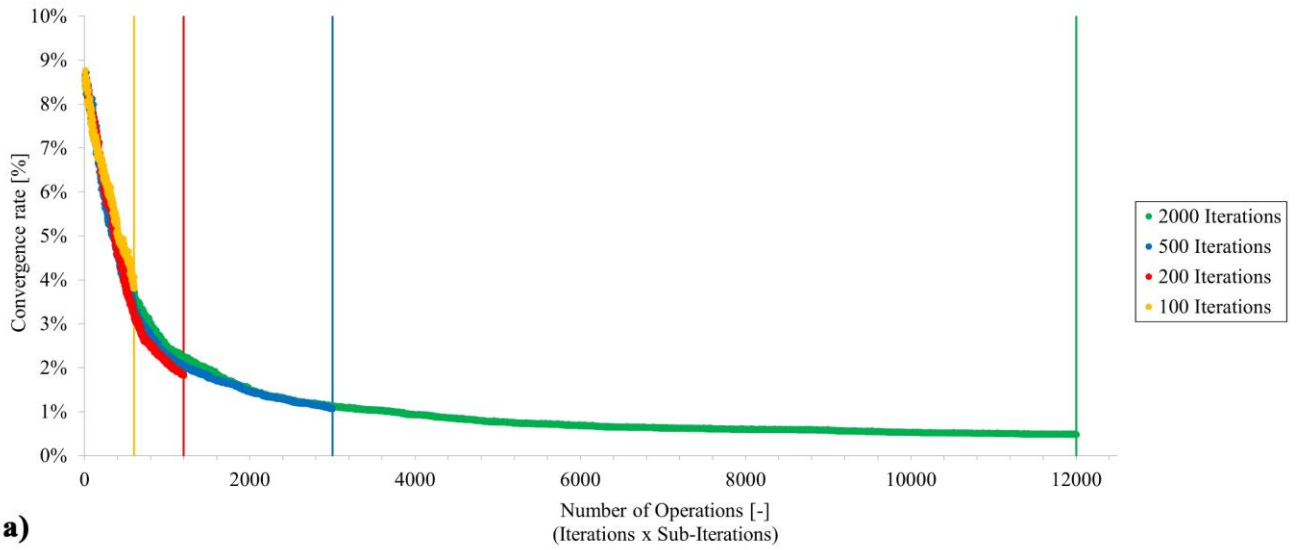


Figure A.25 - Influence of number of iterations on the convergence rate of NM2019\_0 with orthotropic material approach: calibration considering (a) all material parameters and (b) educed number of parameters (based on thresholds fixed for SI).



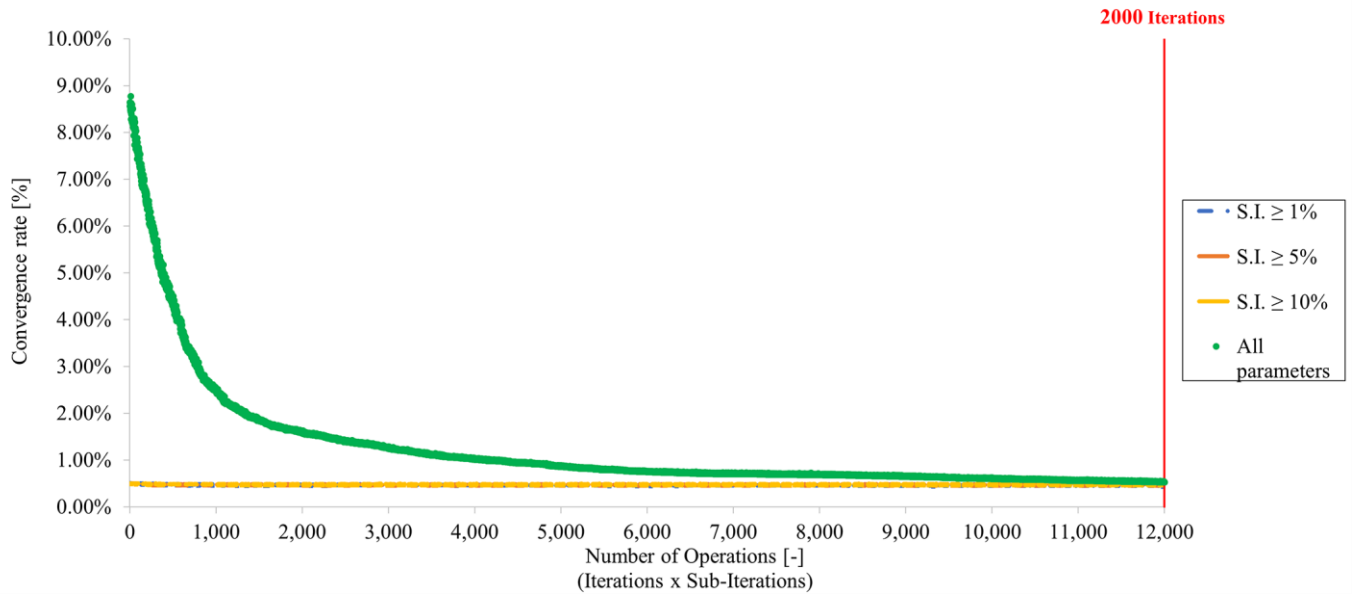


Figure A.26 - Comparison of convergence rate variations in the updating process of NM2019 orthotropic model starting from NM2018 and using 2000 iterations: GA-based approach (green) versus Sobol method for different thresholds (blue, orange and yellow).

Table A.12, Table A.13, Table A.14, Table A.15 summarize the frequency relative errors estimated for the five vibration modes of the tower as the number of iterations of the optimization process increases. As expected, the lowest errors are found with the highest number of iterations (2000), whose run is much more feasible, robust and remarkably less time-consuming using the proposed GA-based optimization approach.

Table A.12 - Variation of frequencies of calibrated NM2018 with isotropic approach in relation to different number of iterations.

Mode	100 Iterations			200 Iterations		500 Iterations		2000 Iterations	
	$f_{EM18}$ [Hz]	$f_{NM18}$ [Hz]	$ \Delta f_{EM18-NM18} $ [%]	$f_{NM18}$ [Hz]	$ \Delta f_{EM18-NM18} $ [%]	$f_{NM18}$ [Hz]	$ \Delta f_{EM18-NM18} $ [%]	$f_{NM18}$ [Hz]	$ \Delta f_{EM18-NM18} $ [%]
$\varphi_1$	2.082	1.987	4.56	2.014	3.27	2.062	0.96	2.070	0.58
$\varphi_2$	2.156	2.021	6.26	2.049	4.96	2.098	2.69	2.111	2.09
$\varphi_3$	6.293	6.326	0.52	6.379	1.37	6.281	0.19	6.280	0.21
$\varphi_4$	6.442	6.818	5.84	6.842	6.21	6.751	4.80	6.700	4.00
$\varphi_5$	6.941	7.000	0.85	7.022	1.17	6.901	0.58	6.850	1.31

Table A.13 - Variation of frequencies of calibrated NM2019\_0 with isotropic approach in relation to different number of iterations.

Mode	100 Iterations			200 Iterations		500 Iterations		2000 Iterations	
	$f_{EM19}$ [Hz]	$f_{NM19_0}$ [Hz]	$ \Delta f_{EM19-NM19_0} $ [%]	$f_{NM19_0}$ [Hz]	$ \Delta f_{EM19-NM19_0} $ [%]	$f_{NM19_0}$ [Hz]	$ \Delta f_{EM19-NM19_0} $ [%]	$f_{NM19_0}$ [Hz]	$ \Delta f_{EM19-NM19_0} $ [%]
$\varphi_1$	2.092	1.989	4.92	2.011	3.87	2.057	1.67	2.078	0.67
$\varphi_2$	2.165	2.024	6.51	2.046	5.50	2.091	3.42	2.121	2.03
$\varphi_3$	6.302	6.352	0.79	6.345	0.68	6.287	0.24	6.279	0.36
$\varphi_4$	6.449	6.797	5.40	6.838	6.03	6.755	4.74	6.693	3.78
$\varphi_5$	6.872	6.976	1.51	7.021	2.17	6.908	0.52	6.843	0.42

Table A.14 - Variation of frequencies of calibrated NM2018 with orthotropic approach in relation to different number of iterations.

Mode	100 Iterations			200 Iterations		500 Iterations		2000 Iterations	
	$f_{EM18}$ [Hz]	$f_{NM18}$ [Hz]	$ \Delta f_{EM18-NM18} $ [%]	$f_{NM18}$ [Hz]	$ \Delta f_{EM18-NM18} $ [%]	$f_{NM18}$ [Hz]	$ \Delta f_{EM18-NM18} $ [%]	$f_{NM18}$ [Hz]	$ \Delta f_{EM18-NM18} $ [%]
$\varphi_1$	2.082	2.079	0.14	2.070	0.58	2.074	0.38	2.084	0.10
$\varphi_2$	2.156	2.123	1.53	2.115	1.90	2.119	1.72	2.137	0.88
$\varphi_3$	6.293	6.277	0.25	6.283	0.16	6.276	0.27	6.284	0.14
$\varphi_4$	6.442	6.645	3.15	6.645	3.15	6.647	3.18	6.516	1.15
$\varphi_5$	6.941	6.789	2.19	6.790	2.18	6.794	2.12	6.907	0.49

Table A.15 - Variation of frequencies of calibrated NM2019\_0 with orthotropic approach in relation to different number of iterations.

Mode	100 Iterations			200 Iterations		500 Iterations		2000 Iterations	
	$f_{EM19}$ [Hz]	$f_{NM19_0}$ [Hz]	$ \Delta f_{EM19-NM19_0} $ [%]	$f_{NM19_0}$ [Hz]	$ \Delta f_{EM19-NM19_0} $ [%]	$f_{NM19_0}$ [Hz]	$ \Delta f_{EM19-NM19_0} $ [%]	$f_{NM19_0}$ [Hz]	$ \Delta f_{EM19-NM19_0} $ [%]
$\varphi_1$	2.092	2.079	0.62	2.070	1.05	2.074	0.86	2.093	0.05
$\varphi_2$	2.165	2.123	1.94	2.115	2.31	2.119	2.12	2.134	1.43
$\varphi_3$	6.302	6.277	0.40	6.283	0.30	6.276	0.41	6.288	0.22
$\varphi_4$	6.449	6.645	3.04	6.645	3.04	6.647	3.07	6.532	1.29
$\varphi_5$	6.872	6.789	1.21	6.790	1.19	6.794	1.14	6.852	0.29

### Credit authorship contribution statement

**Gianluca Standoli:** Conceptualization, Methodology, Software, Validation, Formal analysis, Investigation, Writing - original draft, Writing - review & editing.

**Georgios Panagiotis Salachoris:** Conceptualization, Methodology, Software, Validation, Formal analysis, Investigation, Writing - original draft, Writing - review & editing.

**Maria Giovanna Masciotta:** Investigation, Data processing, analysis and interpretation, Writing – final draft, Writing – review & editing, Supervision.

**Francesco Clementi:** Conceptualization, Methodology, Validation, Formal analysis, Investigation, Writing - original draft, Writing - review & editing, Supervision, Project Administration.

### Declaration of Competing Interest

The authors declare that they have no known competing financial interests or personal relationships that could have appeared to influence the work reported in this paper.

### Acknowledgements

The present study has been carried out within the framework of the National Operational Programme on Research and Innovation (Attraction and International Mobility) PON-AIM 2014-2020 Line 2, co-financed by the European Social Fund and by the National Rotation Fund.

The Authors would like to thank Novatest S.r.l. for providing the devices used to collect vibration data during the two field testing campaigns.

## References

- [1] M. Acito, M. Bocciarelli, C. Chesi, G. Milani, Collapse of the clock tower in Finale Emilia after the May 2012 Emilia Romagna earthquake sequence: Numerical insight, *Eng. Struct.* 72 (2014) 70–91. <https://doi.org/10.1016/j.engstruct.2014.04.026>.
- [2] M. Betti, A. Vignoli, Numerical assessment of the static and seismic behaviour of the basilica of Santa Maria all’Impruneta (Italy), *Constr. Build. Mater.* 25 (2011) 4308–4324. <https://doi.org/10.1016/j.conbuildmat.2010.12.028>.
- [3] G. Brandonisio, G. Lucibello, E. Mele, A. De Luca, Damage and performance evaluation of masonry churches in the 2009 L’Aquila earthquake, *Eng. Fail. Anal.* 34 (2013) 693–714. <https://doi.org/10.1016/j.engfailanal.2013.01.021>.
- [4] S. Lagomarsino, S. Podestà, Damage and Vulnerability Assessment of Churches after the 2002 Molise, Italy, Earthquake, *Earthq. Spectra.* 20 (2004) 271–283. <https://doi.org/10.1193/1.1767161>.
- [5] G. Milani, Lesson learned after the Emilia-Romagna, Italy, 20–29 May 2012 earthquakes: A limit analysis insight on three masonry churches, *Eng. Fail. Anal.* 34 (2013) 761–778. <https://doi.org/10.1016/j.engfailanal.2013.01.001>.
- [6] G. Binda, L ; Anzani, A ; Mirabella Roberti, The failure of ancient towers : Problems of their safety assessment, in: *Compos. Constr. - Conv. Innov.* (Innsbruck, 16-18 Sept. 1997), IABSE, Zurich, Innsbruck, 1997: pp. 699–704. <http://pascal-francis.inist.fr/vibad/index.php?action=getRecordDetail&idt=2445686>.
- [7] G. Bartoli, M. Betti, L. Galano, G. Zini, Numerical insights on the seismic risk of confined masonry towers, *Eng. Struct.* 180 (2019) 713–727. <https://doi.org/10.1016/j.engstruct.2018.10.001>.
- [8] A. Cabboi, C. Gentile, A. Saisi, From continuous vibration monitoring to FEM-based damage assessment: Application on a stone-masonry tower, *Constr. Build. Mater.* 156 (2017) 252–265. <https://doi.org/10.1016/j.conbuildmat.2017.08.160>.
- [9] G. Castellazzi, A.M. D’Altri, S. de Miranda, A. Chiozzi, A. Tralli, Numerical insights on the seismic behavior of a non-isolated historical masonry tower, *Bull. Earthq. Eng.* 16 (2018) 933–961. <https://doi.org/10.1007/s10518-017-0231-6>.
- [10] C. Gentile, M. Guidobaldi, A. Saisi, One-year dynamic monitoring of a historic tower: damage detection under changing environment, *Meccanica.* 51 (2016) 2873–2889. <https://doi.org/10.1007/s11012-016-0482-3>.
- [11] F. Magalhães, A. Cunha, E. Caetano, Vibration based structural health monitoring of an arch bridge: From automated OMA to damage detection, *Mech. Syst. Signal Process.* 28 (2012) 212–228. <https://doi.org/10.1016/j.ymsp.2011.06.011>.
- [12] M. Pieraccini, D. Dei, M. Betti, G. Bartoli, G. Tucci, N. Guardini, Dynamic identification of historic masonry towers through an expeditious and no-contact approach: Application to the “Torre del Mangia” in Siena (Italy), *J. Cult. Herit.* 15 (2014) 275–282. <https://doi.org/10.1016/j.culher.2013.07.006>.
- [13] N. Cavalagli, G. Comanducci, C. Gentile, M. Guidobaldi, A. Saisi, F. Ubertini, Detecting earthquake-induced damage in historic masonry towers using continuously monitored dynamic response-only data, *Procedia Eng.* 199 (2017) 3416–3421. <https://doi.org/10.1016/j.proeng.2017.09.581>.
- [14] A. Saisi, C. Gentile, A. Ruccolo, Static and dynamic monitoring of a Cultural Heritage bell-tower in Monza, Italy, *Procedia Eng.* 199 (2017) 3356–3361. <https://doi.org/10.1016/j.proeng.2017.09.563>.
- [15] M.G. Masciotta, L.F. Ramos, P.B. Lourenço, M. Vasta, Structural monitoring and damage identification on a masonry chimney by a spectral-based identification technique, in: A.. Cunha, P.. Ribeiro, E.. Caetano, M. G. (Eds.), *Proc. Int. Conf. Struct. Dyn. , EURO DYN Vol. 2014-January, 2014, European Association for Structural Dynamics, Porto, Portugal, 2014: pp. 211–218.*

- [16] P.F. Giordano, F. Ubertini, N. Cavalagli, A. Kita, M.G. Masciotta, Four years of structural health monitoring of the San Pietro bell tower in Perugia, Italy: two years before the earthquake versus two years after, *Int. J. Mason. Res. Innov.* 5 (2020) 445–467. <https://doi.org/10.1504/IJMRI.2020.111797>.
- [17] M.G. Masciotta, L.F. Ramos, Dynamic identification of historic masonry structures, in: P.B. Ghiassi, Bahman; Lourenco (Ed.), *Long-Term Perform. Durab. Mason. Struct.*, Woodhead, Publishing Series in Civil and Structural Engineering, Woodhead Publishing (2019), 2019: pp. 241–264. <https://doi.org/10.1016/B978-0-08-102110-1.00008-X>.
- [18] B.M. Douglas, W.H. Reid, Dynamic Tests and System Identification of Bridges, *J. Struct. Div.* 108 (1982) 2295–2312. <https://doi.org/10.1061/JSDEAG.0006057>.
- [19] T. Aoki, D. Sabia, D. Rivella, T. Komiyama, Structural Characterization of a Stone Arch Bridge by Experimental Tests and Numerical Model Updating, *Int. J. Archit. Herit.* 1 (2007) 227–250. <https://doi.org/10.1080/15583050701241208>.
- [20] A. S. Araujo, P. B. Lourenco, D. V. Oliveira, J. Leite, Seismic Assessment of St James Church by Means of Pushover Analysis – Before and After the New Zealand Earthquake, *Open Civ. Eng. J.* 6 (2012) 160–172. <https://doi.org/10.2174/1874149501206010160>.
- [21] R. Ceravolo, G. Pistone, L.Z. Fragonara, S. Massetto, G. Abbiati, Vibration-Based Monitoring and Diagnosis of Cultural Heritage: A Methodological Discussion in Three Examples, *Int. J. Archit. Herit.* 10 (2016) 375–395. <https://doi.org/10.1080/15583058.2013.850554>.
- [22] V. Compán, P. Pachón, M. Cámara, P.B. Lourenço, A. Sáez, Structural safety assessment of geometrically complex masonry vaults by non-linear analysis. The Chapel of the Würzburg Residence (Germany), *Eng. Struct.* 140 (2017) 1–13. <https://doi.org/10.1016/j.engstruct.2017.03.002>.
- [23] L.F. Ramos, M. Alaboz, R. Aguilar, P.B. Lourenço, Dynamic Identification and FE Updating of S. Torcato Church, Portugal, in: 2011: pp. 71–80. [https://doi.org/10.1007/978-1-4419-9831-6\\_9](https://doi.org/10.1007/978-1-4419-9831-6_9).
- [24] T. Zordan, B. Briseghella, T. Liu, Finite element model updating of a tied-arch bridge using Douglas-Reid method and Rosenbrock optimization algorithm, *J. Traffic Transp. Eng. (English Ed.)* 1 (2014) 280–292. [https://doi.org/10.1016/S2095-7564\(15\)30273-7](https://doi.org/10.1016/S2095-7564(15)30273-7).
- [25] R.A. Silva, N. Mendes, D. V. Oliveira, A. Romanazzi, O. Domínguez-Martínez, T. Miranda, Evaluating the seismic behaviour of rammed earth buildings from Portugal: From simple tools to advanced approaches, *Eng. Struct.* 157 (2018) 144–156. <https://doi.org/10.1016/j.engstruct.2017.12.021>.
- [26] F. Pianosi, F. Sarrazin, T. Wagener, A Matlab toolbox for Global Sensitivity Analysis, *Environ. Model. Softw.* 70 (2015) 80–85. <https://doi.org/10.1016/j.envsoft.2015.04.009>.
- [27] J.E. Mottershead, M. Link, M.I. Friswell, The sensitivity method in finite element model updating: A tutorial, *Mech. Syst. Signal Process.* 25 (2011) 2275–2296. <https://doi.org/10.1016/j.ymsp.2010.10.012>.
- [28] Z. Yuan, P. Liang, T. Silva, K. Yu, J.E. Mottershead, Parameter selection for model updating with global sensitivity analysis, *Mech. Syst. Signal Process.* 115 (2019) 483–496. <https://doi.org/10.1016/j.ymsp.2018.05.048>.
- [29] T. Bartz-Beielstein, J. Branke, J. Mehnen, O. Mersmann, *Evolutionary Algorithms*, Wiley Interdiscip. Rev. Data Min. Knowl. Discov. 4 (2014) 178–195. <https://doi.org/10.1002/widm.1124>.
- [30] M. Girardi, C. Padovani, D. Pellegrini, L. Robol, A finite element model updating method based on global optimization, *Mech. Syst. Signal Process.* (2020) 107372. <https://doi.org/10.1016/j.ymsp.2020.107372>.
- [31] R.I. Levin, N.A.J. Lieven, Dynamic finite element model updating using simulated annealing and genetic algorithms, *Mech. Syst. Signal Process.* 12 (1998) 91–120. <https://doi.org/10.1006/mssp.1996.0136>.
- [32] W. Torres, J.L. Almazán, C. Sandoval, R. Boroschek, Operational modal analysis and FE model updating of the Metropolitan Cathedral of Santiago, Chile, *Eng. Struct.* 143 (2017) 169–188. <https://doi.org/10.1016/j.engstruct.2017.04.008>.

- [33] M.. Betti, G.. Bartoli, R.. Corazzi, V.. Kovacevic, Strumenti Open Source per l'ingegneria strutturale. Modellazione meccanica non lineare di edifici in muratura, *Boll. Ing.* 60 (2013) 3–15.
- [34] G. Bartoli, M. Betti, A.M. Marra, S. Monchetti, A Bayesian model updating framework for robust seismic fragility analysis of non-isolated historic masonry towers, *Philos. Trans. R. Soc. A Math. Phys. Eng. Sci.* 377 (2019) 20190024. <https://doi.org/10.1098/rsta.2019.0024>.
- [35] E. García-Macías, L. Ierimonti, I. Venanzi, F. Ubertini, Comparison of Surrogate Models for Handling Uncertainties in SHM of Historic Buildings, in: *Proc. XXIV AIMETA Conf. 2019, 2020*: pp. 1645–1657. [https://doi.org/10.1007/978-3-030-41057-5\\_132](https://doi.org/10.1007/978-3-030-41057-5_132).
- [36] K. Smarsly, K. Dragos, J. Wiggenbrock, Machine learning techniques for structural health monitoring, *8th Eur. Work. Struct. Heal. Monit. EWSHM 2016.* 2 (2016) 1522–1531.
- [37] Y. Ying, J.H. Garrett, I.J. Oppenheim, L. Soibelman, J.B. Harley, J. Shi, Y. Jin, Toward Data-Driven Structural Health Monitoring: Application of Machine Learning and Signal Processing to Damage Detection, *J. Comput. Civ. Eng.* 27 (2013) 667–680. [https://doi.org/10.1061/\(ASCE\)CP.1943-5487.0000258](https://doi.org/10.1061/(ASCE)CP.1943-5487.0000258).
- [38] M. Sanayei, E.S. Bell, C.N. Javdekar, J.L. Edelmann, E. Slavsky, Damage Localization and Finite-Element Model Updating Using Multiresponse NDT Data, *J. Bridg. Eng.* 11 (2006) 688–698. [https://doi.org/10.1061/\(ASCE\)1084-0702\(2006\)11:6\(688\)](https://doi.org/10.1061/(ASCE)1084-0702(2006)11:6(688)).
- [39] G.. Barchiesi, *Ostra in Cartolina (in Italian)*, Banca di Credito Cooperativo, 1994.
- [40] *Guida storica artistica e turistica di Ostra (in Italian)*, Ostra, 2015.
- [41] F. Clementi, A. Pierdicca, A. Formisano, F. Catinari, S. Lenci, Numerical model upgrading of a historical masonry building damaged during the 2016 Italian earthquakes: the case study of the Podestà palace in Montelupone (Italy), *J. Civ. Struct. Heal. Monit.* 7 (2017) 703–717. <https://doi.org/10.1007/s13349-017-0253-4>.
- [42] C. Gentile, A. Saisi, P. Borlenghi, FE modelling for seismic assessment of an ancient tower from ambient vibration survey, in: *8th IOMAC - Int. Oper. Modal Anal. Conf., Copenhagen, 2019*: pp. 295–305. <http://hdl.handle.net/11311/1124063>.
- [43] I. Venanzi, A. Kita, N. Cavalagli, L. Ierimonti, F. Ubertini, Continuous OMA for damage detection and localization in the Sciri Tower in Perugia, Italy, in: *8th IOMAC - Int. Oper. Modal Anal. Conf. Proc., 2019*: pp. 127–136.
- [44] D. Pellegrini, M. Girardi, P.B. Lourenço, M.G. Masciotta, N. Mendes, C. Padovani, L.F. Ramos, Modal analysis of historical masonry structures: Linear perturbation and software benchmarking, *Constr. Build. Mater.* 189 (2018) 1232–1250. <https://doi.org/10.1016/j.conbuildmat.2018.09.034>.
- [45] F. Ubertini, G. Comanducci, N. Cavalagli, A. Laura Pisello, A. Luigi Materazzi, F. Cotana, Environmental effects on natural frequencies of the San Pietro bell tower in Perugia, Italy, and their removal for structural performance assessment, *Mech. Syst. Signal Process.* 82 (2017) 307–322. <https://doi.org/10.1016/j.ymsp.2016.05.025>.
- [46] E. Giordano, F. Clementi, A. Barontini, M. Giovanna, E. Chatzi, F. Luís, Damage detection and optimal sensor placement in health monitoring of “Collegiata di Santa Maria” in Visso ( Central Italy ) Damage detection and optimal sensor placement in health monitoring of “Collegiata di Santa Maria” in Visso ( Central Italy ), (2019) 44–53.
- [47] J. Rodriguez, *Identificação Modal Estocástica: Métodos de Análise e Aplicações em Estruturas de Engenharia Civil*, 2004.
- [48] G. Standoli, E. Giordano, G. Milani, F. Clementi, Model Updating of Historical Belfries Based on Oma Identification Techniques, *Int. J. Archit. Herit.* (2020) 1–25. <https://doi.org/10.1080/15583058.2020.1723735>.
- [49] F. Ubertini, C. Gentile, A.L. Materazzi, Automated modal identification in operational conditions and its application to bridges, *Eng. Struct.* 46 (2013) 264–278. <https://doi.org/10.1016/j.engstruct.2012.07.031>.
- [50] ARTeMIS Modal, (2018).
- [51] B. Peeters, G. De Roeck, Reference-Based Stochastic Subspace Identification for Output-Only



- Modal Analysis, Mech. Syst. Signal Process. 13 (1999) 855–878. <https://doi.org/10.1006/mssp.1999.1249>.
- [52] A. Bajrić, J. Høgsberg, Identification of damping and complex modes in structural vibrations, *J. Sound Vib.* 431 (2018) 367–389. <https://doi.org/10.1016/j.jsv.2018.05.048>.
- [53] A.P. Brincker R, Zhang L, Modal identification from ambient responses using frequency domain decomposition, in: Proc. 18th Int. Modal Anal. Conf. San Antonio, TX, Febr., San Antonio, Texas, 2000: pp. 625–630.
- [54] D.J. Ewins, *Modal Testing: Theory, Practice and Application*, Baldock, Hertfordshire, England, 2000.
- [55] N.J.. Jacobsen, P. Andersen, R.. Brinker, Using Enhanced Frequency Domain Decomposition as a Robust Technique to Harmonic Excitation in Operational Modal Analysis, in: ISMA2006 Int. Conf. Noise Vib. Eng. Kathol. Univ., Leuven (Belgium), 2006. <https://vbn.aau.dk/en/publications/using-enhanced-frequency-domain-decomposition-as-a-robust-techniq>.
- [56] M.R. Mitchell, R.E. Link, B. Sevim, A. Bayraktar, A.C. Altunişik, S. Adanur, M. Akköse, Modal Parameter Identification of a Prototype Arch Dam Using Enhanced Frequency Domain Decomposition and Stochastic Subspace Identification Techniques, *J. Test. Eval.* 38 (2010) 102731. <https://doi.org/10.1520/JTE102731>.
- [57] M. Pastor, M. Binda, T. Harčarik, Modal Assurance Criterion, *Procedia Eng.* 48 (2012) 543–548. <https://doi.org/10.1016/j.proeng.2012.09.551>.
- [58] L.F. Ramos, G. De Roeck, P.B. Lourenço, A. Campos-Costa, Damage identification on arched masonry structures using ambient and random impact vibrations, *Eng. Struct.* 32 (2010) 146–162. <https://doi.org/10.1016/j.engstruct.2009.09.002>.
- [59] L.F. Ramos, L. Marques, P.B. Lourenço, G. De Roeck, A. Campos-Costa, J. Roque, Monitoring historical masonry structures with operational modal analysis: Two case studies, *Mech. Syst. Signal Process.* 24 (2010) 1291–1305. <https://doi.org/10.1016/j.ymsp.2010.01.011>.
- [60] Ministero delle Infrastrutture e dei Trasporti, D.M 17 gennaio 2018 “Aggiornamento delle Norme tecniche per le Costruzioni,” Suppl. Ordin. Alla “Gazzetta Uff. n. 42 Del 20 Febbraio 2018- Ser. Gen. (2018) 1–198.
- [61] R.S. Olivito, S. Porzio, A new multi-control-point pushover methodology for the seismic assessment of historic masonry buildings, *J. Build. Eng.* 26 (2019) 100926. <https://doi.org/10.1016/j.jobe.2019.100926>.
- [62] A.B. S Bagchi, TB Roy, Multiple damage localization of gravity Dam: strain energy based approach using random data, in: CSCE Annu. Conf., 2019.
- [63] A. Garcia-Gonzalez, A. Gonzalez-Herrera, A. Garcia-Cerezo, Damage Localization based on Modal Parameters using the Finite Element Method and Neural Networks, in: n.d. <https://doi.org/10.4203/ccp.93.48>.
- [64] F. Bianconi, G.P. Salachoris, F. Clementi, S. Lenci, A Genetic Algorithm Procedure for the Automatic Updating of FEM Based on Ambient Vibration Tests, *Sensors.* 20 (2020) 3315. <https://doi.org/10.3390/s20113315>.
- [65] J.P. Escallón, C. Wendeler, E. Chatzi, P. Bartelt, Parameter identification of rockfall protection barrier components through an inverse formulation, *Eng. Struct.* 77 (2014) 1–16. <https://doi.org/10.1016/j.engstruct.2014.07.019>.
- [66] S. Kokot, Z. Zembaty, Damage reconstruction of 3D frames using genetic algorithms with Levenberg--Marquardt local search, *Soil Dyn. Earthq. Eng.* 29 (2009) 311–323. <https://doi.org/10.1016/j.soildyn.2008.03.001>.
- [67] Á. Bautista-De Castro, L.J. Sánchez-Aparicio, P. Carrasco-García, L.F. Ramos, D. González-Aguilera, A multidisciplinary approach to calibrating advanced numerical simulations of masonry arch bridges, *Mech. Syst. Signal Process.* 129 (2019) 337–365. <https://doi.org/10.1016/j.ymsp.2019.04.043>.
- [68] A. Aloisio, I. Capanna, R. Cirella, R. Alaggio, F. Di Fabio, M. Fragiaco, Identification and Model Update of the Dynamic Properties of the San Silvestro Belfry in L’Aquila and Estimation

- of Bell's Dynamic Actions, *Appl. Sci.* 10 (2020). <https://doi.org/10.3390/app10124289>.
- [69] C. Leyder, E. Chatzi, A. Frangi, Vibration-based model updating of a timber frame structure, *Procedia Eng.* 199 (2017) 2132–2139. <https://doi.org/10.1016/j.proeng.2017.09.141>.
- [70] Q. Sun, D. Dias, Global sensitivity analysis of probabilistic tunnel seismic deformations using sparse polynomial chaos expansions, *Soil Dyn. Earthq. Eng.* 141 (2021) 106470. <https://doi.org/10.1016/j.soildyn.2020.106470>.
- [71] S.R. Arwade, M. Moradi, A. Louhghalam, Variance decomposition and global sensitivity for structural systems, *Eng. Struct.* 32 (2010) 1–10. <https://doi.org/10.1016/j.engstruct.2009.08.011>.
- [72] F. Benedettini, C. Gentile, Operational modal testing and FE model tuning of a cable-stayed bridge, *Eng. Struct.* 33 (2011) 2063–2073. <https://doi.org/10.1016/j.engstruct.2011.02.046>.
- [73] A. Hassanat, K. Almohammadi, E. Alkafaween, E. Abunawas, A. Hammouri, V.B.S. Prasath, Choosing Mutation and Crossover Ratios for Genetic Algorithms—A Review with a New Dynamic Approach, *Information.* 10 (2019) 390. <https://doi.org/10.3390/info10120390>.
- [74] K. Vekaria, C. Clack, Selective crossover in genetic algorithms: An empirical study, in: 1998: pp. 438–447. <https://doi.org/10.1007/BFb0056886>.
- [75] S. Picek, M. Golub, D. Jakobovic, Evaluation of Crossover Operator Performance in Genetic Algorithms with Binary Representation, in: 2012: pp. 223–230. [https://doi.org/10.1007/978-3-642-24553-4\\_31](https://doi.org/10.1007/978-3-642-24553-4_31).
- [76] U. A.J., S. P.D., Crossover Operators in Genetic Algorithms: a review, *ICTACT J. Soft Comput.* 06 (2015) 1083–1092. <https://doi.org/10.21917/ijsc.2015.0150>.
- [77] G. Syswerda, Simulated Crossover in Genetic Algorithms, in: 1993: pp. 239–255. <https://doi.org/10.1016/B978-0-08-094832-4.50021-0>.
- [78] X.-B. Hu, E. Di Paolo, An efficient genetic algorithm with uniform crossover for air traffic control, *Comput. Oper. Res.* 36 (2009) 245–259. <https://doi.org/10.1016/j.cor.2007.09.005>.
- [79] O. Abdoun, J. Abouchabaka, C. Tajani, Analyzing the Performance of Mutation Operators to Solve the Travelling Salesman Problem, (2012). <http://arxiv.org/abs/1203.3099>.
- [80] E. Lejeune, Geometric Stability Classification: Datasets, Metamodels, and Adversarial Attacks, *Comput. Des.* 131 (2021) 102948. <https://doi.org/10.1016/j.cad.2020.102948>.
- [81] A.I.J. Forrester, A.J. Keane, Recent advances in surrogate-based optimization, *Prog. Aerosp. Sci.* 45 (2009) 50–79. <https://doi.org/10.1016/j.paerosci.2008.11.001>.
- [82] N. V. Queipo, R.T. Haftka, W. Shyy, T. Goel, R. Vaidyanathan, P. Kevin Tucker, Surrogate-based analysis and optimization, *Prog. Aerosp. Sci.* 41 (2005) 1–28. <https://doi.org/10.1016/j.paerosci.2005.02.001>.
- [83] M. Baudin, A. Dutfoy, B. Iooss, A.-L. Popelin, Open TURNS: An industrial software for uncertainty quantification in simulation, (2015). <http://arxiv.org/abs/1501.05242>.
- [84] E. García-Macías, L. Ierimonti, I. Venanzi, F. Ubertini, An Innovative Methodology for Online Surrogate-Based Model Updating of Historic Buildings Using Monitoring Data, *Int. J. Archit. Herit.* 15 (2021) 92–112. <https://doi.org/10.1080/15583058.2019.1668495>.
- [85] J. Sacks, W.J. Welch, T.J. Mitchell, H.P. Wynn, Design and Analysis of Computer Experiments, *Stat. Sci.* 4 (1989). <https://doi.org/10.1214/ss/1177012413>.
- [86] K. Cheng, Z. Lu, C. Ling, S. Zhou, Surrogate-assisted global sensitivity analysis: an overview, *Struct. Multidiscip. Optim.* 61 (2020) 1187–1213. <https://doi.org/10.1007/s00158-019-02413-5>.
- [87] A. Marrel, B. Iooss, F. Van Dorpe, E. Volkova, An efficient methodology for modeling complex computer codes with Gaussian processes, *Comput. Stat. Data Anal.* 52 (2008) 4731–4744. <https://doi.org/10.1016/j.csda.2008.03.026>.
- [88] A. Saltelli, Making best use of model evaluations to compute sensitivity indices, *Comput. Phys. Commun.* 145 (2002) 280–297. [https://doi.org/10.1016/S0010-4655\(02\)00280-1](https://doi.org/10.1016/S0010-4655(02)00280-1).
- [89] G. Matheron, Principles of geostatistics, *Econ. Geol.* 58 (1963) 1246–1266. <https://doi.org/10.2113/gsecongeo.58.8.1246>.